STAR FORMATION IN OB ASSOCIATIONS AND CLUSTERS

BY

CHANG-HUI CHEN

B.S., National Central University, 1994
M.S., National Central University, 1996

DISSERTATION

Submitted in partial fulfillment of the requirements
for the degree of Doctor of Philosophy in Astronomy
in the Graduate College of the
University of Illinois at Urbana-Champaign, 2007

Urbana, Illinois

CERTIFICATE OF COMMITTEE APPROVAL

University of Illinois at Urbana-Champaign
Graduate College

April 11, 2007

We hereby recommend that the thesis by:

CHANG-HUI CHEN

Entitled:

STAR FORMATION IN OB ASSOCIATIONS AND CLUSTERS

Be accepted in partial fulfillment of the requirements for the degree of:

Doctor of Philosophy

Signatures:

Director of Research - You-Hua Chu

Head of Department - You-Hua Chu

Committee on Final Examination*

Chairperson - You-Hua Chu

Susan A. Lamb.
Committee Member - Susan A. Lamb

RMCrutcher
Committee Member - Richard M. Crutcher

Committee Member - Leslie W. Looney

Committee Member - Charles F. Gammie

Committee Member -

* Required for doctoral degree but not for master's degree

© 2007 by Chang-Hui Chen. All rights reserved.

Abstract

Star formation can be characterized at two levels: at microscopic level by the initial mass function (IMF), and at macroscopic level by space, time, and intensity. To understand how star formation proceeds across a region, all four parameters need to be examined. In this thesis, we used the resolved massive stars and young stellar objects (YSOs) in N 44 to study star formation at both levels with extended coverage in space and time. Our study of massive stars showed that the present-day mass functions (PDMFs) of four star formation regions do not have obvious variations and are less steep than those of field regions. The PDMFs of field stars indicates that star formation varies from location to location; therefore, assumptions made for converting PDMFs to IMFs have to be critically examined. Using *Spitzer* mid-IR observations and complementary multi-wavelength data, we confirmed 59 YSOs in N 44. The great majority of YSOs are found in molecular clouds and concentrated toward three molecular peaks. The central molecular peak has the highest concentration of YSOs and molecular material. The peak is centered on the superbubble rim and the YSOs are distributed along it, suggesting that the current star formation is most likely triggered by the expansion of the superbubble. The northern molecular peak has loosely distributed YSOs and the lowest concentration of molecular material. These YSOs are not associated with large ionized gas structures, indicating that they are the first generation of massive stars formed in that cloud. Star formation in a starburst environment at macroscopic level was studied using the resolved cluster content of luminous giant H II regions (GHRs) in M101. In the three GHRs studied, cluster types are different in GHRs with distinct morphologies. NGC 5461 is dominated by a very luminous core, and has been suggested to host a super-star cluster (SSC). Our observations show that it contains three R136-class clusters superposed on a bright stellar background in a small region. This tight group of clusters may dynamically evolve into an SSC in the future, and may appear unresolved and be identified as an SSC at large distances. In contrast, NGC 5462 consists of loosely distributed H II regions and clusters without a prominent core. It has the largest number of clusters among the three GHRs, but most of them are faint and old. NGC 5462 has the steepest cluster luminosity function and the most loosely distributed interstellar gas, qualitatively consistent with the hypothesis that massive clusters are formed in high-pressure interstellar environments.

To my parents

Acknowledgments

I would like to express my sincere gratitude to my advisor, Professor You-Hua Chu, who have guided and nurtured me throughout my study not only in scientific thinking and writing, but also in many aspects in life. Not to mention her generous support on my trips to numerous domestic and international meetings to present my work and meet other distinguished scientists. I also wish to thank Professors Charles Gammie, Susan Lamb, and Lesley Looney for their help and insightful discussions, Dick Crutcher for serving on my committee, Paul Ricker for modeling the merging of massive star clusters, and Lew Snyder and Brian Fields for delightful conversations.

Many thanks are due to Robert Gruendl for obtaining and processing ISPI data and Armin Rest for MOSAIC data. Likewise, I am thankful to Karl Gordon for processing MIPS data, Sean Points, Chris Smith, and Claudio Aguilera for providing access to their observations of N 44 and 30 Dor as part of the Magellanic Cloud Emission-Line Survey, and staffs at Kitt Peak Observatory and Cerro Tololo Inter-American Observatory for their assistance during my observation runs. On the science part, I have benefited greatly from discussion with Joe Parker, Eva Grebel, and Wolfgang Brandner on photometry, Kelsey Johnson on young massive clusters, Mordecai Mac Low and Fabian Heitsch on triggered star formation, and Nuria Calvet and Barbara Whitney on models of massive young stellar objects.

It gives me great pleasures to thank members in our Magellanic Cloud group, Robert Gruendl, Rosa Williams, and Bryan Dunne, for wonderful experiences of team work as well as their help on numerous manuscript proof-reading, especially during the final stage of my thesis work. I am also grateful to fellow graduate students and post-doc in the department, Shiya Wang, Alan Calder, Rich Cybert, Ray Chen, Shih-Ping Lai, Wen-Chin Lin, Chao-Chin Yang, and Karen Yang, for their exciting discussions, delightful collaborations, and great company.

The department office staff, Sandie Osterbur, Carol Stickrod, and Jeri Cochran have been very helpful in administrative issues, which makes my life much easier.

My non-astronomy friends have bestowed kindness and encouragement upon me, especially Sheila Chen and Shiao-Yin Wu, who have been by my side for as long as I have known them.

Finally, I would like to dedicate this thesis to my parents. They have always supported and encouraged me, and also understood my infrequent visits to them during the years of my study. Without them, I would not make it to this point.

Table of Contents

List of Tables . . . ix

List of Figures . . . x

List of Abbreviations . . . xii

Chapter 1 Introduction . . . 1
- 1.1 Scientific Problems . . . 2
- 1.2 Approach . . . 3
  - 1.2.1 Star Formation in OB Associations . . . 3
  - 1.2.2 Star Formation in Clusters . . . 4

Chapter 2 Massive Stars in the H II Complex N 44. I. the Recent Star Formation . . . 6
- 2.1 Introduction . . . 6
- 2.2 Observations and Data Reductions . . . 7
- 2.3 Methodology . . . 9
  - 2.3.1 Accuracy of the Photometry: Internal and External Tests . . . 9
  - 2.3.2 From *UBV* Photometry to Masses of Main-Sequence Stars: Reddening-Free Color Magnitude Diagrams . . . 10
- 2.4 Massive Stellar Content of N 44 . . . 12
  - 2.4.1 Star Formation Regions and Field Regions . . . 12
  - 2.4.2 Present-Day Mass Function . . . 13
- 2.5 Discussion . . . 14
  - 2.5.1 PDMFs in Star Formation Regions . . . 15
  - 2.5.2 PDMFs in Background Regions . . . 15
- 2.6 Figures and Tables . . . 16

Chapter 3 Massive Stars in the H II Complex N 44. II. the Current Star Formation . . . 39
- 3.1 Introduction . . . 39
- 3.2 Observations and Data Reductions . . . 40
  - 3.2.1 *Spitzer* IRAC and MIPS Observations . . . 41
  - 3.2.2 CTIO 4 m ISPI and MOSAIC Observations . . . 42
  - 3.2.3 Archival *HST* Images . . . 43
- 3.3 Identification of Massive YSOs . . . 43
  - 3.3.1 Selection of Massive YSO Candidates . . . 44
  - 3.3.2 Multi-wavelength Confirmation and Classification of YSOs . . . 46
- 3.4 Determination of YSO Masses . . . 49
- 3.5 Spatial Distribution of Star Formation . . . 51
  - 3.5.1 YSOs in H II Regions . . . 51
  - 3.5.2 Global Distribution of YSOs . . . 53
  - 3.5.3 Triggered Star Formation . . . 54
- 3.6 Figures and Tables . . . 55

Chapter 4 Massive Star Formation in Giant H II Regions in M101 76
4.1 Introduction 76
4.2 Observations and Data Reduction 77
4.3 Methodology 79
  4.3.1 Synthetic Photometry 80
  4.3.2 Assessing Masses and Ages of Clusters 81
  4.3.3 Assessing Cluster Sizes 82
4.4 Clusters in Three Luminous GHRs in M101 83
  4.4.1 Clusters in NGC 5461 83
  4.4.2 Clusters in NGC 5462 85
  4.4.3 Clusters in NGC 5471 86
4.5 Discussion 88
  4.5.1 Nature of Faint Cluster Candidates in GHRs 88
  4.5.2 The Fraction of Massive Stars Formed in Clusters 90
  4.5.3 Interstellar Environments of the GHRs 92
  4.5.4 Cluster Luminosity Function 92
  4.5.5 Evolutionary Aspects of the Clusters 94
4.6 Summary 95
4.7 Figures and Tables 97

Chapter 5 Conclusions 117
5.1 Summary 117
  5.1.1 Massive Star Formation in H II Complex N 44 117
  5.1.2 Clusters in GHRs in M101 118
5.2 Future Work 119
  5.2.1 New Optical and IR Ground-based Observations of N 44 – Better Data Quality 119
  5.2.2 *HST* NICMOS and WFPC2 Observations of N 44 119

References 121

Curriculum Vitae 126

List of Tables

2.1 Journal of *UBV* Photometry Observations 36
2.2 Coefficients of Transformation Functions 36
2.3 Mass Range and Main Sequence Star Counts for Star Formation Regions 36
2.4 Mass Range and Main Sequence Star Counts for Field Star Regions 37
2.5 Mass Range and Field-Corrected Main Sequence Star Counts for Star Formation Regions . . 38
2.6 Linear Least-Square Fits to the Uncorrected and Corrected Star Formation Regions and Field Regions 38

3.1 Parameters used in IRAC and MIPS Photometric Measurements 71
3.2 Effective Wavelength and Zeroth-Magnitude Flux of $UBVIJHK_s$ Bands 71
3.3 Multi-wavelength Photometry of YSO Candidates Selected from CMD Criteria 72
3.4 Inferred Physical Parameters from SED Fits to YSOs 75

4.1 Properties of the Three Luminous GHRs in M101 and 30 Dor in the LMC 112
4.2 Table of Observations 112
4.3 Photometry of Candidate Clusters in NGC 5461 113
4.4 Photometry of Candidate Clusters in NGC 5462 114
4.5 Photometry of Candidate Clusters in NGC 5471 115
4.6 Physical Properties of Massive Clusters in M101 GHRs 116
4.7 Fractional Contribution of Clusters to Total Stellar Light & Ionizing Luminosity 116

List of Figures

2.1 MCELS Hα image of N 44 labeled with three fields covered in the *UBV* observations 17
2.2 Photometric errors of standard stars and comparisons between observations and the Landolt (1992) catalog 17
2.3 Comparisons of photometry between the two long exposure dithered pointings of Field 1 . . . 18
2.4 Comparisons of photometry between the two long exposure dithered pointings of Field 2 . . . 18
2.5 Comparisons of photometry between the two long exposure dithered pointings of Field 3 . . . 19
2.6 Comparisons of the program stars in the overlap regions between each pair of fields 20
2.7 Comparisons of the program stars detected in all three bands in the overlap regions between each pair of fields 21
2.8 Comparisons of the program star photometry with the MCPS 22
2.9 Comparisons of the program star photometry with the OM95 catalog 23
2.10 CMDs of all detected stars in N 44 24
2.11 Star formation and field regions in N 44 used in determination of mass functions 25
2.12 CMDs of stars in SB-int and SB-rim 26
2.13 CMDs of stars in South H II and LH48 27
2.14 CMDs of stars in field regions F-I1 and F-I2 28
2.15 CMDs of stars in field regions F-I3 and F-I1+I2+I3 29
2.16 CMDs of stars in field regions - F-O1 and F-O2 30
2.17 CMDs of stars in field regions F-O1+O2 and Background 31
2.18 Mass functions of star formation regions 32
2.19 Mass functions of inner field regions 32
2.20 Mass functions of outer field and background regions 33
2.21 Slope to the PDMF of uncorrected star formation regions 34
2.22 Slope to the PDMF of field regions 35

3.1 MCELS Hα and MOSAIC B-band images of N 44 56
3.2 IRAC and MIPS images of N 44 57
3.3 CMDs of sources detected in N 44 58
3.4 Example SEDs of known AGB and obscured SG stars within the field of N 44 58
3.5 Multi-wavelength images, CMD, and SED of example YSOs in N 44 59
3.6 SEDs of seven Class I and I/II YSOs analyzed in the paper. 64
3.7 SEDs of twelve Class II and II/III YSOs analyzed in the paper 65
3.8 SEDs of eight Class III YSOs analyzed in the paper 67
3.9 YSOs in the H II region N 44C 68
3.10 Close-up WFPC2 images of the small H II region associated with YSO 052207.3−675819.9 projected within N 44C 68
3.11 YSOs in the H II region N 44F 69
3.12 YSOs in the H II region N 44F 69
3.13 Distribution of YSOs with respect to stellar and interstellar environments of N 44 70

4.1 POSS-II red image of M101 from the Digitized Sky Survey 98

4.2 Color composite of *HST* WFPC2 images of NGC 5461 99
4.3 Color composite of *HST* WFPC2 images of NGC 5462 100
4.4 Color composite of *HST* WFPC2 images of NGC 5471 101
4.5 *HST* WFPC2 images of the main body of NGC 5461 102
4.6 *HST* WFPC2 images of the main body of NGC 5462 103
4.7 *HST* WFPC2 images of NGC 5471 104
4.8 M_{F547M} versus ($M_{\mathrm{F547M}} - M_{\mathrm{F675W'}}$) diagram of clusters in NGC 5461 105
4.9 M_{F547M} versus ($M_{\mathrm{F547M}} - M_{\mathrm{F675W'}}$) diagram of clusters in NGC 5462 106
4.10 M_{F547M} versus ($M_{\mathrm{F547M}} - M_{\mathrm{F675W'}}$) diagram of clusters in NGC 5471 106
4.11 *HST* WFPC2 PC image of the clusters in the core of NGC 5461 (i.e., H 1105) in the F547M band 107
4.12 *HST* WFPC2 PC images of the brightest clusters in NGC 5462 and NGC 5471 107
4.13 Comparison of binned continuum images of 30 Dor and NGC 604 with M101 GHRs 108
4.14 *HST* WFPC2 images of four regions with R136-class clusters coexistent with bright diffuse stellar background 109
4.15 M_{F547M} LFs of candidate clusters in NGC 5461, NGC 5462, NGC 5471, and of the combined sample of all three GHRs 110
4.16 A 3-D diagram of age, core radius, and mass of clusters in the LMC and M101 111

List of Abbreviations

2MASS	Two Micron All Sky Survey
AGB	asymptotic giant branch
CMD	color magnitude diagram
CTIO	Cerro Tololo Inter-American Observatory
FWHM	full width at half maximum
GHR	giant H II region
HST	*Hubble Space Telescope*
IMF	initial mass function
IR	infrared
IRAC	InfraRed Array Camera
LBV	luminous blue variable
LF	luminosity function
LMC	Large Magellanic Cloud
MCELS	Magellanic Cloud Emission-Line Survey
MCPS	Magellanic Cloud Photometric Survey
MIPS	Multiband Imaging Photometer for *Spitzer*
MS	main sequence
PBCD	post basic calibrated data
PDMF	present-day mass function
PN	planetary nebula
PSF	point spread function
SED	spectral energy distribution
SG	supergiant
SSC	super-star cluster
SSP	simple stellar population

WFPC2	Wide Field Planetary Camera 2
WR	Wolf-Rayet
YSO	young stellar object

Chapter 1

Introduction

Massive stars are significant sources of energy for the interstellar medium (ISM) in a galaxy. The stellar energy feedback changes the distribution and physical conditions of the ISM, which affects future star formation. Therefore, the interplay between massive stars and the ISM plays an important role in the formation and evolution of the host galaxy.

Star formation begins with the collapse of a dense core that has either occurred due to Jeans instability or been triggered dynamically. In regions where massive stars are present, the triggering mechanism is of particular interest. Three types of triggering can occur due to the interplay between massive stars and their surrounding ISM (Elmegreen, 1998). On small scales (10 pc), stars can be formed by direct compression of pre-existing cloudlets from a high pressure surrounding medium. On intermediate scales (10^2 pc), shock compression of a nearby cloud from one side can produce a dense rim, which becomes gravitationally unstable and then fragments and collapses to form stars. On large scales (10^3 pc), expanding interstellar shells can accumulate mass, cool, and subsequently collapse to form stars.

Observationally, however, it is often difficult to convincingly demonstrate whether star formation is indeed triggered. For example, the studies of H II complexes N 11 and N 44 showed an age difference in the underlying massive stellar contents; the OB stars in the central superbubble are older than those on the shell rim or in H II regions on the periphery (Parker et al., 1992; Oey & Massey, 1995). This sequential star formation was suggested to be a result of triggering. However, the natal interstellar conditions have been altered by the energy feedback from the massive stars, destroying any direct evidence of triggering. Young stellar objects (YSOs), on the other hand, have not yet dynamically altered the large-scale interstellar conditions. Therefore, one can use the physical conditions of the surrounding ISM to assess whether or not they are examples of triggered star formation. A number of observational studies have demonstrated strong cases of triggered star formation, such as the YSOs embedded inside the dust globules in the superbubble N 51D (Chu et al., 2005), or the young massive stars formed on the borders of Galactic H II regions (Deharveng et al., 2005, 2006; Zavagno et al., 2006).

The most intense formation of massive stars takes place in giant H II regions (GHRs). Their Hα luminosities, 10^{39}–10^{41} ergs s^{-1} (Kennicutt, 1984), require an ionizing power equivalent to that of 24–2400 O5V stars (Schaerer & de Koter, 1997). In the two nearest observable GHRs, 30 Dor in the Large Magellanic Cloud (LMC) and NGC 604 in M33, where the stellar contents are well resolved, two distinct types of stellar grouping have been observed. 30 Dor is dominated by one central massive cluster, R136, while NGC 604 contains multiple OB associations spreading over a large area (Hunter et al., 1995, 1996; Walborn & Blades, 1997). It is not clear whether OB associations or compact clusters are preferentially formed in other GHRs. Particularly interesting are the luminous GHRs in M101 that have Hα luminosities $\gtrsim$ 10 times higher than 30 Dor, indicating an incredibly intense burst of star formation (e.g., Luridiana & Peimbert, 2001). With such high concentrations of massive stars, these GHRs provide an excellent laboratory to study the modes of massive star formation, and in particular to probe whether they are birthplaces of globular clusters (Kennicutt & Chu, 1988).

1.1 Scientific Problems

A fundamental characteristic of star formation is the initial mass function (IMF), which describes the frequency distribution of stellar masses at formation. Spectrophotometric observations of massive stars have been used to derive IMFs of OB associations (e.g., Massey & Thompson, 1991; Hillenbrand et al., 1993; Massey & Johnson, 1993; Massey et al., 1995; Parker et al., 2001) and for field stars away from any OB associations (Massey et al., 1995). The derived IMFs appear to suggest that the population of field stars formed with a smaller fraction of the most massive stars than populations in OB associations, indicating that the IMF of a stellar population depends on its star formation environment.

However, IMFs are derived from the observed *present-day* mass functions (PDMFs) and a priori assumptions of star formation history. For OB associations, coeval star formation is often assumed, but the co-existence of OB and Wolf-Rayet stars and embedded massive YSOs in OB associations indicates that star formation may be a prolonged process (Chu et al., 2005). Furthermore, Elmegreen & Scalo (2006) have shown that the PDMF of field stars in the LMC can be reproduced by an OB association-like IMF and a declining star formation rate (SFR) as satisfactorily as by a "field star" IMF and a constant SFR. The differing IMFs of OB associations and field stars are by no means a settled issue. To tackle this problem, it is necessary to examine star formation with extended coverage in both space and time, i.e., from OB associations to field at 200 pc distance and from $10^6 - 10^7$ yr ago to present.

Recent *Spitzer* mid-infrared (IR) observations enabled the detection of individual YSOs in the Magellanic Clouds (MCs), revealing the on-going star formation. It is now possible to use the resolved stellar population to map out star formation as a function of space and time in the MCs. As the ISM of the MCs has been surveyed in great detail, it is further possible to determine the relationship between star formation and the physical conditions and properties of the ISM. Consequently, studies of starbursts in the MCs allow us to answer fundamental questions about star formation, such as:

- Does the IMF vary with star formation environment?
- Is current star formation triggered by the energy feedback from earlier generations of stars?

In distant GHRs where individual massive stars cannot be resolved, the ensemble properties of massive stars in clusters can be studied. Their ages, masses, structural properties, and spatial distribution are determined to examine the mode of massive star formation in starburst environments. Studies of GHRs can help us answer questions about large-scale star formation:

- What causes the different types of stellar grouping?
- What are the proportions of the different types of stellar grouping?
- How does star formation vary as a function of time and location in GHRs?
- What is the relationship between the star formation activity and the interstellar conditions in GHRs?

These questions can be answered through studying the massive stellar contents of star formation regions with different levels of activity from small to large scales. In the following section we describe the approach taken in this thesis as well as the selection of the star formation regions for specific studies.

1.2 Approach

In this thesis, the properties of massive star formation in OB associations and clusters are investigated using multi-wavelength data sets. The goal of the thesis is to understand massive star formation at different levels of activity on both small and large scales and over an extended period of time in order to better grasp how the interplay between massive star formation and the ISM modifies interstellar conditions and regulates star formation activity.

1.2.1 Star Formation in OB Associations

The LMC provides an excellent laboratory to study OB associations and their surrounding fields since stars are at a common, known distance and can be individually resolved down to $\sim 1\ M_{\odot}$ at optical wavelengths.

A suitable region to study the multiple facets of star formation needs to have multiple generations of star formation in the sky plane (as opposed to along the line-of-sight) within a manageable area. LHα 120-N 44 (N 44; Henize, 1956) in the LMC is an ideal choice.

N 44 is one of the three largest H II complexes in the LMC. It contains three OB associations, LH47, 48, and 49 (Lucke & Hodge, 1970) that are in different evolutionary stages and have different interstellar structures: LH47 in the central superbubble, LH48 in one contiguous H II region at the northeast rim of the superbubble, and LH49 in a group of H II regions to the southeast exterior of the superbubble. Along the western rim of the superbubble exist a number of dense H II regions where star formation may have been triggered by the expansion of the superbubble (Oey & Massey, 1995).

In Chapter 2, we study the populations of massive stars in N 44 using new *UBV* images taken with the 0.9 m telescope of the Cerro Tololo Inter-American Observatory (CTIO). We use these populations to determine the properties of massive star formation in OB associations and their surrounding fields, and examine their relationships with the ISM and stellar energy feedback.

In Chapter 3, we use *Spitzer Space Telescope* mid-IR observations of N 44 to search for YSOs. We utilitize multi-wavelength observations to determine the nature of the YSO candidates. The interstellar environment of N 44 has been covered in several surveys and is used to infer the interstellar conditions for the YSOs. The massive YSOs are used to examine the relationship between the interstellar conditions and the stars that are formed, and also to investigate whether the current star formation is truly triggered dynamically. The detailed analysis of the resolved massive stars and YSOs in N 44 provides a comprehensive view on a small-scale starburst phenomenon.

1.2.2 Star Formation in Clusters

M101 hosts a large number of GHRs, which provide an excellent laboratory to study cluster formation. Chapter 4 reports our study of three very luminous but morphologically different GHRs in M101, NGC 5461, NGC 5462 and NGC 5471. *Hubble Space Telescope* (*HST*) images obtained in continuum bands are used to identify cluster candidates and for photometric measurements, and images in the Hα emission-line band are used to show ionized interstellar gas. The measured colors and magnitudes are compared with the evolutionary tracks generated by the Starburst99 and Bruzual & Charlot population synthesis models to determine the ages and masses of the cluster candidates. The fraction of stars formed in massive clusters has also been estimated from the clusters' contribution to the total stellar continuum emission and from a comparison between the ionizing power of the clusters and the ionizing requirement of the associated H II regions.

Our conclusions from the three aforementioned chapters of this study are given in Chapter 5. In addition, we discuss future explorations with optical and near-IR observations newly obtained using the CTIO 4m telescope as well as those proposed using the *HST*.

Chapter 2

Massive Stars in the H II Complex N 44. I. the Recent Star Formation

2.1 Introduction

A fundamental characteristic of star formation is the initial mass function (IMF). The IMF is commonly denoted as $\xi(\log m)$ in units of number of stars per logarithmic mass ($\log m$) interval per unit area. The slope of the IMF is then $\Gamma = d\ (\log \xi)/d\ (\log m)$. For a power-law mass spectrum $f(m) \propto m^{\gamma}$, the slope of the IMF becomes $\Gamma = \gamma + 1$; for example, Salpeter's (1955) IMF has $\Gamma = -1.35$.

IMFs of OB associations have been derived from spectrophotometric observations of massive stars, and the slope has been reported to be $\Gamma = -1.2 \pm 0.3$, -1.3 ± 0.3, and -1.3 ± 0.1 for the Galaxy, the LMC, and the SMC, respectively (Massey & Thompson, 1991; Hillenbrand et al., 1993; Massey & Thompson, 1991; Massey et al., 1995; Parker et al., 2001). These slopes are all similar to that of Salpeter's IMF. Observations of massive stars in the field show much steeper IMFs with $\Gamma = -3.4 \pm 1.3$, -4.1 ± 0.2, and -3.7 ± 0.5 for the Galaxy, the LMC, and the SMC, respectively (Massey et al., 1995). These results appear to suggest that IMFs depend on star formation environments; however, as described below, there exist other possible explanations.

Observations of an ensemble of stars can be used to determine the *present-day* mass function (PDMF), which depends on both the IMF and the star formation history. The derivation of an IMF from a PDMF requires a priori assumption of star formation history. For OB associations, a coeval star formation has often been assumed, but the co-existence of OB and Wolf-Rayet (WR) stars and embedded massive young stellar objects (YSOs) in OB associations indicates that star formation may be a prolonged process (Chu et al., 2005). Furthermore, Elmegreen & Scalo (2006) have shown that the PDMF of field stars in the LMC can be reproduced by a Salpeter IMF and a declining star formation rate (SFR) as satisfactorily as a steeper IMF and a constant SFR.

We have chosen the H II complex N 44 for detailed observations of its star formation in order to critically examine and inter-compare the IMFs of the OB associations and the surrounding field regions. N 44 is one of the three largest HII complexes in the LMC. It contains three OB associations, LH47, 48, and 49 (Lucke

& Hodge, 1970) that are in different evolutionary stages and interstellar structures: LH47 in the central superbubble, LH48 in one contiguous HII region at the northeast rim of the superbubble, and LH49 in a group of HII regions to the southeast exterior of the superbubble (Figure 2.1). Along the western rim of the superbubble exist a number of dense HII regions where star formation may have been triggered by the expansion of the superbubble (Oey & Massey, 1995).

We have obtained UBV images of N 44 with a large area coverage, 506 arcmin^{-2}, which also includes field regions away from the OB associations. This chapter reports the UBV observations of N 44 and how they are used to determine the PDMF of OB associations and field regions. The results allow us to examine the validity of the common assumption used in deriving IMFs.

2.2 Observations and Data Reductions

The broadband UBV images of N 44 were obtained with the 0.9 m telescope of the Cerro Tololo Inter-American Observatory (CTIO) on 2001 December 19. The images were taken with a 2048 × 2048 Tek CCD that has a pixel scale of $0\farcs4$ pixel^{-1} and covers a field-of-view of $13\farcm5 \times 13\farcm5$. To fully map N 44, three fields were obtained with a $\sim 2'$ overlap between adjacent fields. The positions of these fields are plotted over an Hα image of N 44 from the Magellanic Cloud Emission Line Survey (MCELS, Smith & The MCELS Team, 1999) in Figure 2.1. To minimize the effects of bad columns in the CCD, two pointings were used for each field, dithered by $30''$ in both the north-south and east-west directions. This dithering strategy also provides complementary internal checks of the photometry in the overlapping regions. To maximize the dynamic range, short-, medium-, and long-exposures were made in each filter of every field. The program fields, pointing positions, and exposure times in each of the filters are listed in Table 2.1.

Standard stars from Landolt (1992) were observed for photometric calibration, and those with $(B-V) \leq 0.0$ were emphatically included to ensure reliable photometric transformation for the program OB stars. About fifty standards from fields SA 95, SA 98, and Rubin 149 (Landolt, 1992) were observed at a range of airmasses to determine the extinction coefficients.

The data were processed using IRAF packages to subtract bias and dark current counts, correct pixel-to-pixel sensitivity variations (flat-fielding), remove cosmic rays, and fix bad pixels. The processed data were further reduced with IRAF routines to obtain photometric measurements. Aperture photometry was performed on the standard stars, using the `apphot` routine with a 12–15 pixel source aperture radius. Due to crowding, photometry on the program star fields was performed using the point-spread-function (PSF)-fitting routine `daophot` (Stetson, 1987). Stars were first identified in the program fields using the automated source finding routine `daofind`. Then all the detected stars were fitted by a second-order PSF[1] determined for each CCD frame, following the reduction procedures outlined in Massey & Davis (1992) and Davis (1994). The PSF-fitting routine produced instrumental magnitudes based on a small aperture, typically 4–6 pixels in radius, to optimize the signal-to-noise ratio (S/N) of the fit. An aperture correction was applied to the instrumental magnitudes of the program stars to compensate the larger aperture used to measure the standard star fluxes.

The aperture-corrected instrumental magnitudes were transformed to the final apparent magnitudes using the following transformation equations:

$$u = U + u_1 + u_2 X + u_3(U - B), \tag{2.1}$$

$$b = B + b_1 + b_2 X + b_3(B - V), \tag{2.2}$$

$$v = V + v_1 + v_2 X + v_3(B - V), \tag{2.3}$$

where U, B, and V are the apparent magnitudes in the Johnson photometric system, u, b, and v are the instrumental magnitudes, X is the airmass, and (u_1, b_1, v_1), (u_2, b_2, v_2), and (u_3, b_3, v_3) are respectively the zero point, extinction, and color coefficients to be determined. The transformation equations were fitted to the instrumental and published apparent magnitudes of the standard stars (Landolt, 1992), allowing all the coefficients to vary. The values of these coefficients and the rms errors to the transformation fit are listed in Table 2.2. The rms error is $\sim$ 0.01–0.02 mag in the V and B bands and $\lesssim$ 0.05 mag in the U band. Comparisons of the derived colors and magnitudes of the standard stars used in the transformation equations to the values determined by Landolt (1992) are shown in Figure 2.2.

After the data were calibrated to the Johnson system, the astrometric solution for each pointing was determined using $\geq$ 20 reference stars in the USNO B1.0 catalog, resulting in an rms accuracy of $\sim 0\farcs3$–$0\farcs5$. The resulting photometric lists from the short-, medium-, and long-exposures in each band for each field were then combined by clipping measurements of saturated star images or with S/N $<$ 5, and averaging multiple measurements of the same star with weights proportional to the inverse square of their errors. The photometric lists from all observations were merged into a final UBV catalog, in which only stars with both B and V detections were included and the astrometry was referenced to the V frame. The total number of stars in the final catalog is 26,862.

---

[1] The choice of second-order PSF was made because the stellar radial profiles varied across the CCD. Zeroth and first-order PSFs were also tried. Their fits left residuals in the cores and/or over-subtracted wings of the program stars, indicative of a bad PSF.

2.3 Methodology

2.3.1 Accuracy of the Photometry: Internal and External Tests

Internal Consistency Tests

The internal consistency of the photometry can be examined using the overlapping regions in the observations. We have carried out tests to examine two sources of uncertainties. The first one is in the measurement itself, which results from the uncertainty in the PSF models and aperture corrections used in each image. The second is in the photometric calibration, associated with the uncertainty in the transformation coefficients for the conversion from the instrument system to the standard photometry system.

The uncertainties in the measurements can be determined by comparing the photometric results from the two-pointing dithered observations of each field, as they were obtained close in time and covered similar areas. Figures 2.3–2.5 show the comparisons of the derived magnitudes and colors of the program stars in each pair of dithered, long-exposure images for each field. No zero-point offsets are found for any of the field in any band, indicating good consistency in measurements. The scatters of differences about the zero-point do increase at faint magnitudes and regions of bright nebular emission, i.e., most of Field 1 and part of Field 3. This is expected as the PSF-fitting routine may have difficulty correctly picking out faint sources in crowded regions or in regions with high background levels. Note that the B magnitude comparison plots for Field 3 in Fig 2.5 are self-comparisons, as one long B band exposure was corrupted by telescope tracking problems. The B magnitudes were derived twice from the good exposure, against both V dithered-pointings. Thus any measurement differences between the V pointings will propagate to the derived B magnitudes. The comparisons demonstrate that the measurements in this study are consistent to an error margin of the order of a few hundredths of a magnitude for $V \lesssim 19$.

The uncertainties in the calibrations can be examined using the overlapping regions between different fields. These images were taken at different airmasses; so if the transformation equations were not solved correctly, there will be offsets in the photometry between fields. Figures 2.6 and 2.7 show the comparisons of the derived magnitudes and colors of the program stars in overlapping regions between each pair of fields. Fig. 2.6 shows comparisons of stars detected in the B and V bands, while Fig. 2.7 shows comparisons of only those stars detected in all three bands. There are no obvious offsets observed in the comparisons between any two fields, suggesting that the transformation coefficients are self-consistent. The scatter increased towards fainter magnitudes where measurements have larger errors. The scatter is greater in the $(U - B)$ color comparisons because of the larger uncertainties in deriving the U band transformation coefficients. In conclusion, the internal tests suggest that the combined photometric uncertainties in PSF modeling and calibration are < 0.1 mag for stars with $V \lesssim 19$.

External Consistency Tests

The external consistency tests were performed using two published photometric catalogs of N 44: the *UBVI* catalog from the Magellanic Cloud Photometric Survey (MCPS, Zaritsky et al., 2004) and the *UBV* catalog of the OB associations LH47 and LH48 from the Oey & Massey (1995, hereafter OM95) study.

Comparisons of derived magnitudes and colors of stars common to our study and the MCPS catalog are shown in Figure 2.8. There are no obvious offsets between the two sets of photometric data. The scatter in the comparison plots increases at fainter magnitudes in all three bands, and is significantly larger in the $(U - B)$ than the $(B - V)$ color comparisons. We also note that the comparisons for Field 1, where prominent nebular emission is present, exhibit greater scatter than those for Field 2, where nebular emission is minimal. These trends in the scatter can be explained by the drift-scanning technique used in MCPS, which breaks down in regions with high stellar densities or bright nebular emission, in addition to their calibration problem in the U band (Zaritsky et al., 2004).

Comparisons of magnitudes and colors of stars common to our study and the OM95 catalog are shown in Figure 2.9. The comparisons in V show systematic offsets between this study and the OM95 catalog. The offset is ~ -0.04 mag in LH47, but $\sim +0.09$ mag in LH48. Similar offsets are also seen in the color comparisons; the $(B - V)$ comparisons show offsets of $\sim +0.10$ mag for LH47 and ~ -0.10 mag for LH48, which correspond to offsets of $\sim +0.06$ mag and ~ -0.01 mag in the B band. This inconsistency is unlikely to be caused by the position-dependent variations in the PSF model, which are ≤ 0.03 mag. In our study LH47 and LH48 were observed in the same field, while OM95 mapped them with three small fields ($2\farcm5 \times 4\farcm0$ each). Since our photometric measurements are consistent with those of MCPS, it is likely that the photometric inconsistencies between our results and OM95's results are largely caused by errors in their transformation coefficients. This conclusion can be verified by future photometric measurements using CCD images of N 44 taken with the CTIO 4m MOSAIC Imager.

2.3.2 From *UBV* Photometry to Masses of Main-Sequence Stars: Reddening-Free Color Magnitude Diagrams

The mass of a star can be estimated by comparing its magnitudes and colors to model predictions, if these values have been corrected for both the distance and the extinction. For the program stars, the distance correction is straightforward since the 50 kpc distance to the LMC is well established (Feast, 1999). The reddening towards individual stars is not known, but the reddening effect can be circumvented by using reddening-free colors and magnitudes, i.e., the Johnson Q parameter (Johnson & Morgan, 1953) and the Wesenheit function W (Madore, 1982). The Johnson Q parameter is defined as

$$Q = (U-B)_0 - \frac{E(U-B)}{E(B-V)}(B-V)_0, \tag{2.4}$$

where $(U-B)_0$ and $(B-V)_0$ are intrinsic colors of a star and $E(U-B)$ and $E(B-V)$ are color excesses. The Wesenheit function W is defined as

$$W = V - DM - A_V - R_V(B-V)_0, \tag{2.5}$$

where DM is the distance modulus, A_V is the extinction in the V band, and R_V is the ratio of total-to-selective extinction. Since $\frac{E(U-B)}{E(B-V)}$ and R_V are nearly independent of a star's intrinsic color, Q and W can then be rewritten with the observed color by plugging $(U-B)_0 \equiv (U-B) - E(U-B)$, $(B-V)_0 \equiv (B-V) - E(B-V)$, and $R_V \equiv \frac{A_V}{E(B-V)}$ into Equations 3.4 and 3.5:

$$\begin{aligned} Q &= [(U-B) - E(U-B)] - \frac{E(U-B)}{E(B-V)}[(B-V) - E(B-V)] \\ &= (U-B) - \frac{E(U-B)}{E(B-V)}(B-V), \end{aligned} \tag{2.6}$$

$$\begin{aligned} W &= V - DM - A_V - \frac{A_V}{E(B-V)}[(B-V) - E(B-V)] \\ &= V - DM - R_V(B-V). \end{aligned} \tag{2.7}$$

Since both intrinsic colors and observed colors result in the same values of Q and W, these two parameters are independent of the amount of extinction and thus "reddening-free".

To demonstrate the effectiveness of the reddening-free parameters, three types of color-magnitude diagrams (CMDs) for all the stars detected in the program fields are shown in Figure 2.10: $(V - DM)$ vs. $(B-V)$, $(V - DM)$ vs. $(U-B)$, and W vs. Q. A DM of 18.5 was assumed, which corresponds to the canonical LMC distance of 50 kpc; values of $\frac{E(U-B)}{E(B-V)} = 0.72$ and $R_V = 3.1$ (Mathis, 1990) were adopted for determining Q and W. Also shown in the CMDs are stellar evolutionary tracks (Lejeune & Schaerer, 2001). In the $(V - DM)$ vs. $(B-V)$ and $(V - DM)$ vs. $(U-B)$ CMDs, the extinction effect is apparent, as shown in the offset between the main-sequence (MS) branch and that expected from stellar evolutionary models. Mass estimates using these diagrams require an extinction correction, which can be tricky as these corrections are not constant across the region and need to be determined for each star individually. On the other hand, in the reddening-free W vs. Q CMDs, the mass of a star can be directly read from its location with respect to the evolutionary tracks, except in regions where the tracks are overlapping or closely spaced, i.e., those in the post-MS phase or with masses $\gtrsim 25M_\odot$ (Massey, 1985; Massey et al., 1995), making it impossible to distinguish, for example, between a $60M_\odot$ MS star and a $30M_\odot$ supergiant. Therefore, in our analysis of stellar content of N 44, we will concentrate on only the MS stars whose masses can be reasonably well estimated from photometric data, i.e., stars with masses $\lesssim 25M_\odot$, or later than $\sim$ O9 V.

2.4 Massive Stellar Content of N 44

The CMDs of all the stars detected in the program fields (Fig. 2.10) show a mixed population of stars. The most prominent features in the $(V - DM)$ vs. $(B - V)$ CMD are the red clump and red giant branch stars at the lower right part and the massive MS and blue supergiants on the left part of the CMD. While the red stars originate from the old disk population of the LMC, the blue stars represent a young population in the LMC, the majority of which may be associated with the N 44 H II complex. Some Galactic foreground stars are also present in the CMD, but the number is low. As the surface density of Galactic stars brighter than $V = 21$ is 1.3 stars arcmin^{-2} along all lines-of-sight to the LMC (Ratnatunga & Bahcall, 1985), for our observed area of 506 arcmin^{-2} the total expected number of foreground Galactic stars is 810, $\sim$ 3% of the stars in our catalog. Furthermore, the Galactic foreground stars are mostly G-type stars occupying a vertical strip near $(B - V) \sim 0.7$, so they do not confuse our analysis of blue LMC stars described below.

2.4.1 Star Formation Regions and Field Regions

To analyze the stellar populations in N 44, we have used the Hα image and CO contours in Figure 2.11 to guide our selection of regions. The Hα emission from ionized gas traces massive stars formed in the past few Myr, and the dispersal of ionized gas by stellar energy feedback can be used to infer the evolutionary stage of the underlying stellar population. The concentrations of molecular material, on the other hand, may or may not have a causal relationship with the stellar energy feedback.

In N 44, the central superbubble contains $\gtrsim$ 10 Myr old stars whose stellar winds and supernova explosions have energized the supershell (Oey & Massey, 1995). Three groups of H II regions are found with different levels of molecular concentrations: the bright H II regions on the western rim of the superbubble, the group of H II regions associated with LH49 to the southeast of the superbubble, and the H II region around LH48 at the northeast rim of the superbubble. Based considerations of these interstellar environments, we have selected these four star formation regions: (1) "SB-int" - the superbubble interior that contains the older stars in LH47; (2) "SB-rim" - H II regions on the western superbubble rim that contains the younger stars in LH47; (3) "South H II" - the brightest H II regions to the southeast of the superbubble that contains part of LH49; and (4) "LH48" - the H II region around LH48. These four selected regions are likely to represent star formation at different evolutionary stages.

Three types of field regions have been selected with the following characteristics: (1) "F-I1, F-I2, and F-I3" - inner field regions that contain faint diffuse Hα emission and are just outside of the prominent star formation regions; (2) "F-O1, F-O2" - outer field regions that contain little or no diffuse Hα emission and are, within the coverage of our observations, farthermost away from CO contours; (3) "Background" - background region that includes all the areas external to the outermost CO contour until the boundaries of the coverage of our observations. These three types of field regions can be used to examine variations in the field population.

The CMDs in $(V - DM)$ vs. $(B - V)$, $(V - DM)$ vs. $(U - B)$, and reddening-free W vs. Q of all the selected star formation and field regions are shown in Figures 2.12– 2.17. Comparisons among CMDs of star formation regions and field regions show that the number of massive stars drops quickly from the star formation regions, the inner field regions, and down to the lowest in the outer field regions. The old population, e.g., red clump and red giant branch stars, are most prominent in the field regions. To quantify the difference among all the selected regions, their PDMFs are determined and described in the following section.

2.4.2 Present-Day Mass Function

With the reddening-free colors and magnitudes and stellar evolutionary tracks, we can determine the PDMF for each selected region by counting stars in the MS phase within each mass bin. The numbers of MS stars per mass bin for the star formation regions and field regions are presented in Tables 2.3 and 2.4, respectively. Since the UBV photometry is not adequate to distinguish between stars with masses $> 25M_{\odot}$, they are counted as one bin, though it may include both MS stars and supergiants. Figures 2.18–2.19 illustrate the PDMFs of bin-size corrected numbers of MS stars per mass bin for these regions. The PDMFs of the four star formation regions show relatively fewer stars in the last four lower mass bins than those of the field regions. This is mainly caused by the incompleteness in photometric measurements due to crowding in the star formation regions and the incompleteness in detecting lower mass stars due to the larger extinction. The PDMFs of the outer field regions show a declining slope from low to high mass bins and a cutoff at masses $\sim 12M_{\odot}$. It is most likely that stars with higher masses have died and hence the population would be older than the lifetime of a $\sim 12M_{\odot}$ star. The PDMFs of the inner field regions show two components:

a declining slope over mass bins lower than the $10 - 12M_{\odot}$ bin, and a tail in the higher mass bins. The two components seen in the PDMFs of the inner field regions suggest a mixed population: the slope over low mass bins is similar to those seen in the outer field regions, while the tail in high mass bins is from the young stars associated with the diffuse Hα emission. The PDMF of the Background field region is similar to those of the inner field regions.

The slopes of the PDMFs are calculated for the four star formation regions and the Background field region. Individual inner and outer field regions have too small numbers in their PDMFs so the slopes are only calculated for the combined inner field region, F-I1+I2+I3, and the combined outer field region, F-O1+O2. The calculation of the PDMF slope excludes mass bins with $M > 25M_{\odot}$ and $M < 7M_{\odot}$ to minimize errors propagated from estimates in stellar masses and incompleteness in star counts. The exception to the latter condition is the combined outer field region, as the calculation was extended to the $5 - 7M_{\odot}$ mass bin since this bin does not seem to be affected by incompleteness and including it can help to derive a fit with statistical significance. The slopes of the PDMFs derived from linear least-square fits are -1.9 ± 0.7, -2.1 ± 0.3, -1.4 ± 0.5, -1.9 ± 0.7 for the four star formation regions SB-int, SB-rim, South H II, and LH48, and -2.7 ± 0.6, -3.1 ± 1.0, and -2.7 ± 0.4 for the field regions F-I1+I2+I3, F-O1+O2, and Background. The fitted slopes to the PDMFs are shown in Figures 2.21–2.22.

The PDMFs of the star formation regions are then corrected for the field contamination. The amount of correction was estimated from the PDMFs of F-O1+O2 and F-I1+I2+I3, respectively, as they give the lower and upper limits of the field contamination in the mass range of $7 - 25M_{\odot}$. The field-corrected PDMFs are listed in Table 2.5. Compared to the uncorrected PDMFs in Tables 2.3, the field correction made with either of the field regions is minimal in the mass range $7 - 25M_{\odot}$. The slopes are also determined for these field-corrected PDMFs, and they are -1.8 ± 0.7, -2.1 ± 0.3, -1.4 ± 0.6, -1.9 ± 0.7 for SB-int, SB-rim, South H II, and LH48, respectively. These values are essentially the same as those derived for the uncorrected regions. The best-fit PDMF slopes, the numbers of stars, and the surface densities of stars used in the fits for uncorrected and corrected star formation regions, and field regions are given in Table 2.6.

2.5 Discussion

The PDMFs we have determined clearly depend on both the IMFs and star formation history. By comparing the PDMFs among the star formation regions and with the field regions, we hope to gain insight into the star formation history and hence the IMFs.

2.5.1 PDMFs in Star Formation Regions

The PDMFs for the four star formation regions in N 44 (Fig. 2.21) do not show obvious variations. The fitted slopes of the PDMFs have large error bars because of the small mass range (7–25 $M_{\odot}$, or B4–O9 stars) and small number of stars used in the fits. It is interesting to note that the SB-rim region has the largest number of stars and its PDMF is steeper than the Salpeter IMF; however, we caution that this steeper slope may be caused by the inclusion of stars of different ages along the rim, where an evolved WR star and YSOs have both been reported.

It is also interesting to note that the observed PDMFs below 7 $M_{\odot}$ are visibly lower than the best-fit PDMFs determined from the 7–25 $M_{\odot}$ mass range. Several factors may contribute to this deficiency of observed lower mass stars: (1) incompleteness due to higher extinction, especially for SB-rim and South H II where high concentrations of molecular material is present and extinction is expected to be high; (2) incompleteness due to crowding, e.g., the tight cluster in N 44B located within SB-rim; and (3) lower-mass stars have not reached MS to be detected. To differentiate among these factors, future deep observations at longer wavelengths, such as *IJHK* bands, are needed to detect lower mass stars and improve the completeness. The slopes of PDMFs can be better determined if the stellar mass range in the fits can be extended to lower masses.

2.5.2 PDMFs in Background Regions

In N 44, we find that the PDMFs of field regions have steeper slopes, $\Gamma = -3.1$ to -2.7, than the slope in the field-corrected star formation regions, $\Gamma = -2.1$ to -1.3. At the first glance, our results seem to follow a similar trend reported by Massey et al. (1995) study, who derived a steeper IMF for stars with masses $> 25 M_{\odot}$ in the field regions, defined as $2'$ (30 pc) away from the boundaries of OB associations, given that most massive stars have a lifetime of ~ 3 Myr and assuming a velocity of 10 km s^{-1}.

We have looked into the physical significance of "field population" using the field regions for N 44. The field region, as defined by Massey et al. (1995), in N 44 would be everything at $\geq 2'$ away from the main OB associations LH47/48/49, and thus includes all three types of field regions selected in our study. Our inner and outer field regions are at different distances from OB associations, and thus their PDMFs can be examined for spatial variations. The PDMFs of the combined-inner and combined-outer field regions in Fig. 2.22 show similar slopes, but different cutoffs at the high-mass end. The inner field regions even contain massive stars with masses greater than 25 $M_{\odot}$, while the outer field regions have no stars greater than $\sim$12 $M_{\odot}$. Table 2.4 shows that the numbers of stars with $3 \leq M < 7$ $M_{\odot}$ are 479 and 264 in the inner and outer field regions, respectively. If the inner/outer number ratio of these low mass stars is representative of the relative star formation activity, we expect the outer field regions to contain 28 stars with $7 \leq M < 12$ $M_{\odot}$ and 7 stars with $M > 12$ $M_{\odot}$; however, only 14 and 0 stars are observed in these two mass ranges. The deficiency in massive stars in the outer field regions, compared with the inner field regions, is real, instead of being caused by fluctuations in small number statistics.

We have examined the location of the most massive stars in the inner field regions, and find them all associated with small discrete H II regions or inside diffuse H II shell structures. Apparently, the inner field regions host recent star formation, and the outer field regions have no recent star formation. It is possible that star formation has propagated across space and the star formation history varies from location to location. Therefore, star formation history can be a complex function of space and time, and the derivation of IMFs from PDMFs could be really tricky. Observations of the current star formation (i.e., YSOs) allow us to see the trend of propagation of star formation in space, and may help us critically evaluate the assumptions made for converting PDMFs to IMFs.

2.6 Figures and Tables

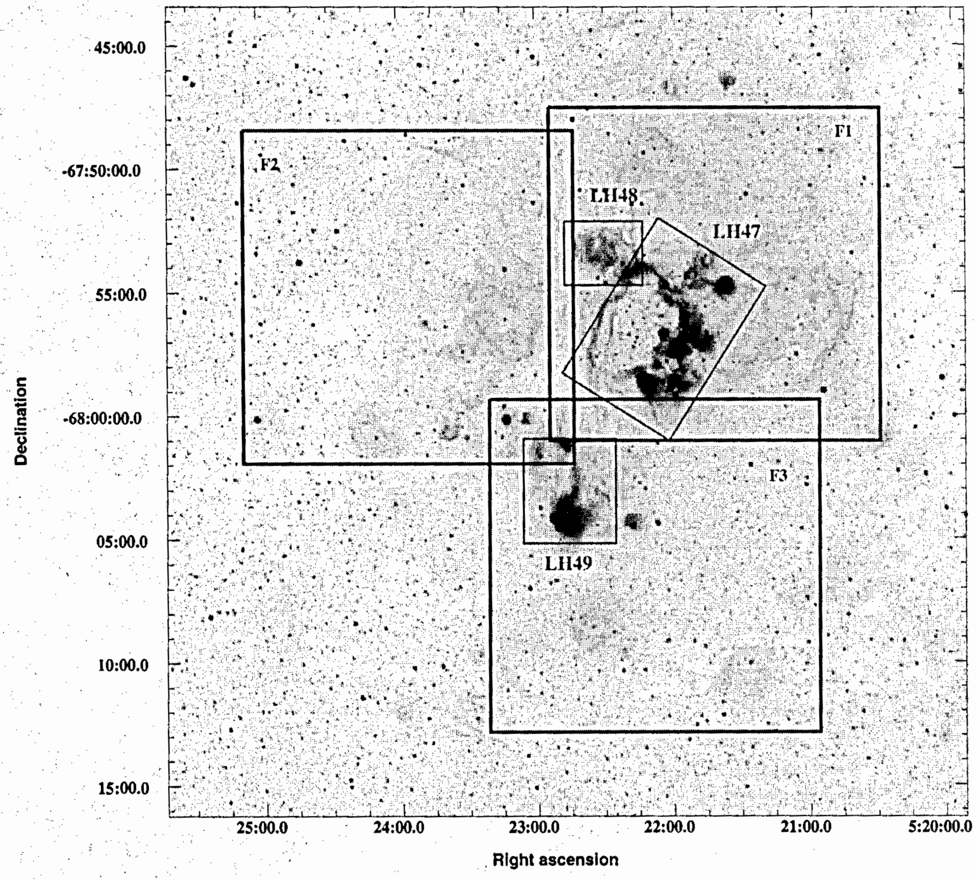

Figure 2.1 MCELS Hα image of N 44 labeled with three fields covered in the UBV observations. Each box has a 13.'5×13.'5 field-of-view. The OB associations LH47, 48, and 49 (Lucke & Hodge, 1970) are also marked.

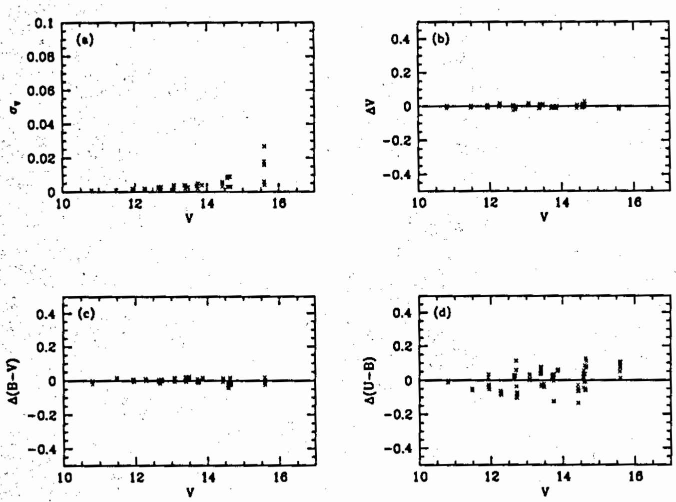

Figure 2.2 Photometric errors of standard stars and comparisons between observations and the Landolt (1992) catalog. (a) Photometric errors in V as a function of V magnitude for standard star observations. (b)–(d) Differences in the V magnitude, $(B-V)$, and $(U-B)$ as a function of V magnitude for the standard star observations and those of Landolt (1992). The differences refer to (this work – Landolt (1992))

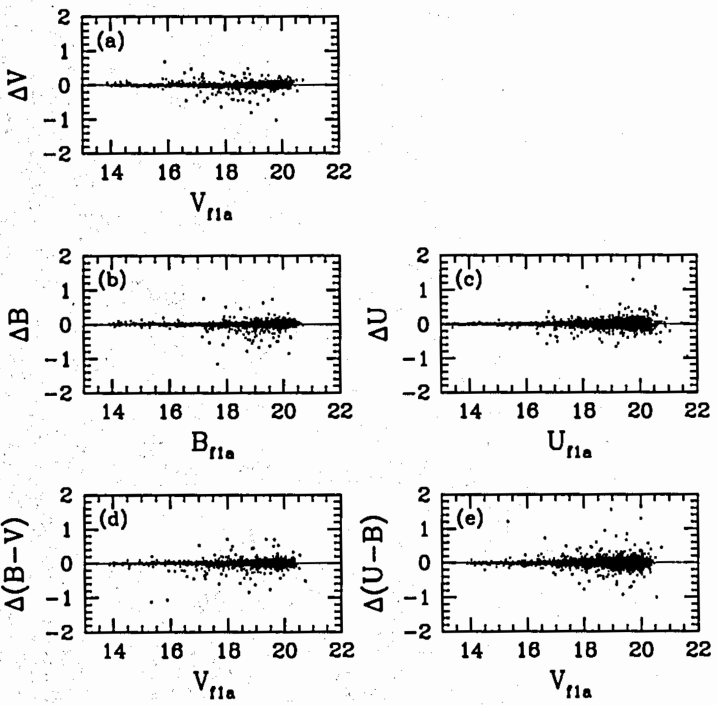

Figure 2.3 Comparisons of photometry between the two long exposure dithered pointings of Field 1, designated as f1a and f1b. (a) Differences in the V magnitude as a function of V magnitude. (b) Differences in the B magnitude as a function of B magnitude. (c) Differences in the U magnitude as a function of U magnitude. (d) Differences in the $(B - V)$ magnitude as a function of V magnitude. (e) Differences in the $(U - B)$ magnitude as a function of V magnitude. The differences refer to (f1b − f1a).

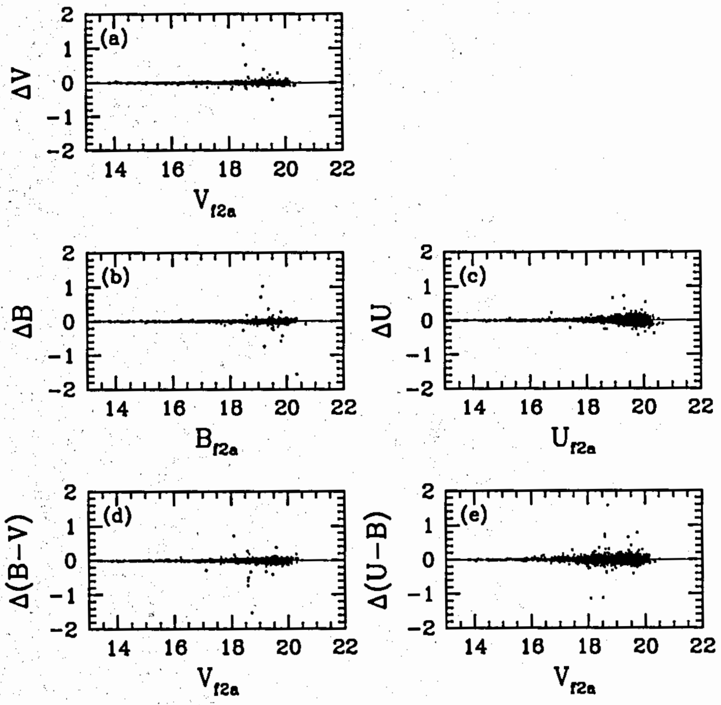

Figure 2.4 Comparisons of photometry between the two long exposure dithered pointings of Field 2, designated as f2a and f2b. Individual comparisons mirror those in Fig. 2.3.

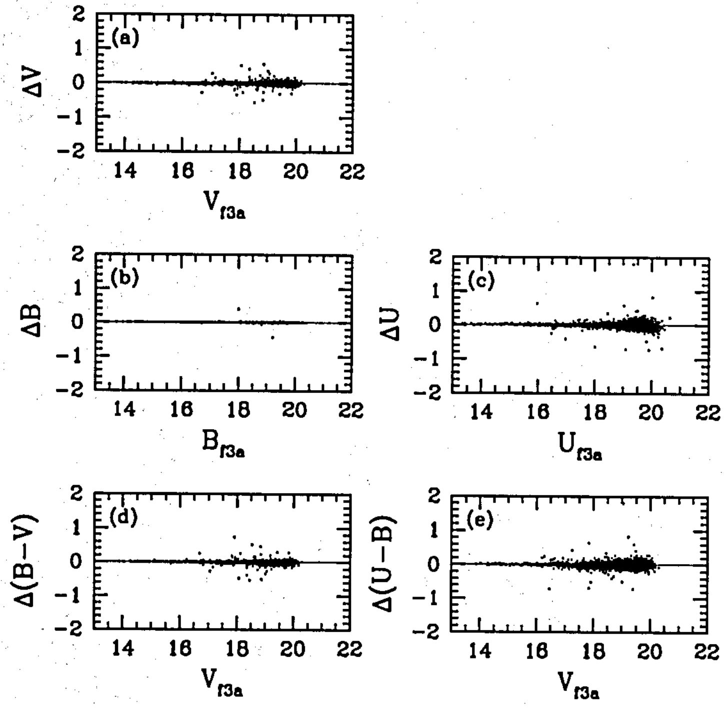

Figure 2.5 Comparisons of photometry between the two long exposure dithered pointings of Field 3, designated as f3a and f3b. Individual comparisons mirror those in Fig. 2.3. Note that the *B* magnitude comparison plots are self-comparisons and thus show almost no scatters (see text for details).

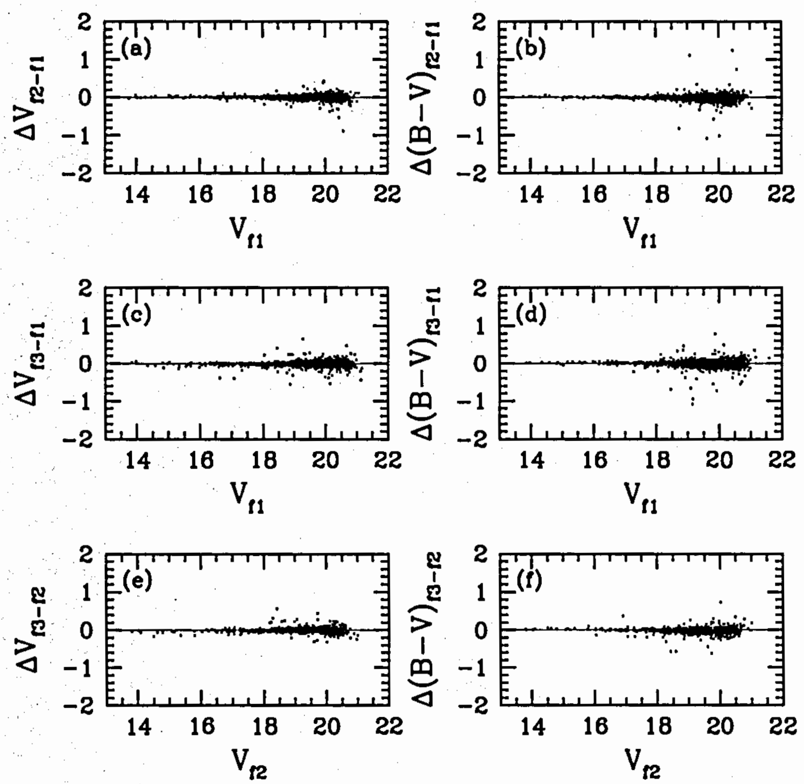

Figure 2.6 Comparisons of the program stars in the overlap regions between each pair of fields: (a) and (b) - the overlap between Fields 1 and 2, (c) and (d) - the overlap between Fields 1 and 3, (e) and (f) - the overlap between Fields 2 and 3. (a), (c), and (e) Differences in the V magnitude as a function of V magnitude. (b), (d), and (f) Differences in $(B-V)$ as a function of V magnitude.

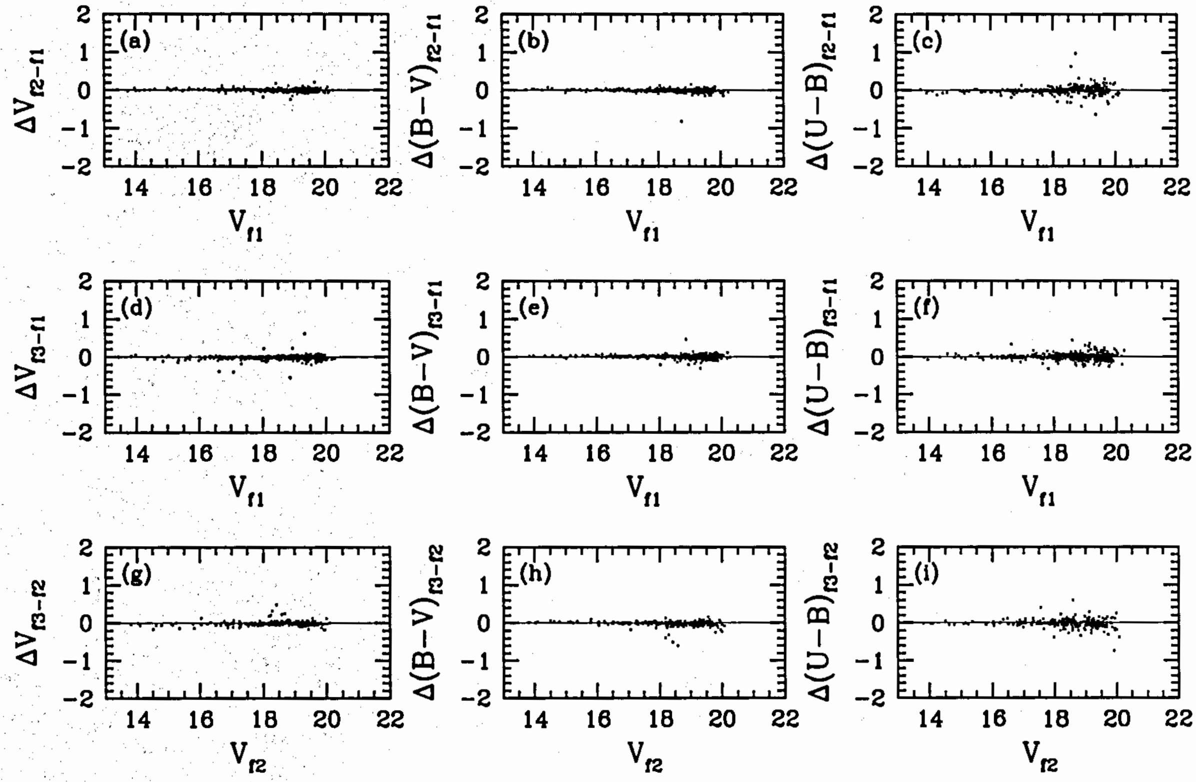

Figure 2.7 Comparisons of the program stars detected in all three bands in the overlap regions between each pair of fields: (a), (b), and (c) - the overlap between Fields 1 and 2, (d), (e), and (f) - the overlap between Fields 1 and 3, (g), (h), and (i) - the overlap between Fields 2 and 3. (a), (d), and (g) Differences in the V magnitude as a function of V magnitude. (b), (e), and (h) Differences in $(B - V)$ as a function of V magnitude. (c), (f), and (i) Differences in $(U - B)$ as a function of V magnitude.

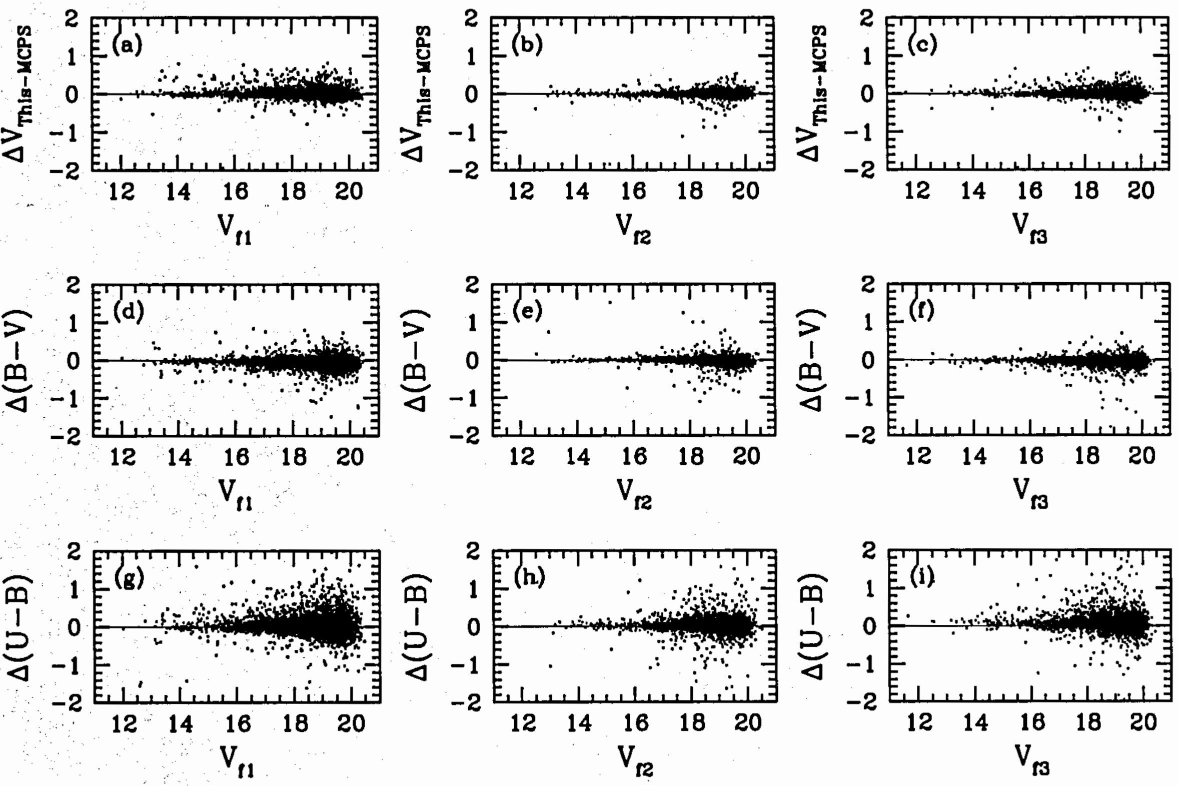

Figure 2.8 Comparisons of the program star photometry with the MCPS: (a), (d), and (g) stars in Field 1, (b,e,h) stars in Field 2, and (c), (f), and (i) stars in Field 3. (a), (b), and (c) Differences in the V magnitude as a function of V magnitude. (d), (e), and (f) Differences in $(B-V)$ as a function of V magnitude. (g), (h), and (i) Differences in $(U-B)$ as a function of V magnitude. The differences refer to (this work − the MCPS).

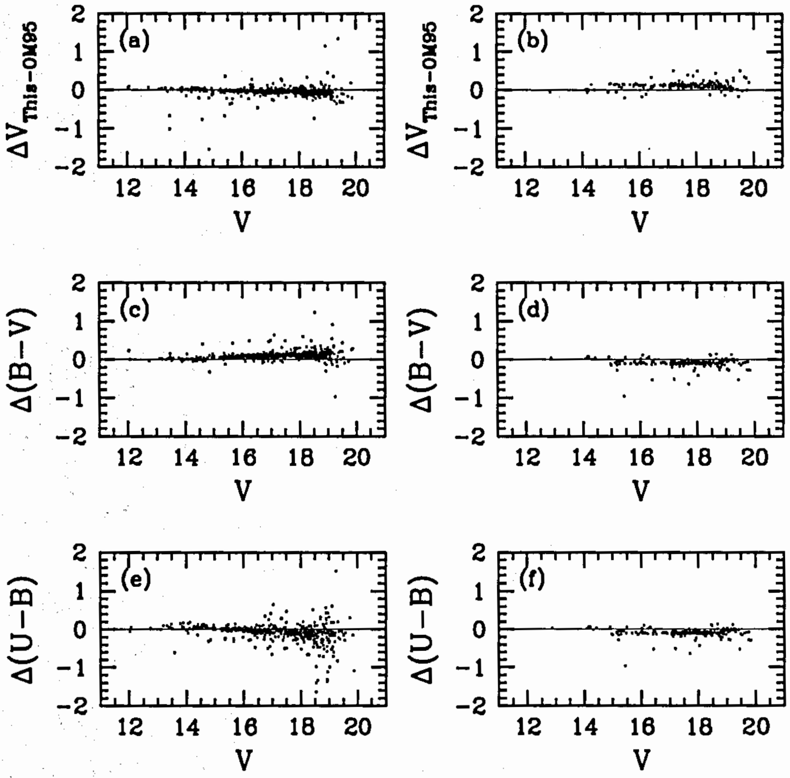

Figure 2.9 Comparisons of the program star photometry with the OM95 catalog: (a), (c), and (e) stars in LH47, (b), (d), and (f) stars in LH48. (a) and (b) Differences in the V magnitude as a function of V magnitude. (c) and (d) Differences in $(B-V)$ as a function of V magnitude. (e) and (f) Differences in $(U-B)$ as a function of V magnitude. The differences refer to (this work – the OM95 catalog).

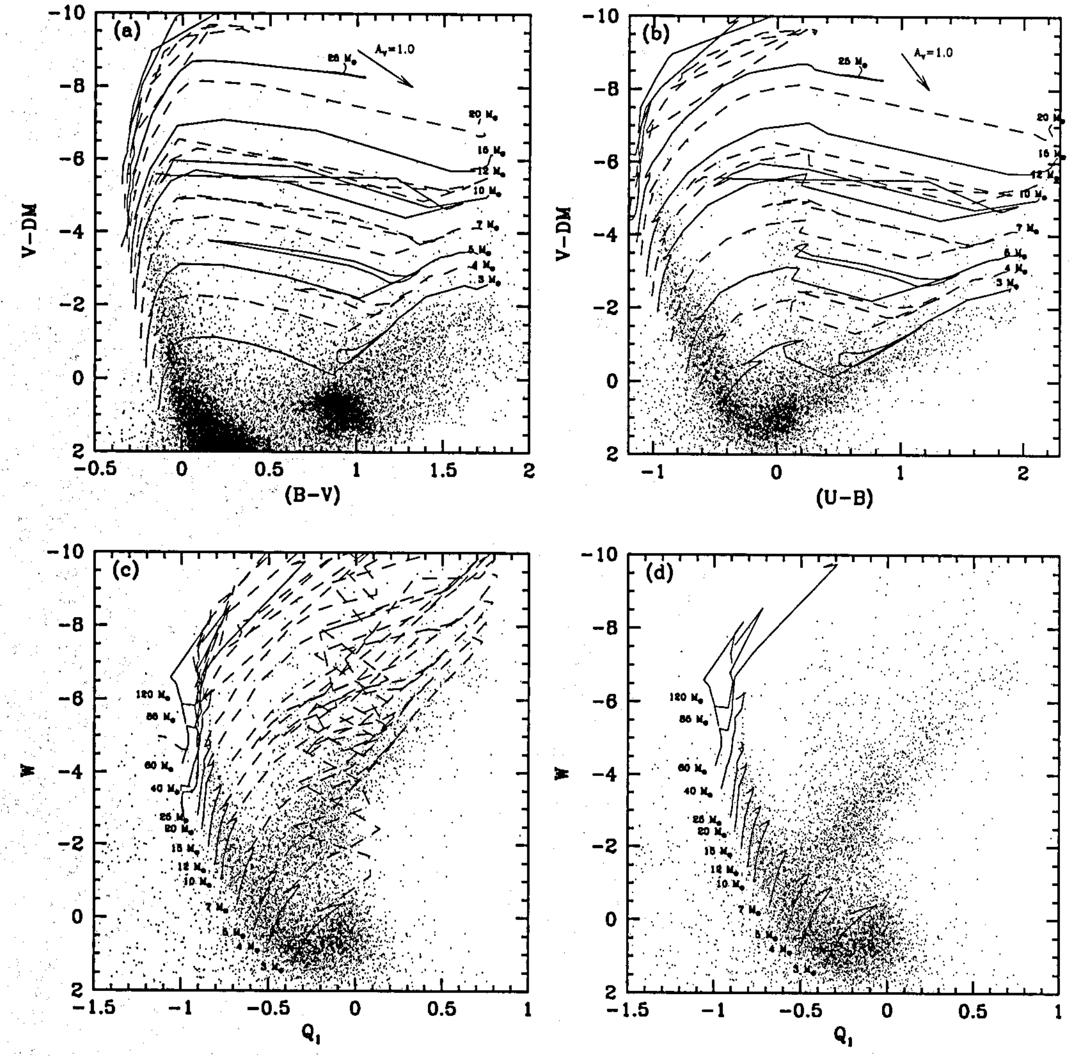

Figure 2.10 CMDs of all detected stars in N 44 in (a) $(V - DM)$ vs. $(B - V)$, (b) $(V - DM)$ vs. $(U - B)$, and (c)–(d) W vs. Q. In (a) and (b), stellar evolutionary tracks of different masses (Lejeune & Schaerer, 2001) are plotted alternately in solid and dashed lines to better distinguish adjacent tracks. The mass of each stellar model is labeled. In (c), each evolutionary track is shows as two segments: the MS phase (solid lines) and post-MS phase (dashed line). In (d), only the MS phase of the evolutionary tracks are plotted.

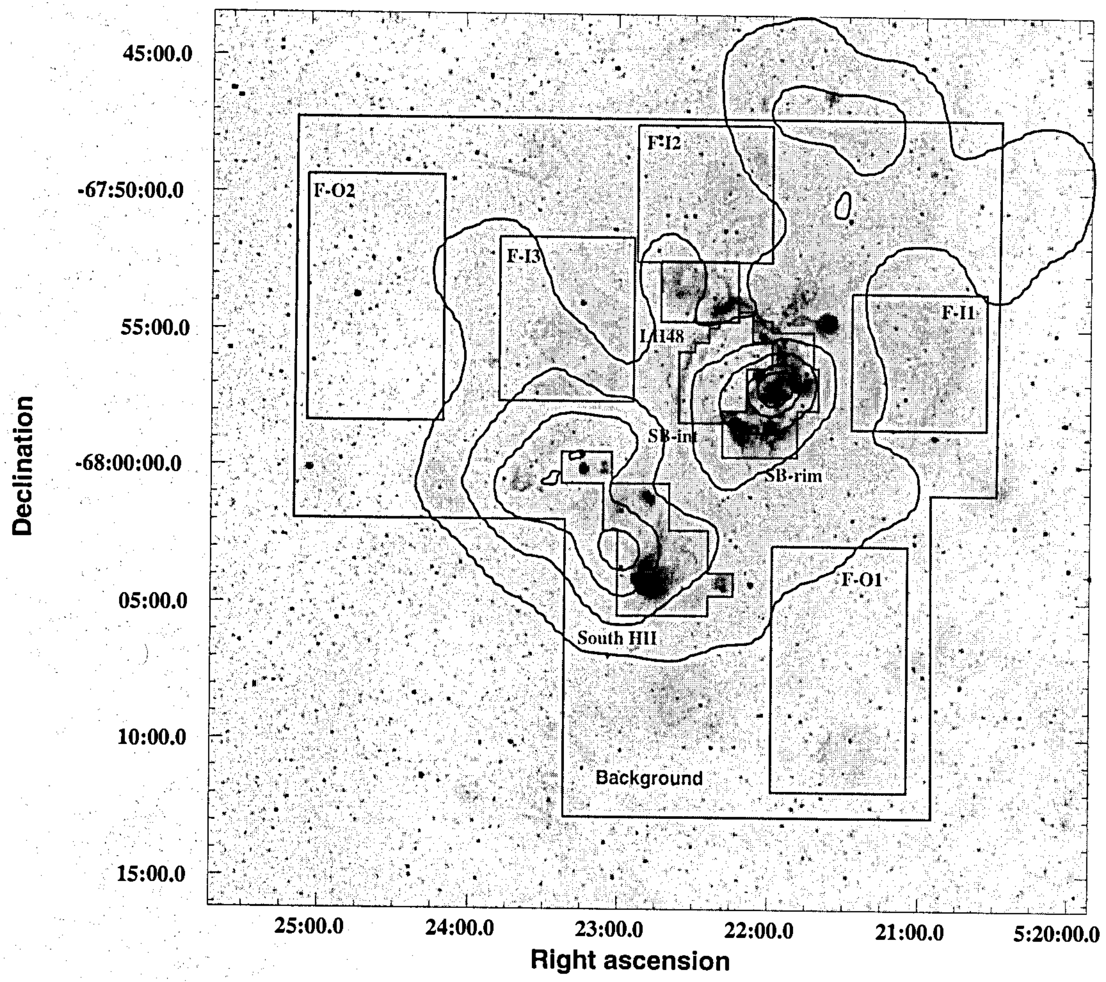

Figure 2.11 Star formation and field regions in N 44 used in determination of mass functions. These regions are marked on the MCELS Hα image of N 44. The image is also overlaid with CO contours (Fukui et al., 2001).

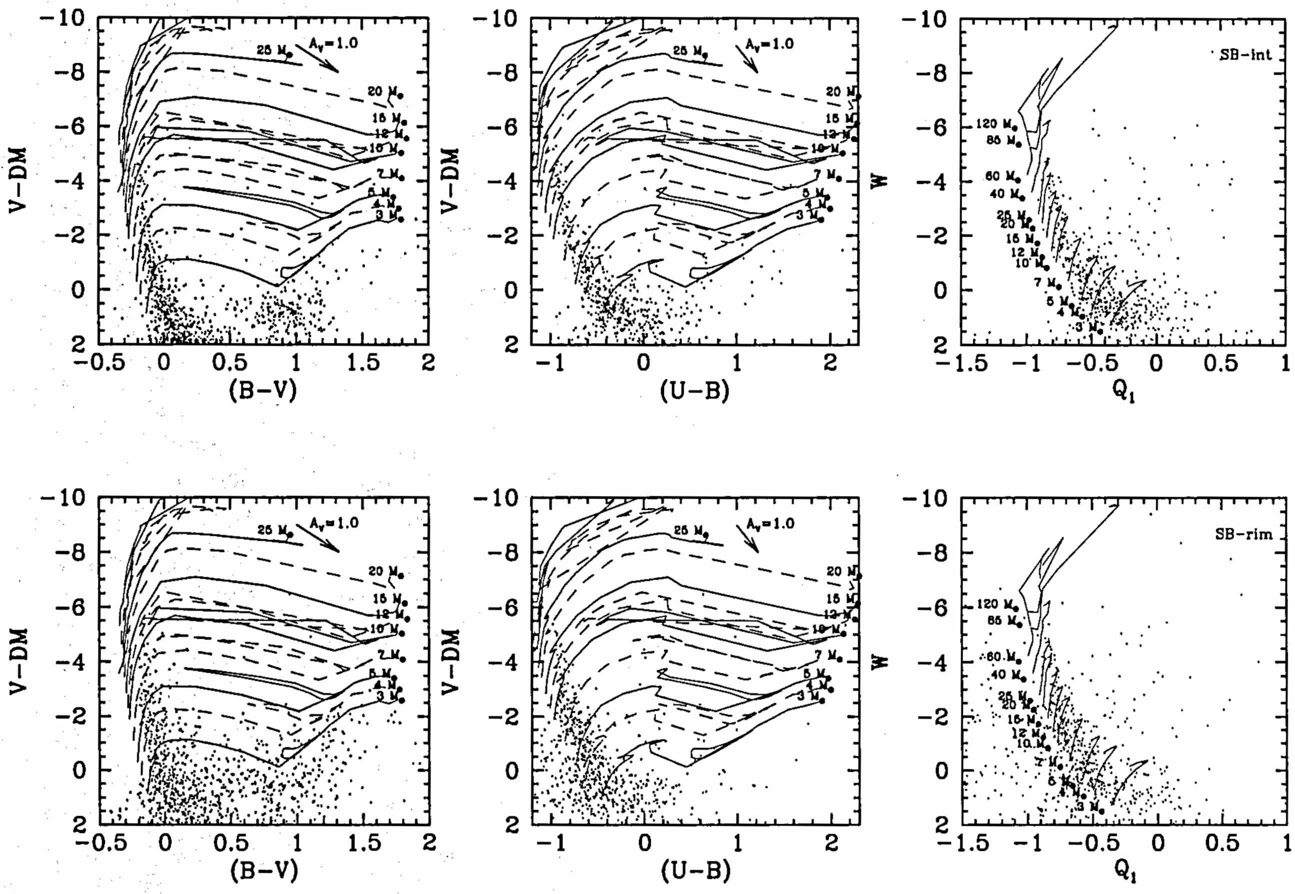

Figure 2.12 CMDs of stars in SB-int and SB-rim. Upper panels: SB-int. Lower panels: SB-rim. From left to right are CMDs in $(V - DM)$ vs. $(B - V)$, $(V - DM)$ vs. $(U - B)$, and W vs. Q. In the $(V - DM)$ vs. $(B - V)$ and $(V - DM)$ vs. $(U - B)$ CMDs, stellar evolutionary tracks of different masses (Lejeune & Schaerer, 2001) are plotted alternately in solid and dashed lines to better distinguish adjacent tracks. The mass of each stellar model is labeled. In the W vs. Q. CMD, only the MS phase of the evolutionary tracks are plotted.

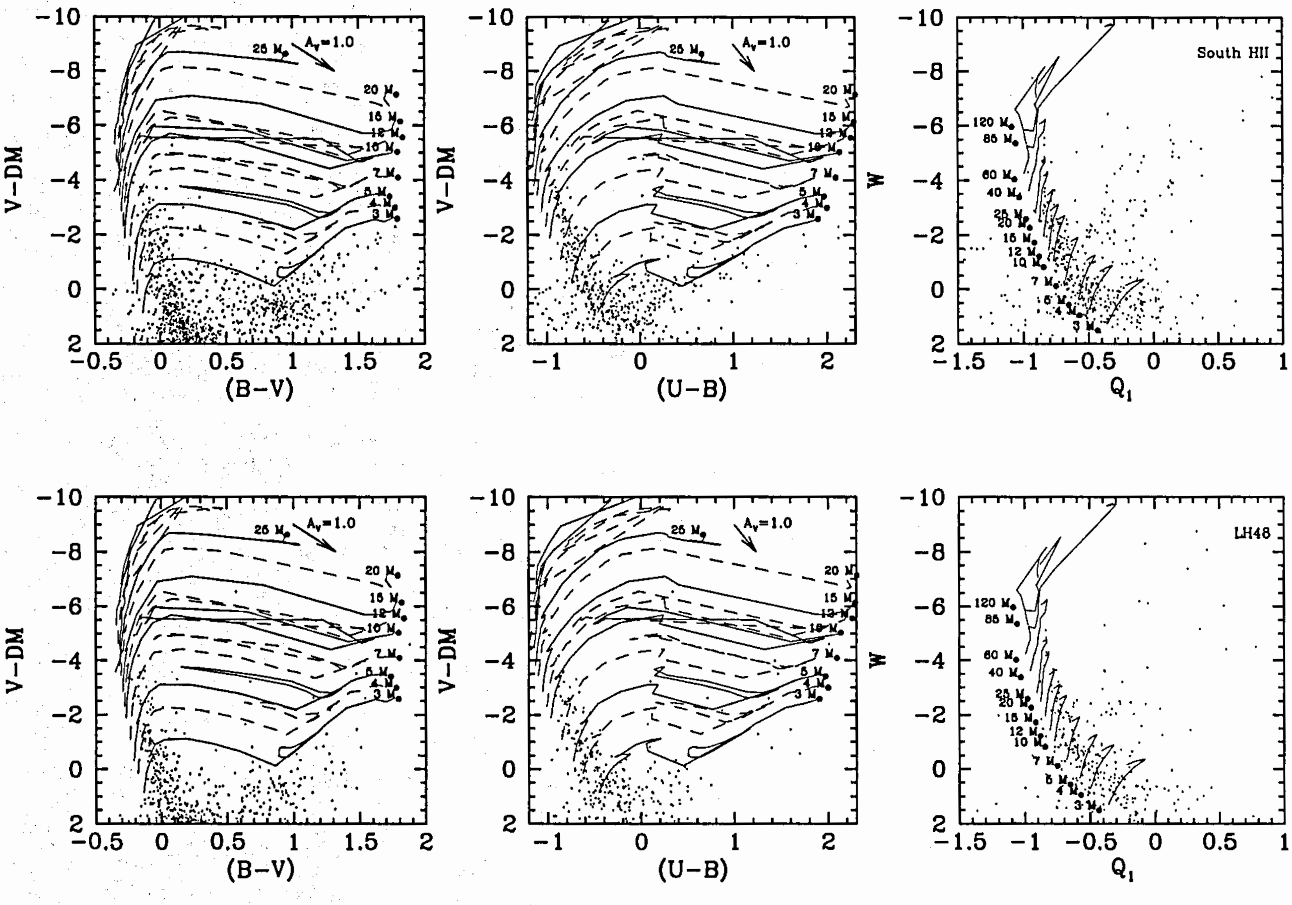

Figure 2.13 CMDs of stars in South H II and LH48. Upper panels: South H II. Lower panels: LH48. Individual plots mirror those in Fig. 2.12.

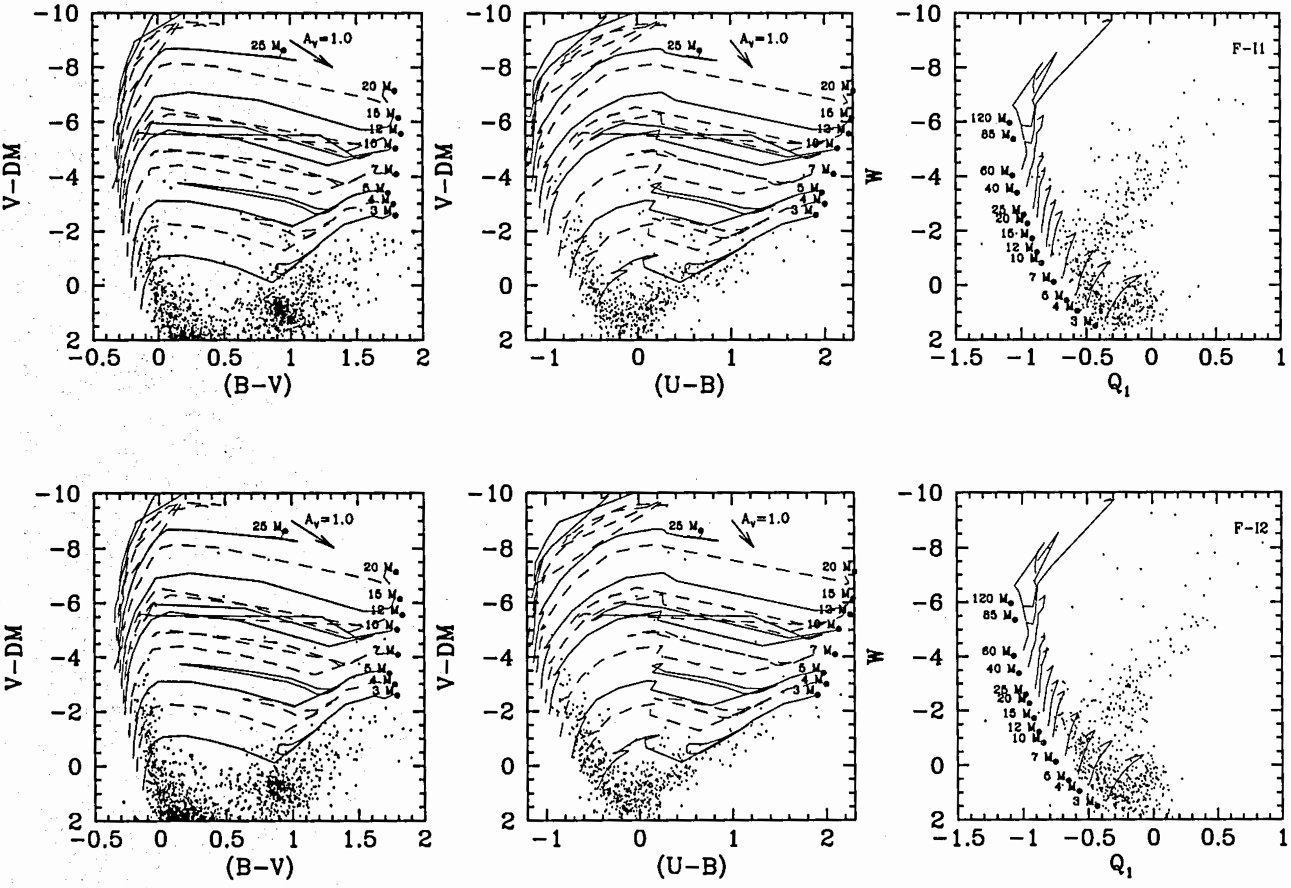

Figure 2.14 CMDs of stars in field regions F-I1 and F-I2. Upper panels: F-I1. Lower panels: F-I2. Individual plots mirror those in Fig. 2.12.

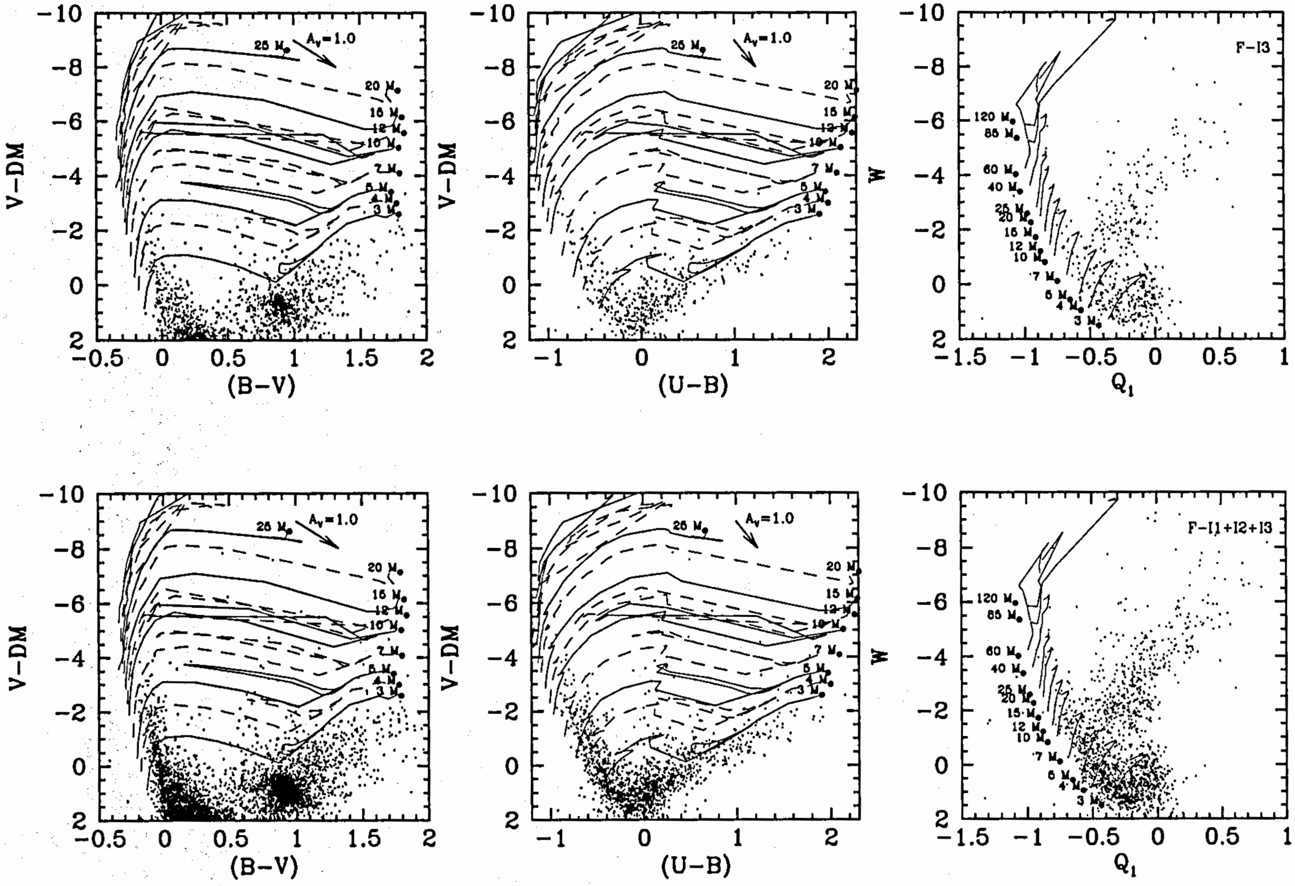

Figure 2.15 CMDs of stars in field regions F-I3 and F-I1+I2+I3. Upper panels: F-I3. Lower panels: F-I1+I2+I3. Individual plots mirror those in Fig. 2.12.

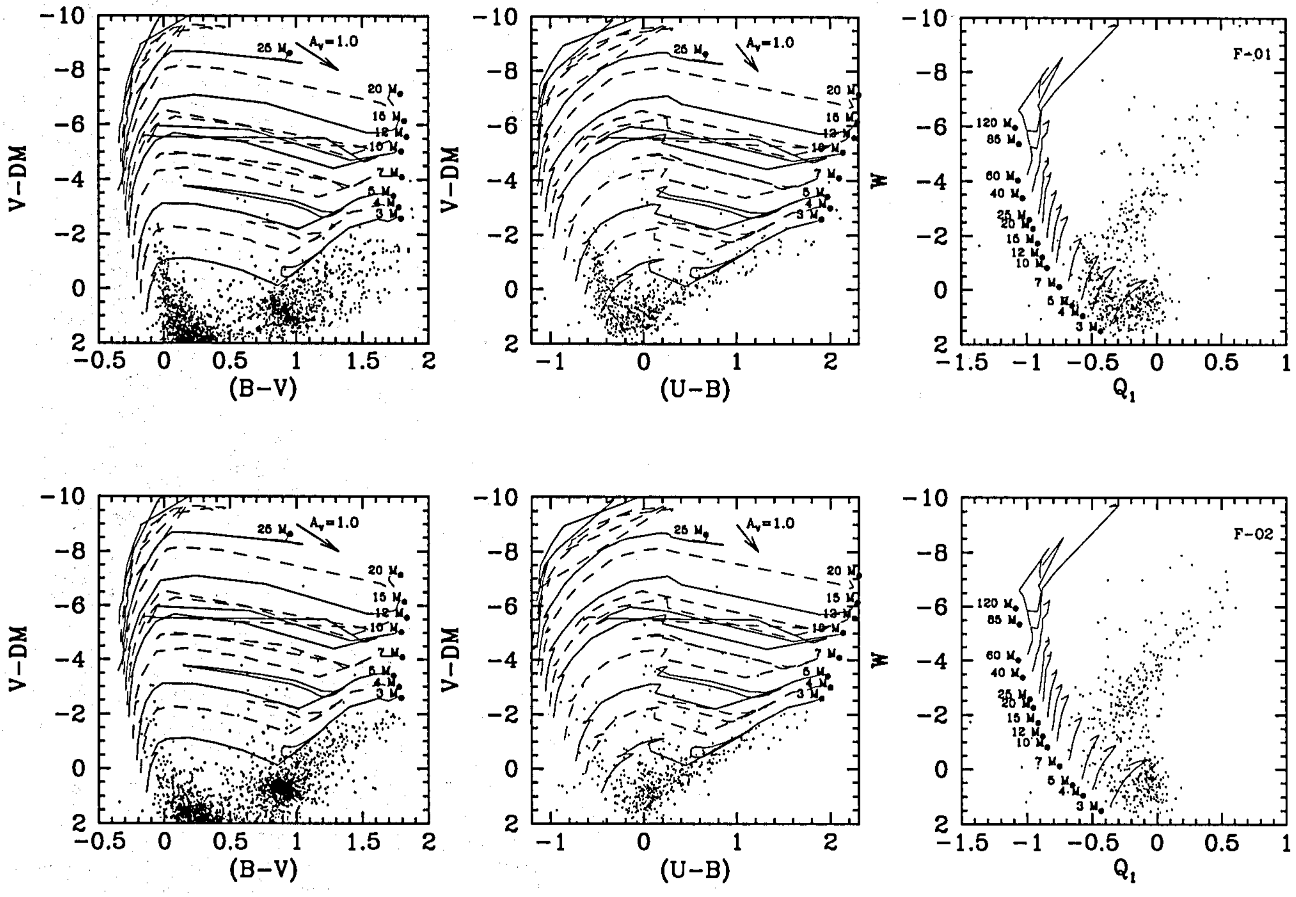

Figure 2.16 CMDs of stars in field regions F-O1 and F-O2. Upper panels: F-O1. Lower panels: F-O2. Individual plots mirror those in Fig. 2.12.

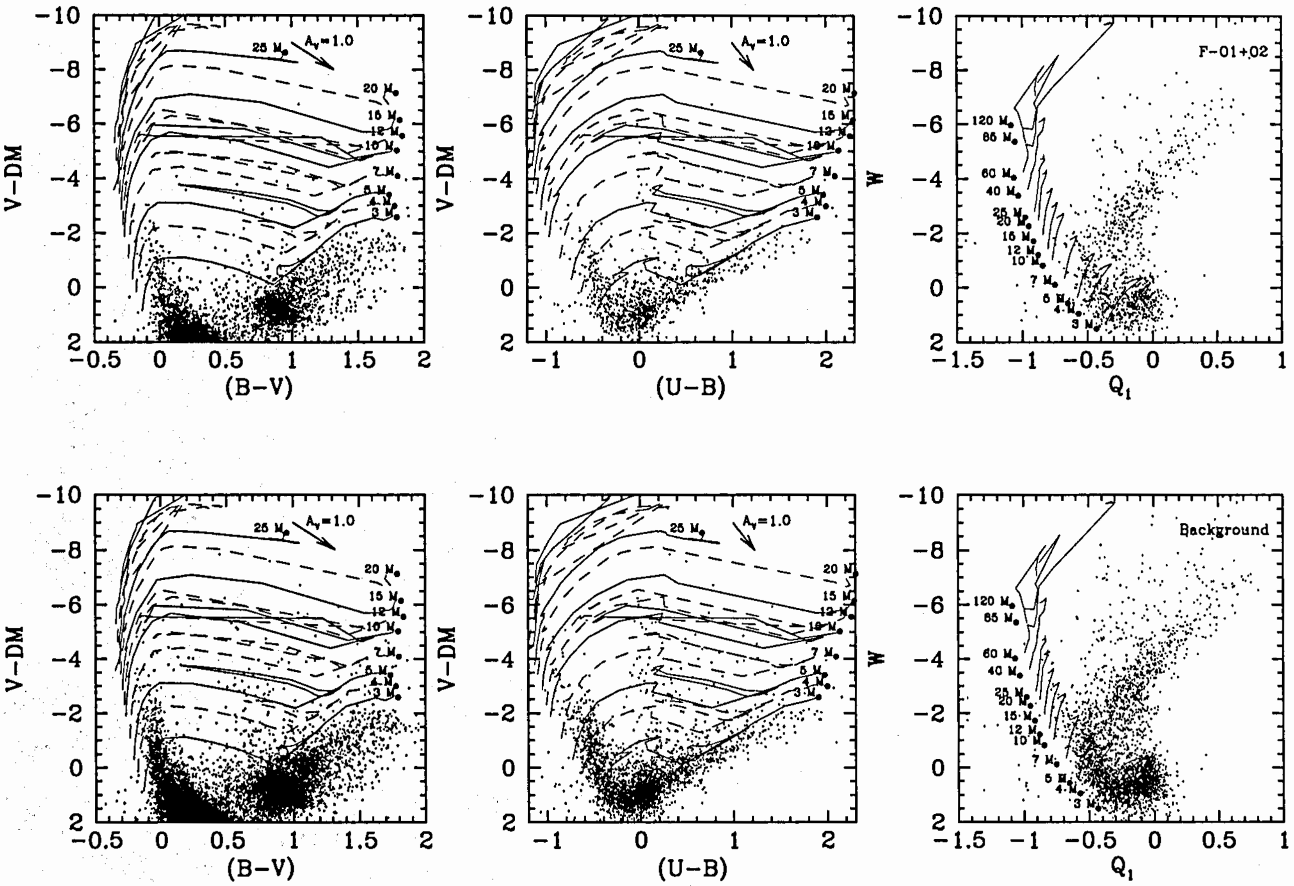

Figure 2.17 CMDs of stars in field regions F-O1+O2 and Background. Upper panels: F-O1+O2. Lower panels: Background. Individual plots mirror those in Fig. 2.12.

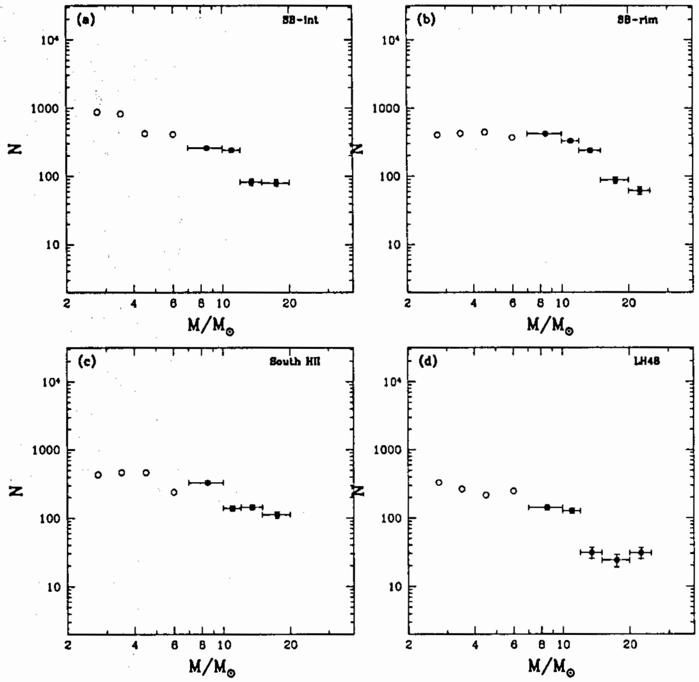

Figure 2.18 Mass functions of star formation regions. (a) SB-int, (b) SB-rim, (c) South H II, and (d) LH48. Mass bins that are not affected by incompleteness are shown in filled circles, while those might be affected in open circles. The uncertainties for the star counts are assumed to be $N^{0.5}$ while the error bar for stellar mass refers to the range of the mass bin.

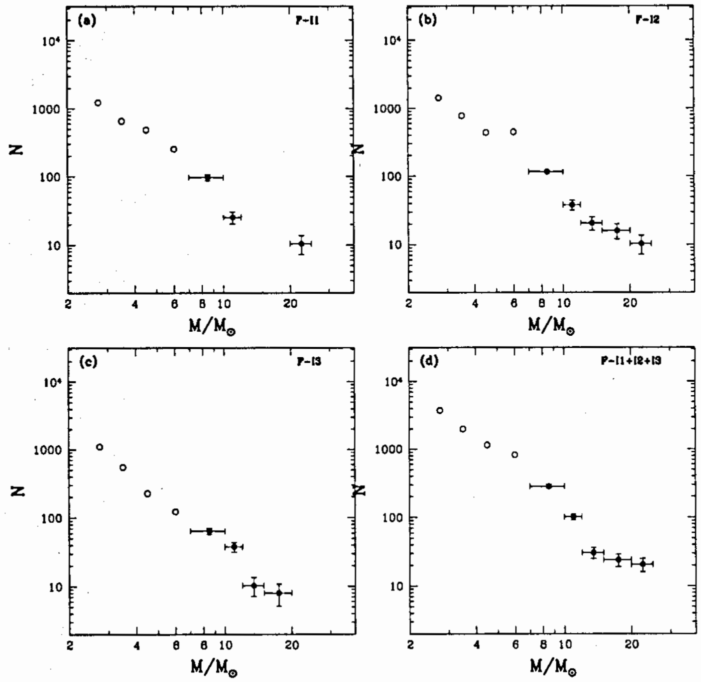

Figure 2.19 Mass functions of inner field regions. (a) F-I1, (b) F-I2, (c) F-I3, and (d) F-I1+I2+I3. Symbols are the same as Fig. 2.18.

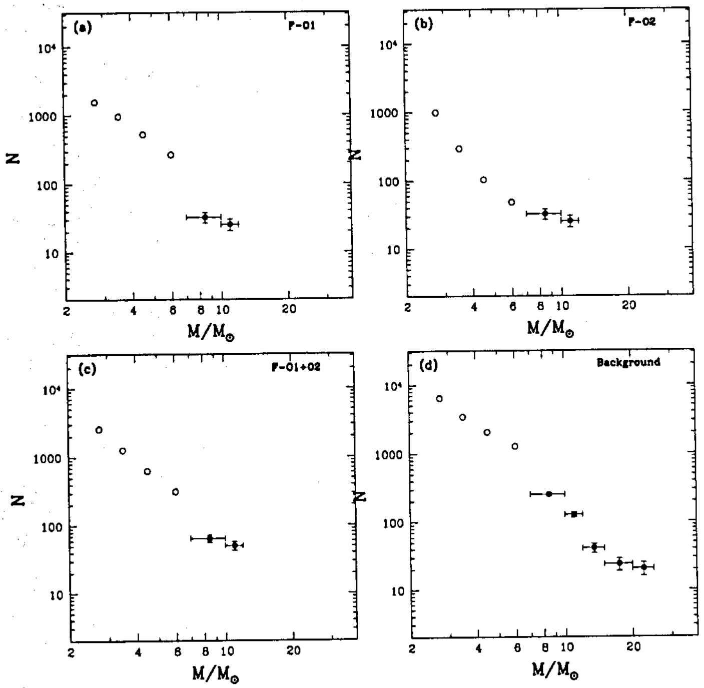

Figure 2.20 Mass functions of outer field and background regions. (a) F-O1, (b) F-O2, (c) F-O1+O2, and (d) Background. Symbols are the same as Fig. 2.18.

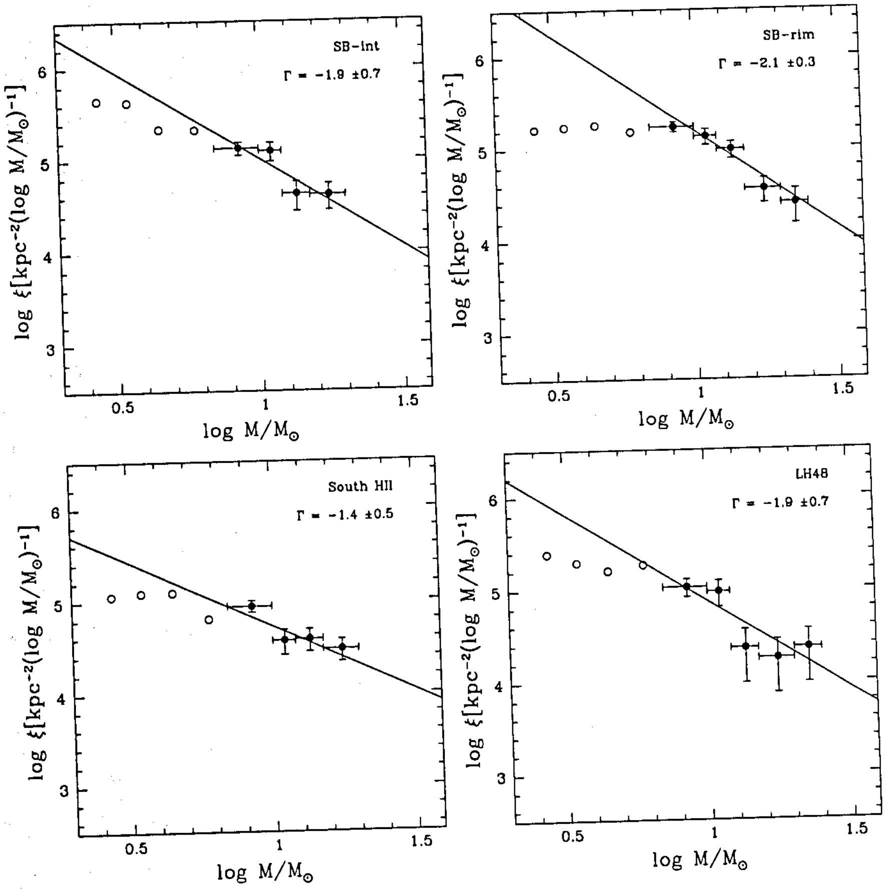

Figure 2.21 Slope to the PDMF of uncorrected star formation regions. (a) SB-int, (b) SB-rim, (c) South H II, and (d) LH48. Lower mass bins (open circles) were excluded from the fits. The uncertainties for the star counts are assumed to be $\sqrt{N}$ while the error bar for stellar mass refers to the range of the mass bin.

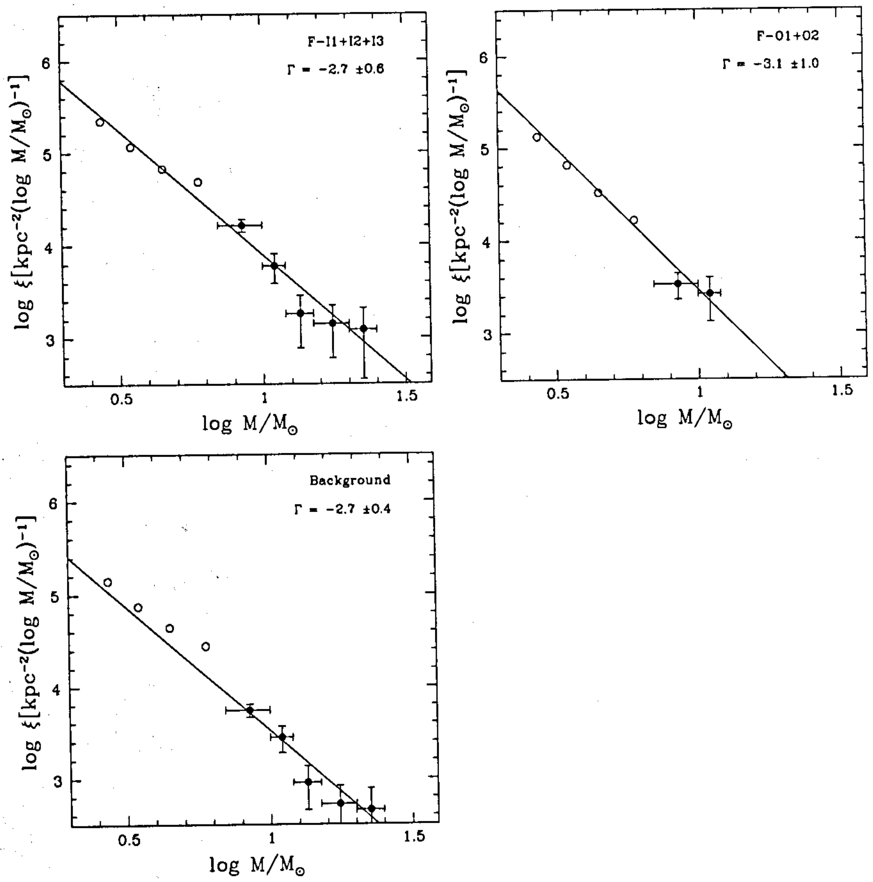

Figure 2.22 Slope to the PDMF of field regions. (a) F-I1+I2+I3, (b) F-O1+O2, and (c) Background. Lower mass bins (open circles) were excluded from the fits. The exception to the rule is the PDMF of F-O1+O2 as the $5 - 7M_\odot$ bin was included to obtain a statistical meaningful fit.

Table 2.1. Journal of UBV Photometry Observations

Field	R.A. J2000	Decl. J2000	Exposure (s) U	B	V
N 44 F1	05 21 43	-67 54 17	10	10	10
			60	40	30
			600	400	300
N 44 F2	05 23 54	-67 55 17	10	10	10
			60	40	30
			600	400	300
N 44 F3	05 22 09	-68 06 08	10	10	10
			60	40	30
			600	400	300

Table 2.2. Coefficients of Transformation Functions

Filter	Zero Point Coeff.	Extinction Coeff.	Color Coeff.	rms
U	3.80	0.54	-0.05	0.052
B	2.10	0.34	0.08	0.016
V	1.96	0.20	-0.02	0.009

Table 2.3. Mass Range and Main Sequence Star Counts for Star Formation Regions

Mass Range ($M_\odot$)	$\log(M_c/M_\odot)$	N SB-int	SB-rim	South HII	LH48
> 25	...	5	5	7	1
25 - 20	1.35	0	6	0	3
20 - 15	1.24	10	11	14	3
15 - 12	1.13	8	23	14	3
12 - 10	1.04	19	26	11	10
10 - 7	0.93	40	65	51	22
7 - 5	0.78	60	54	35	36
5 - 4	0.65	41	43	45	21
4 - 3	0.54	103	53	58	33
3 - 2.5	0.44	69	32	34	26

Table 2.4. Mass Range and Main Sequence Star Counts for Field Star Regions

Mass Range ($M_\odot$)	$\log(M_c/M_\odot)$	Background	F-O1+O2+O3	F-O1	*N* F-O2	F-I1+I2+I3	F-I1	F-I2	F-I3
> 25	...	1	0	0	0	4	1	1	2
25 - 20	1.35	2	0	0	0	2	1	1	0
20 - 15	1.24	3	0	0	0	3	0	2	1
15 - 12	1.13	4	0	0	0	3	0	2	1
12 - 10	1.04	10	4	2	2	8	2	3	3
10 - 7	0.93	39	10	5	5	43	15	18	10
7 - 5	0.78	185	46	39	7	120	37	65	18
5 - 4	0.65	197	61	51	10	111	47	42	22
4 - 3	0.54	426	157	120	37	248	82	97	69
3 - 2.5	0.44	507	202	124	78	298	98	113	87

Table 2.5. Mass Range and Field-Corrected Main Sequence Star Counts for Star Formation Regions

Mass Range		N							
($M_\odot$)	$\log(M_c/M_\odot)$	SB-int[a]		SB-rim[a]		South HII[a]		LH48[a]	
> 25	...	5	5	5	4	7	6	1	1
25 - 20	1.35	0	0	6	6	0	0	3	3
20 - 15	1.24	10	10	11	11	14	13	3	3
15 - 12	1.13	8	8	23	23	14	13	3	3
12 - 10	1.04	19	18	25	25	10	9	10	9
10 - 7	0.93	39	35	64	59	49	42	21	19
7 - 5	0.78	55	46	48	37	26	9	33	26
5 - 4	0.65	35	28	35	27	33	21	17	12
4 - 3	0.54	87	75	33	17	27	4	22	13
3 - 2.5	0.44	49	35	6	-11	-5	-31	12	2

[a] The left column lists star counts corrected with the combined outer field and right column corrected with the combined inner field.

Table 2.6. Linear Least-Square Fits to the Uncorrected and Corrected Star Formation Regions and Field Regions

Field	Γ	N[a]	N/pc^2
Uncorrected			
SB-int	-1.9 ± 0.7	77	4.1E-2
SB-rim	-2.1 ± 0.3	131	5.5E-2
South HII	-1.4 ± 0.5	90	2.5E-2
LH48	-1.9 ± 0.7	41	3.1E-2
Field-corrected[b]			
SB-int	-1.8 ± 0.7	76	4.1E-2
SB-rim	-2.1 ± 0.3	129	5.4E-2
South HII	-1.4 ± 0.6	87	2.4E-2
LH48	-1.9 ± 0.7	40	3.0E-2
Field			
F-I1+I2+I3	-2.7 ± 0.6	59	3.6E-2
F-O1+O2	-3.1 ± 1.0	60[c]	3.2E-2
Background	-2.7 ± 0.4	58	1.3E-2

[a] Number of stars used to determine the slope of the mass function.

[b] Only the fits to the PDMF with correction made with the combined outer field are listed. The fits resulted from corrections made with combined inner field have similar results.

[c] The fit to the mass function includes an additional $5 - 7 M_\odot$ bin for better statistics.

Chapter 3

Massive Stars in the H II Complex N 44. II. the Current Star Formation

3.1 Introduction

Star formation frequently takes place in high concentrations and at intense levels, called "starbursts." The massive stars in a starburst can inject energies into the interstellar medium (ISM) to photoionize the ambient medium and to dynamically sweep up the medium into expanding shells. The expanding shells can trigger subsequent star formation either by compressing ambient dense clouds or by collect-and-collapse within the shell (Elmegreen 1998). Starbursts can easily spread over areas 10^2-10^3 pc across, and play a vital role in determining the large-scale structures of their host galaxies.

While starbursts are the most prominent features in a galaxy, their detailed properties cannot be easily studied: in distant galaxies the stellar content is not resolved and in the Milky Way the distances and association among stars in a starburst are uncertain. The Large and Small Magellanic Clouds (LMC & SMC; MCs) are the only galaxies in which stars are at common, known distances and can be individually resolved down to $\sim 1\ M_\odot$ at optical wavelengths. Recent *Spitzer* mid-infrared (IR) observations enabled the detection of individual young stellar objects (YSOs) in the MCs, revealing the on-going star formation. It is now possible to use the resolved stellar population to map out star formation as a function of space and time in the MCs. As the ISM of the MCs has been surveyed in great detail, it is further possible to determine the relationship between star formation and the physical conditions and properties of the ISM. Consequently, studies of starbursts in the MCs allow us to answer fundamental questions about star formation, such as:

- Does the initial mass function (IMF) vary in slope and mass range?
- Is current star formation triggered by the energy feedback from stars formed earlier?

The largest HII regions in the MCs, 30 Dor in the LMC and NGC 346 in the SMC, have been the targets of intensive studies; however, 30 Dor is too complex for an unambiguous analysis of the astrophysical processes and its central stellar density exceeds the crowding limit even for *HST*, and NGC 346 is too young to have extended over several 10^2 pc. A suitable region to study the multiple facets of star formation in a starburst needs to have multiple generations of star formation in the sky plane (as opposed to along the line-of-sight) within a manageable area. LHα 120-N 44 (N 44; Henize, 1956) in the LMC is an ideal choice.

N 44 is one of the three largest HII complexes in the LMC. It contains three OB associations, LH47, 48, and 49 (Lucke & Hodge, 1970), that are in different evolutionary stages and interstellar structures: LH47 in the central superbubble, LH48 in one contiguous HII region at the northeast rim of the superbubble, and LH49 in a group of HII regions to the southeast exterior of the superbubble (Figs. 3.1a,b). Along the western rim of the superbubble exist a number of dense HII regions where star formation may have been triggered by the expansion of the superbubble (Oey & Massey, 1995). Surveys of CO in the N 44 complex (Fig. 3.1c; Fukui et al., 2001) show two high concentrations of molecular material at the western rim of the central superbubble and at the HII regions around LH49, and a weaker concentration to the north of the superbubble where no OB associations are identified although a few small isolated HII regions are visible.

The effects of stellar energy feedback are evident in N 44. The Hα image (Fig. 3.1a) shows the reach of stellar UV radiation. The X-ray image (Fig. 3.1d) reveals 10^6 K gas heated by fast stellar winds and supernova explosions. While the expansion of the central superbubble may have triggered the intense star formation along its western rim, the hot gas outflow from the superbubble may be responsible for the onset of star formation at the northeastern extension of the south molecular peak.

To determine the relationship between the interstellar conditions and the stars formed, we use massive young stellar objects (YSOs) because they are still embedded in dense circumstellar material and thus have not significantly altered the physical conditions of their ambient medium. YSOs are most easily identified by the mid-IR emitted from their circumstellar envelopes. The advent of the *Spitzer Space Telescope* makes it possible to search for massive YSOs in the LMC. We have been awarded *Spitzer* Cycle 1 observations of N 44. This chapter reports the *Spitzer* observations of N 44 and how they are used to search for YSOs. Multi-wavelength observations are used to probe the nature of the YSO candidates, and associate YSOs with their stellar and interstellar environments. The results allow us to probe whether different interstellar conditions lead to the formation of stars with different mass functions, and whether star formation is truly triggered dynamically.

3.2 Observations and Data Reductions

We have used *Spitzer* mid-IR observations to diagnose YSOs. To extend the spectral energy distribution (SED) and to improve the angular resolution, we have also obtained ground-based optical and near-IR imaging observations of N 44. We have also searched for images in the *HST* archive, and used the available images to examine the optical counterparts and environments of the YSO candidates.

3.2.1 *Spitzer* IRAC and MIPS Observations

Our *Spitzer* observations of N 44 were made with the InfraRed Array Camera (IRAC; Fazio et al., 2004) on 2005 March 27 and the Multiband Imaging Photometer for *Spitzer* (MIPS; Rieke et al., 2004) on 2005 April 7. The IRAC observations were obtained using the mapping mode in the 3.6, 4.5, 5.8, and 8.0 μm bands. The mapping covers a $\sim 30' \times 30'$ area in each band, but the common area covered by all four bands is $\sim 30' \times 23'$. At each pointing, exposures were made with a five-point cyclic dithering pattern in the 30 s high dynamic range mode. The total integration time at each pointing is $\sim$ 150 s. The mosaicked maps were processed with the Spitzer Science Center pipeline (ver. S11.4.0) and provided to us as part of the Post Basic Calibrated Data (PBCD) products.

The MIPS observations were made using the scan map mode at the medium scan rate in the 24, 70, and 160 μm bands. The mapping consists of sixteen $0\overset{\circ}{.}5$ scan legs with a cross-scan step of $148''$ to cover a region of $24' \times 50'$ in all three MIPS bands. The MIPS DAT version 3.00 (Gordon et al., 2005) was used for the basic processing and final mosaicking of the individual images. In addition, the 24 μm image has been corrected for a readout offset and divided by a scan-mirror-independent flat field, and the 70 and 160 μm images have been corrected for a pixel-dependent background using a low-order polynomial fit to the source-free regions. The final mosaicked maps have exposure times of roughly 160, 80, and 16 s at 24, 70, and 160 μm, respectively.

Aperture photometry for point sources in the IRAC images was carried out using the IRAF package `apphot`. The sources were identified with the automated source finding routine `daofind`, using parameters optimized to find the majority of point-like sources while minimizing the inclusion of peaks of dust clumps. Some regions contain multiple sources superposed on extended emission, and `daofind` does not always identify the same sources at the same locations in all four IRAC bands. Therefore, we identified sources in each of the four IRAC bands, merged the four source lists into a master source list, and used this master list for photometric measurements in all four bands. The photometric measurements were made with a source aperture of 3-pixels ($3\overset{''}{.}6$) radius and an annular background aperture at radii of 3–7 pixels ($3\overset{''}{.}6$–$8\overset{''}{.}4$). An aperture correction was applied, and the fluxes were converted into magnitudes using the correction factors and zero-magnitude fluxes provided in the IRAC Data Handbook (see Table 3.1).

The photometric measurements from long- and short-exposure IRAC observations were averaged with weights proportional to the inverse square of their errors. For sources that were saturated in the long exposures, their measurements from the short exposures were adopted. The results were used to produce a photometric catalog of 36,711 sources detected in the IRAC observations of N 44. Not all sources were detected in all four bands. As our IRAC 3.6 and 5.8 μm observations did not extend as far north as the other IRAC and MIPS observations, we used the *Spitzer* survey of the LMC (SAGE, Meixner et al., 2006) to complete the coverage in these two IRAC bands.

MIPS images have lower angular resolution. Source identification using `daofind` is practical only for the 24 μm images. In the 70 and 160 μm images, point sources cannot be easily resolved from one another or from a bright diffuse background; therefore, the few apparent point sources were identified by visual inspection. The photometric measurements were made with parameters appropriate for the point spread functions (PSFs), as recommended in the MIPS Data Handbook and given in Table 3.1. Note that the aperture corrections adopted for 70 and 160 μm measurements are those for sources of temperatures 15 and 10 K, respectively. For sources of higher temperatures, such as 1000–3000 K, the adopted aperture corrections will result in fluxes 8% too high in 70 μm and 2% too high in 160 μm because the source emission peaks at shorter wavelengths; however, these errors do not significantly affect the analysis and conclusions of our study of YSOs.

The *Spitzer* images of N 44 in the 3.6, 8.0, and 24 μm bands are shown in Figure 3.2. The 3.6 μm image is dominated by stellar emission, the 8.0 μm image shows the polycyclic aromatic hydrocarbon (PAH) emission, while the 24 μm image is dominated by dust continuum emission (Li & Draine, 2001, 2002). To better illustrate the relative distribution of emission in the different bands, we have produced a color composite with 3.6, 8.0, and 24 μm images mapped in blue, green, and red, respectively. In this color composite, shown in Figure 3.2d, dust emission appears red and diffuse, stars appear as blue point sources, red supergiants appear yellow, and dust shrouded YSOs and AGB stars appear red.

3.2.2 CTIO 4 m ISPI and MOSAIC Observations

We obtained near-IR images in the J and K_s bands with Infrared Side Port Imager (ISPI) on the Blanco 4 m telescope at Cerro Tololo Inter-American Observatory (CTIO) on 2005 November 14–15. The images were obtained with the 2K × 2K HgCdTe HAWAII-2 array, which had a pixel scale of $0\farcs3$ pixel^{-1} and a field-of-view of $10\farcm25 \times 10\farcm25$. Six fields were observed to map the main H II complex of N 44. Each field was observed with ten 30 s exposures in the J band and twenty 30 s exposures (which was coadded from two 15 s frames to avoid background saturation) in the K_s band. The observations were dithered to aid in sky subtraction and removal of transients and chip defects. All images were processed using the IRAF package `cirred` for dark and sky subtraction and flat-fielding. The astrometry of individual processed images was solved with the routine `imwcs` in the IRAF package `wcstools`. The astrometrically calibrated images are then coadded to produce a total exposure map for each filter. The flux calibration was carried out using 2MASS photometry of isolated sources.

We obtained *UBVI* broadband images of N 44 with the MOSAIC II CCD Imager on the CTIO Blanco 4 m telescope on 2006 February 2. The MOSAIC Imager consists of eight 2K × 4K SITe CCDs. The CCDs have a pixel scale of $0\farcs27$ pixel^{-1}, yielding a total field-of-view of $36' \times 36'$. The entire N 44 was imaged in a single field. All *UBVI* images have been processed with the standard reduction procedure: bias and dark were subtracted, flat-fielding was applied, and multiple frames in each filter were combined to remove cosmic rays and improve the S/N. The astrometry for the processed images were performed by referencing to stars in the USNO B1.0 catalog. The flux calibration was carried out by bootstrapping from photometric measurements made in Chapter 2 and Zaritsky et al. (2004).

3.2.3 Archival *HST* Images

Archival *HST* Wide Field Planetary Camera 2 (WFPC2) images of N 44 taken with continuum or emission-line filters are available for six fields from five GO programs with proposal IDs of 6253, 6540, 6623, 6698, and 7553. These archival images have been retrieved and further processed. Multiple exposures with the same pointing and filter are combined using the IRAF routine `crrej` to remove cosmic rays. Astrometric corrections for each image have been refined, using reference stars from the USNO B1.0 catalog.

3.3 Identification of Massive YSOs

YSOs show different spectral energy distribution (SED) from stars because YSOs are shrouded in dust which absorbs the stellar radiation and irradiates at IR wavelengths; therefore, it is possible to identify YSOs from their IR excess. For high-mass YSOs, the distribution of circumstellar dust is not well known because too few objects have been found and the formation mechanism for massive stars is still uncertain (e.g, Stahler et al., 2000). It is not even known whether massive YSOs have accretion disks ubiquitously (e.g., Cesaroni et al., 2007).

We will use the commonly accepted physical structure and evolution of low-mass YSOs as a starting point for interpreting the SEDs of higher-mass YSOs. Low-mass YSOs are believed to be initially surrounded by a small accretion disk and a large infalling envelope with bipolar cavities, and as YSOs evolve, they clear the envelope and disk. This process results in different SEDs that have been used to classify low-mass YSOs in an evolutionary sequence, i.e., the Class I/II/III system (Lada, 1987). In this classification system, a Class I YSO has a compact accretion disk and a large infalling envelope with bipolar cavities; its SED is dominated by emission from the envelope and rises long-ward of 2 μm. A Class II YSO has dispersed most of its envelope and is surrounded by a flared disk; its SED, dominated by emissions from the central source and disk, is flat or falls long-ward of 2 μm. A Class III YSO has cleared most of the disk so its SED shows a reddened blackbody with little or no excess in near-IR.

The geometries of dust disk and envelope of low-mass YSOs have been adopted in the radiative transfer models of high-mass YSOs by a number of investigators (e.g., Whitney et al., 2004b; De Buizer et al., 2005; Robitaille et al., 2006). In their models, at an early evolutionary stage when the YSO is embedded in a large envelope with small opening angle, the predicted SED is dominated by emission from the envelope and shows a generally rising trend from the shortest detectable wavelength to beyond 24 μm. At an intermediate evolutionary stage when the opening angle of the envelope increases and the stellar and disk emissions may be exposed, the predicted SED for the YSO has one peak (stellar emission) below ~ 1 μm with its intensity dependent of the viewing angle, and another peak rising long-ward of 1 μm but turning flat or falling at around 10-20 μm. At a late evolutionary stage when most of the envelope and disk have been dispersed, the SED shows a bright stellar emission with a modest mid-IR excess. These models provide useful links between circumstellar dust structures and SEDs; thus, we will use the general trends of the SEDs to identify YSO candidates in N 44.

To construct SEDs for the sources in our *Spitzer* photometric catalog, we have expanded the catalog by adding photometric data from 1) our UBV catalog (Chapter 3), 2) the Magellanic Cloud Photometric Survey (Zaritsky et al., 2004) for regions not covered in our UBV observations, 3) the Point Source Catalog in the JHK_s bands of the Two Micron All Sky Survey (2MASS, Skrutskie et al., 2006), and 4) our 24 and 70 μm catalogs. When merging the datasets, we allow a $1''$ error margin for matching sources in optical and near-IR catalogs, and $4''$ for 24 μm and $8''$ for 70 μm catalogs to account for their large pixel scales. The final catalog lists each source's right ascension, declination, magnitude, and photometric uncertainty in the $UBVJHK_s$, 3.6, 4.5, 5.8, 8.0, 24, and 70 μm bands, and is included as part of the multi-wavelength catalog for *Spitzer* sources in the LMC (Gruendl & The Illinois Team, 2007). For constructions of SEDs, magnitudes are converted to flux densities using the corresponding zeroth-magnitude flux listed in Table 3.1 and 3.2.

3.3.1 Selection of Massive YSO Candidates

YSO candidates are commonly diagnosed with an IR excess compared to stellar radiation. This IR excess makes YSOs lie in the redder part of the color-color and color-magnitude diagrams (CC and CMDs) than normal stars. However, red sources are not just YSOs, but also background galaxies and asymptotic giant branch (AGB) stars. Furthermore, the numbers of both kinds of contaminants are not negligible. We have thus examined several CC diagrams and CMDs with solely IRAC bands as well as combinations of IRAC with JHK_s or MIPS bands, to determine the color indices that are most effective in separating YSOs from the contaminants. The [8.0] vs. ([4.5]−[8.0]) CMD is among the most effective ones; such a CMD of all sources detected in N 44 is shown in Figure 3.3. The prominent vertical branch centered at ([4.5] − [8.0]) ∼ 0 consists of mostly main-sequence (MS), giant, and supergiant (SG) stars. In the lower right of the CMD lie background galaxies and low-mass YSOs[1], while in the upper right lie AGB stars and higher-mass YSOs.

To obtain a sample of YSO candidates, we have first applied the statistical criteria from Harvey et al. (2006), ([4.5]−[8.0]) > 0.5 and [8.0] < 14.0−([4.5]−[8.0]), to exclude stars and background galaxies. As background galaxies and low-mass YSOs share the same lower right part of the CMD, the latter are thus also excluded. In fact, low-mass YSOs are likely to be the majority of the sources in this part of the CMD since the total number of these sources is ∼ 960, and the expected number of background galaxies, based on a number density of 0.05 arcmin^{-2} (Harvey et al., 2006; Gruendl & The Illinois Team, 2007) and a field coverage of 900 arcmin^2, is only 45.

The sources passed the first set of criteria need to be separated between evolved stars and YSOs. We have used known AGB and post-AGB stars within the field of N 44 and also theoretical models as a guidance. These known objects are searched through the SIMBAD database and then cross-identified with our catalog of all sources using a match radius 10.″0. When a match circle encloses multiple sources in our catalog, the closest one is chosen to be the true match. Thirty evolved stars are cross-identified in our catalog and marked in the [8.0] vs. ([4.5]−[8.0]) CMD, along with expected loci based on models for C- and O-rich AGB stars (Groenewegen, 2006). Among these evolved stars, twenty six are bona fide AGB stars at early and late evolutionary stages, such as carbon stars, M-type variables, IR carbon stars, and OH/IR stars. They have ([4.5] − [8.0]) < 1.5, well within that expected from AGB models. The remaining four with ([4.5] − [8.0]) > 1.5 are three AGB/post-AGB/planetary nebula (PN) candidates and one obscured AGB/SG star classified from their *IRAS* colors (Loup et al., 1997) or near-IR variability (Wood et al., 1992). The reddest one of the four, IRAS 05242−6748 = LI-LMC 855 (Loup et al., 1997), has ([4.5] − [8.0]) ∼ 4.5. However, this red color is not centered on the nearby optical star but on a diffuse, discrete clump resolved in our ISPI K_s image, making its identity as an AGB star uncertain. The other three objects, IRAS 05190−6748 = LI-LMC 957, IRAS 05216−6753 = LI-LMC 861, and IRAS 05240−6809 = LI-LMC 948, have ([4.5] − [8.0]) = 3.69, 2.84, and 1.83, demonstrating that the colors of AGB stars/candidates can span a wide range.

We further use SEDs to evaluate the effectiveness of the [4.5]-[8.0] = 2.0 criterion for excluding evolved stars. Example SEDs of various types of AGB stars/candidates are shown in Figure 3.4, including early and late stage C- and O-rich AGB stars, AGB/post-AGB/PN candidates, and obscured AGB/SG star. All SEDs but one show a blackbody with peak below 8 μm or a blackbody composite with a nearly flat slope

---

[1] Low-mass YSOs such as those in the Serpens cloud (Harvey et al., 2006) would have [8.0] ∼ 15.5 and fainter, close to the detection limit.

from ~ 2 to 8 μm, consistent with dust temperatures of $\sim 400 - 1,000$ K observed in Galactic AGB stars (Rowan-Robinson et al., 1986). These SEDs are obviously different from those of high-mass YSO models and thus can be readily used to separate them from YSOs. On the other hand, AGB candidates with a rising SED at 1–8 μm, such as LI-LMC 861 (Fig. 3.4f), will need additional information to determine their nature (see §3.3.2). We have examined SEDs of all sources satisfying the criteria ([4.5] – [8.0]) > 0.5 and [8.0] < 14 – ([4.5] – [8.0]). We find that among the 165 sources with 0.5 < ([4.5] – [8.0]) < 2.0, the majority have SEDs similar to AGB stars. In contrast, among the 105 sources with ([4.5] – [8.0]) ≥ 2.0, only two sources show parts of their SEDs resembling that of AGB stars, though the actual number of AGB stars would be larger since some have SEDs indistinguishable from YSOs. Based on our examination of the SEDs, we conclude that ([4.5] – [8.0]) ≥ 2.0 is an satisfactory criterion to statistically exclude most of the bona fide AGB stars from the high-mass YSO population.

After applying the two CMD criteria [8.0] < 14 – ([4.5] – [8.0]) and ([4.5] – [8.0]) ≥ 2.0 to exclude most of the background galaxies and AGB stars, a list of 105 YSO candidates is produced. As an attempt to search for additional candidates that are more embedded and may not be shown as point sources in the 4.5 μm image, similar methods are applied to CMDs of longer wavelength bands, such as [24] vs. ([8.0]–[24]). However, as the angular resolution degrades toward longer wavelengths together with the presence of prominent diffuse dust features, sources without point-like images at 4.5 μm band often show changes in the brightness distribution and shifts in the peak position among images at different IRAC bands, indicating that they are most likely peaks of diffuse dust emission. Therefore, no additional sources are added to the list of YSO candidates.

The 105 YSO candidates selected from the CMD criteria still include unresolved dust clumps, AGB or obscured evolved stars, and background galaxies. Since these contaminants cannot be separated from YSOs with simple color-magnitude relations, a detailed examination on each source is needed to assess its nature. In the next section we discuss how we use SEDs and multi-wavelength images to confirm YSOs.

3.3.2 Multi-wavelength Confirmation and Classification of YSOs

It is not trivial to confirm YSOs in the LMC because the identification of contaminants requires a number of methods. For example, interstellar dust features such as small dust clump or concentration can be identified in high-resolution optical and near-IR images. For background galaxies, some may be resolved in high-resolution images, while other unresolved, distant ones can be identified from their characteristic SED shape, i.e., a nearly flat slope from optical to far-IR observed in active galactic nuclei and quasars (Franceschini et al., 2005; Hatziminaoglou et al., 2005; Rowan-Robinson et al., 2005). For evolved stars with

SEDs resembling massive YSOs, the identification differs from case to case; for example, LI-LMC 957 is away from molecular clouds and shows no diffuse emission in the surroundings of the source at 5.8, 8.0, and 24 μm. A dust-free environment as such is more likely to host an evolved star than a high-mass YSO in isolation. Therefore, to confirm an YSO, simultaneous examination on SED shapes and multi-wavelength images is needed.

We have thus prepared postage stamp images with the same field of view for each YSO candidate in MCELS Hα and MOSAIC $UBVI$, ISPI JK_s, IRAC 3.6, 4.5, 5.8, and 8.0 μm, and MIPS 24 and 70 μm bands. In a few cases when WFPC2 Hα or V images are available, they replace ground-based images; and in other cases when the fields are not covered by our ISPI observations, 2MASS images are used. Next to the stamp images, we also show the source's SED from U to 70 μm, and a [8.0] vs. ([4.5]$-$[8.0]) CMD with the source's location marked. For a source to be confirmed as an YSO, the first step is to establish that the IR excess is circumstellar, not interstellar. We argue that circumstellar emission can be safely assumed for those appearing as point sources in IRAC images and possessing no off-center, discrete dust clumps in optical and near-IR images. The reason is that even if by chance the IR emission comes from a dust clump along the line of sight of an early type star such as O5, the clump has to be small with size < 0.5 pc to appear unresolved in IRAC images, and also within $\lesssim$ 1000 AU, or 0.005 pc from the star to have a dust temperature (assuming albedo = 0) peaking at 8 μm ($\sim$ 360 K). Since an interstellar clump has to be so specifically arranged to mimic the emission from dust in circumstellar disk/envelope, it is most likely that the origin of such IR emission is circumstellar.

We then use SEDs and multi-wavelength images to classify YSOs, guided by SEDs from massive YSO models. Robitaille et al. (2006) proposed a classification scheme, Stage 0, I, II, and III, analogous to the Class scheme for low mass YSOs. We have adopted the same idea but adjusted it to intuitively interpret the observable properties. In our classification for massive YSOs, Class I sources have SEDs rising steeply from near-IR to 24 μm and beyond. Since they are embedded in their circumstellar envelopes within the natal clouds, images of Class I YSOs are unlikely to show counterparts at optical, but will emerge at near-IR (JHK_s) and continuously to brighten up from 3.6 to 70 μm bands[2]. A Class II YSO has a large opening angle in its envelope so emissions from the central source and material inside envelope, such as a disk, dominate the SED, which is characterized with two peaks: one below $\sim$ 1 μm with a lower brightness, and the other between 8 and 24 μm with a rising slope at 1–8 μm. Images of Class II YSOs would show faint counterparts at optical, brighten up from J to 8 μm but drop at 24 μm. Class III YSOs are surrounded by remnant circumstellar material and thus the SEDs show bright, early type stellar emission at optical

---

[2] Although in the 70 μm image the YSOs might not be resolved from companions or surroundings due to the 70 μm array's coarse angular resolution of $\sim 18''$.

and modest dust emission at IRAC bands. Images of Class III YSOs would show bright counterparts at optical with even detectable Hα nebular emission, and become fainter toward long wavelengths at 5.8 and 8.0 μm. This classification describes the observed SEDs of the YSO candidates in N 44 without making a priori assumption of geometry of dust distribution of the YSOs. We will later use the SEDs of our YSOs to examine how well the model predictions match the data.

Three examples of confirmed Class I, II, and III YSOs are shown in Figure 3.5 in images in MCELS Hα, MOSAIC V, ISPI JK_s, IRAC 3.6, 4.5, 5.8, and 8.0 μm, and MIPS 24 and 70 μm, along with their SEDs and marked positions in the [8.0] vs. ([4.5]−[8.0]) CMD. Other than the readily classified cases as those shown in Fig. 4a–c, there are more sources showing complicated nature. The first complication is multiplicity. Seventeen ($\sim$ 30%) of the apparent point sources in IRAC images are resolved into multiple systems or even small clusters in MOSAIC and ISPI images, and another twenty sources show extended images in the ISPI K_s or WFPC2 images, uncertain of their multiplicity. In a multiple system consisted of YSOs and stars, YSOs can be identified through comparisons between J and K_s images (Fig. 4d) because they are bright at Ks but faint at J, while stars show the other way around. However, classification for individual YSOs in a multiple system may be difficult since their emissions at IRAC and MIPS bands are not separable from companions or surrounding ISM. The second complication is dust in the foreground and surroundings ISM. YSOs are often found in dark clouds and dust columns. These interstellar features can be identified in the optical images as dark patches bright-rimmed or against dense stellar background (e.g., Fig. 4f). However, classification for these sources might not always be certain. For example, some sources show non-detection at optical, which can be either a Class I or an obscured Class II, and also have an uncertain origin of the 24 μm emission because the source is not resolved from its surrounding ISM. The last complication is the evolution process of YSOs. As YSOs evolve gradually, the separation between different evolutionary stages is not definite. Several YSOs show characteristics between classes and are assigned as I/II, II/III, etc.

Among the 105 YSO candidates, fifty-nine are confirmed as YSOs and the rejected are twenty-three diffuse dust features, twelve stars in dusty regions, six evolved/AGB stars, and five galaxies. The results of examination on YSO candidates are given in Table 3.3, which lists candidate name, coordinate, 8 μm luminosity order, magnitude in $UBVJHK_s$, 3.6, 4.5, 5.8, 8.0, 24, and 70 μm bands, source type, and remarks on multiplicity and association with dark cloud and dust column. For single source YSOs, their physical properties such as mass and envelope accretion rate can be inferred by comparing their SEDs with model predictions (e.g., Chu et al., 2005). For YSOs in the multiple systems, we did not attempt to derive their properties from comparisons with models since it requires decomposing the SEDs, which needs knowledge on evolutionary stage of individual YSOs and is not available from the current data.

3.4 Determination of YSO Masses

A rough mass range for the central stellar sources in YSOs can be estimated by comparing their locations on the CMD to model predictions (e.g., Whitney et al., 2004a; Robitaille et al., 2006). The faint end of the fifty-nine confirmed YSOs have $[8.0] \sim 11.1 - 11.7$ and $([4.5]-[8.0]) \sim 2.1 - 2.7$, consistent with the brighter end expected from $\sim 4 M_\odot$ models and thus indicating the lower mass limit for the single-source YSOs in our sample. Similarly, $[8.0] \sim 8.0$ is the brightness at which the majority of $\sim 12 M_\odot$ models lie, suggesting that YSOs brighter than this magnitude may have higher masses. These comparisons, however, can only be used as reference points since YSOs of different mass, evolutionary status, and viewing angle overlap greatly in the CMD.

Multi-parameter fits to observed SEDs have been successfully used in previous studies to infer the physical properties of YSOs, such as the mass of the central source (e.g., Chu et al., 2005; Robitaille et al., 2007). We have used the SED Fitting Tool (Robitaille et al., 2007) to derive the physical properties of single-source YSOs in our sample. Figures 3.6–3.8 show the SED fits, with YSOs grouped into Class I, II , and III according to our classification scheme and displayed in the order of their 8 μm luminosities within each group to examine the effect of photometric uncertainties on the fits. The number of models that fit the data and the χ^2 value of the best-fit model are given in Table 3.4, along with selected physical properties inferred from the models, including foreground extinction; mass, temperature, and age of the central stellar source; envelope accretion rate; disk accretion rate and mass; and total luminosity. In the following paragraphs we discuss the results of fits for each class.

In the seven Class I YSOs used in the fitting (Fig. 3.6), the best-fit SEDs match well with observations. Only in the two faintest YSOs are the fits not well constrained due to an insufficient number of data points in the SED. The inferred foreground extinctions, $A_V = 2.4 - 26.9$, are consistent with observed environments of the seven Class I YSOs, five of which are in dark clouds. This agreement indicates that the integrated physical properties derived from the fits are representative of the YSOs. The inferred young ages of the central sources, $1.0 \times 10^4 - 2.8 \times 10^5$ yr, and the high envelope accretion rates, $1.2 \times 10^{-4} - 7.0 \times 10^{-3} M_\odot$ yr^{-1}, suggest that they are in the main accretion phase and embedded in massive envelopes, consistent with that expected in our empirical classification for Class I sources. The masses estimated for the central stellar sources range from ~ 12 to $25 M_\odot$, corresponding to ~ B2–O8/9 (Schmidt-Kaler, 1982).

In the twelve Class II YSOs used in the fitting (Fig. 3.7), the best-fit SEDs show reasonable agreement with observations, although the deviations are larger compared to those of the Class I YSOs. The most common deviation is PAH emission. Characterized by a "check-mark" SED shape at four IRAC bands, PAH emission is observed in most of our Class II YSOs. As the model calculations do not include PAH emission, the fitting tends to result in a highly edge-on viewing angle or an over-estimate of the disk mass to account for the emission. This fitting error might also be responsible for deviations observed at near-IR (JHK_s) and/or optical ($UBVI$) bands in several YSOs. Despite the deviation, the overall good agreement between models and observations indicates that the derived physical properties are likely still acceptable. Compared to Class I sources, these YSOs have inferred ages about ten times higher but envelope accretion rates at least two orders of magnitudes smaller or completely negligible. The older ages and smaller envelope accretion rates indicate that these YSOs are more evolved and less embedded, consistent with our empirical classification of Class II sources. The masses estimated for the central sources range from $\sim$ 8 to $19M_{\odot}$, corresponding to $\sim$ B3–B0.

In the eight Class III YSOs used in the fitting (Fig. 3.8), only four of them have best-fit SEDs in reasonable agreement with the observations. In sources 052207.3−675819.9, 052229.1−675359.5, and 052126.2−674742.1, model SEDs deviations are observed in the IRAC bands, which is likely due to PAH emission. In source 052340.6−680528.5, the model SED deviates at optical and near-IR bands, but the origin of this deviation is not obvious. The inferred physical properties show that three of these four Class III YSOs not only have a zero envelope accretion rate, but also their disk accretion rate and mass are respectively 10^5 and 10^{3-4} times smaller than those of Class II sources, consistent with that expected for Class III sources. The other YSO, source 052207.3−675819.9, has inferred envelope and disk properties comparable to those of Class II YSOs. These values, however, may not be reflective of reality since the radiative transfer in the models only takes into account dust emission, but this YSO has already formed a small H II region (see detail in §3.6.1) and its warm, ionized gas also contributes to the total emission. Nevertheless, this inconsistency does not significantly affect its stellar mass estimate. The masses estimated for the stellar sources in these four YSOs are $\sim 9 - 11M_{\odot}$, corresponding to B3–B2.

The other four Class III sources have major discrepancies between the best-fit and observed SEDs. All four YSOs show an IR deficit at 1–6 μm in their SEDs compared to the best-fit models. This discrepancy is unlikely to come from bad fits to the viewing angle, as we have examined the same model with all ten available viewing angles for each YSO and found none of them can reproduce the observed SED satisfactorily. We note that similar discrepancies using the same models were also found for the low-mass YSOs DM Tau and GM Aur (Robitaille et al., 2007). These two YSOs are known to have a near-IR deficit in their SEDs, which was interpreted as a clearing of the dust from the inner regions of their disks (Rice et al., 2003; Calvet et al., 2005). It is possible that our high-mass YSOs also experience a similar disk evolution phase. We also note that the SEDs of some Herbig Ae/Be stars in Hillenbrand et al. (1992) exhibits overall shapes similar to those of these Class III YSOs. Sources 052147.1−675656.7, 052315.1−680017.0, and 052157.0−675700.1 resemble the Herbig Be star FMC 27 in the Galactic H II region RCW 34 (Finkenzeller & Mundt, 1984; Rodgers et al., 1960), while 052159.6−675721.7 and one of the better-fitted Class III sources, 052340.6−680528.5, resemble the Herbig Ae star TY Cra. FMC 27 and TY Cra were suggested to be stars or star/disk systems viewed through a remnant infalling envelope (Hillenbrand et al., 1992); our YSOs could also be in a similar situation.

Comparisons between model and observed SEDs for selected YSOs show that models reproduce observations well for Class I sources, begin to deviate from observations for Class II sources mainly due to the lack of PAH emission in calculations, and can exhibit large differences from Class III sources. In general, our empirical classification agrees with the evolutionary stages expected from high-mass YSO models. The masses of the central sources estimated for these YSOs range from ~ 8 to 25 $M_{\odot}$, corresponding to B3–O8. Note that this is not the total mass range for YSOs in our sample since only the single-source YSOs are included in the fitting; faint sources in multiple systems would have even lower masses. Finally, it is interesting that while the majority of the Class I sources do not have PAH emission, most of the Class II and some Class III sources show PAH emission. This emission might originate from the circumstellar disks around the YSOs, like that observed in the disks around Ae stars (e.g., Ressler & Barsony, 2003; van Boekel et al., 2004). However, the emission is not necessarily confined to the disks but can originate anywhere the UV radiation from the central sources reach. Our current broad-band SEDs are not adequate to distinguish between these two origins, but comparisons between IR spectroscopic observations and model predictions (Li & Draine, 2001, 2002; van Boekel et al., 2004) might shed light on the origin of the emission.

3.5 Spatial Distribution of Star Formation

The large number of massive YSOs found in N 44 provides an excellent opportunity for us to investigate questions such as 1) whether different interstellar conditions lead to star formation with different mass function, 2) how star formation proceed across the region, and 3) whether there is evidence of triggered star formation.

3.5.1 YSOs in H II Regions

In N 44, about 40% of the YSO candidates are found inside or near the edges of bright H II regions. Such configuration can result from either triggering or spontaneous star formation. In the former case, the ionization front of an H II region can compress pre-existing molecular clumps and trigger star formation, or the swept-up material at the interface between the ionization front and molecular cloud can accumulates into a dense ridge and becomes gravitationally unstable and then fragments and collapses to form stars (Elmegreen, 1998). Alternatively, the star formation may not occur coevally. Some massive stars may form first and photonionize the surrounding clouds to expose other nearby YSOs or even cause an early disruption of their accretion processes. The YSOs in and around H II regions offer a close view of both triggering and disrupting influences from massive stars. Since the examination requires high angular resolution images of ionized/shocked gas around the YSOs, only those with *HST* observations will be included in the discussion. WFPC2 images of three H II regions, N 44C, N 44F, and N 44H, are available in the *HST* archives and they have YSOs within the field. In the following the fields are discussed individually.

N 44C is a bright H II region situated at southwest of the superbubble shell rim. The main ionization source is an O7 V star (Oey & Massey, 1995) as marked in the WFPC2 Hα image in Figure 3.9a. In the field also marked are seven YSO candidates. The spatial relation between YSOs and the ionized gas is better illustrated in a color composite of the same field displayed in Fig. 3.9b where 8 μm, K_s, and Hα images are mapped in red, green, and blue, respectively. Two of the YSOs are projected within N 44C. There is no morphological feature in the Hα emission to indicate a causal relationship between the H II region and the YSOs. The remaining five YSOs in N 44C are located away from the boundary of the H II region. They are randomly distributed within the optically obscured region which coincides with the location of a molecular cloud (Chin et al., 1997; Fukui et al., 2001). The spatial distribution of the YSOs with respect to the H II region together with the high mass of the molecular cloud ($3.7 \times 10^5 M_\odot$, Mizuno et al., 2001) make it unlikely for the H II region to be responsible for the formation of these YSOs. Nevertheless, as will be discussed in §3.5.3, their formation might have been triggered by the expansion of the superbubble.

Projected near N 44C, a small H II region is detected around YSO 052207.3−675819.9. Figure 3.10 shows a close-up of this H II region in the Hα emission-line and R continuum images. The size of the H II region is $2''\!.2 \times 1''\!.5$, or 0.53pc×0.36pc. The H II region has an average surface brightness[3] of 1.9×10^{-14} ergs cm^{-2} s^{-1} arcsec^{-2}, corresponding to an emission measure of 9.4×10^3 cm^{-6} pc. Assuming that the line-of-sight length of the H II region is the average of the two axes, 0.45 pc, the rms electron density is then ~ 145 cm^{-3}. The size of the H II region is comparable to those of compact H II regions, i.e., $\lesssim 0.5$ pc, but its rms electron density and emission measure are much smaller than the canonical values of compact H II regions, i.e., $\gtrsim 5 \times 10^3$ cm^{-3} and $\gtrsim 10^7$ cm^{-6} pc (Franco et al., 2000). The mass of the central source can be estimated from its location in the extinction-free W vs. Q CMD (Chapter 2). The star has extinction free color $Q = -0.76 \pm 0.02$ and magnitude $W = -0.96 \pm 0.03$, consistent with a 7–10 $M_\odot$ MS star (Lejeune & Schaerer, 2001), or a B2–3 MS star. We further estimate the required ionizing power from

---

[3] Owing to the ~ 300 km s^{-1} redshift of the LMC, the filter transmission of the red-shifted Hα line is $\sim 93\%$ of the peak transmission, thus the extracted Hα surface brightness and flux are multiplied by a correction factor of 1.07.

the Hα luminosity of the H II region. To determine the Hα luminosity, the Hα flux is extracted using an aperture of its size, resulting in an Hα flux of 5.0×10^{-14} ers cm^{-2} s^{-1}. The extinction is estimated from the difference between the observed color $(B-V) = 0.20$ and the expected intrinsic color $(B-V)_0 = -0.22$, resulting in the observed/intrinsic Hα flux ratio of 2.47 (Peimbert & Torres-Peimbert, 1974). Given the Hα flux, a distance of 50 kpc, and an extinction correction factor of 2.47, the Hα luminosity of the H II region is 3.7×10^{34} ergs s^{-1}. Assuming a 10^4 K optically thick H II region, the required ionizing luminosity, $Q(\mathrm{H}^0)$, can be derived from the Hα luminosity, $L_{\mathrm{H}\alpha}$, through the relation $Q(\mathrm{H}^0) = 7.4 \times 10^{11}\ L_{\mathrm{H}\alpha}$ photons s^{-1}. The required ionizing luminosity of the H II region is 2.7×10^{46} photons s^{-1}. This value is smaller than that of a B0.5V star, 5.9×10^{47} photons s^{-1} (Schaerer & de Koter, 1997). As a B0.5V star has a mass $< 19M_\odot$, the ionization requirement is consistent with the mass estimated from our *UBV* photometry.

N 44F is a bright, classical ring-nebula H II region at the northwest rim of the superbubble. Its ionizing flux comes mainly from an O8III star (Will et al., 1997) as marked in Figure 3.11a. Two prominent pillar-like dust columns can be readily recognized in the WFPC2 Hα image (Figure 3.11a), but only one YSO is found in the field. This YSO is emerging at the tip of a dust column, similar to those in the Eagle Nebula (=M 16, Hester et al., 1996). The mass estimated from the SED fit for the YSO is $\sim 10M_\odot$. Compared to those seen in the Eagle Nebula, $\sim 3-4M_\odot$ (Thompson et al., 2002), our YSO is more massive.

N 44H is located to the southeast of the superbubble. The H II region is ionized by four early B stars (Chapter 2), one of them is B0-1 and the other three is B2-3, as marked in Figure 3.12a. There is no morphological feature in the Hα emission to indicate a causal relationship between the H II region and the YSO. However, as the YSO is projected against the outflow of the hot (10^6 K) gas, the hot gas might have triggered the star formation.

3.5.2 Global Distribution of YSOs

With the large number of YSOs detected in N 44, we can investigate what caused current star formation, examine whether star formation depends on initial conditions, and further assess how star formation proceeds across the region. To answer these questions, we need to examine the relationships between YSOs and the interstellar environment.

We first compare the spatial distribution of YSOs to those of ionized gas and molecular cloud. Ionized gas delineates regions where massive stars were formed in the last few Myr and their energy feedback might have triggered the next generation of star formation. Molecular clouds are potential sites for star formation. Figure 3.13b plots the YSO locations and CO contours over an Hα image of N 44. Clearly, the great majority of the YSOs are found in molecular clouds, and they concentrated toward the three molecular peaks.

A closer examination shows that the central molecular peak has the highest concentration of YSOs; it contains nineteen YSOs ($\sim 1/3$ of the total YSOs) in an area of $4' \times 2'$. The bright Hα emission indicates that it has intense star formation in the past few Myr. The northern molecular peak has loosely distributed YSOs and its concentration level of molecular material is the lowest among the three. The YSOs are not associated with large ionized gas structures, indicating that they are the first generation of massive stars formed in that cloud. The southern molecular peak has two concentrations of molecular gas, and these two concentrations show different types of star formation. The concentration toward northeast has more distributed YSOs and lower surface-brightness H II regions, while the other concentration has four YSOs packed between the CO contour peak and the boundaries of the bright H II region. Apparently, star formation properties are different in these clouds.

To understand what might caused different star formation in these clouds, we have further compared their physical properties. The three clouds have different velocity dispersions (Mizuno et al., 2001). The northern molecular peak LMC/M5221-6750, which shows the least advanced star formation, has a smaller FWHM line-width, $\Delta V = 3.8$ km s^{-1}, at the peak position. The central molecular peak LMC/M5221-6802 and the southern molecular peak LMC/M5239-6802 have $\Delta V = 7.2$ and 15.8 km s^{-1}, respectively. The larger line-width in the clouds with more advanced star formation may come from the energy feedback from massive stars. The central molecular peak, being adjacent to the superbubble, is likely to be energized by the expansion of the superbubble. The southern molecular peak may have energy input from the expansion of the H II region, or the pressure from the outflow of the hot gas (Fig. 3.13c).

3.5.3 Triggered Star Formation

Using YSOs and their interstellar environment, we can investigate whether some of the current star formation in N 44 is triggered. The YSOs in the central molecular peak are potential cases of triggered star formation, as the triggering mechanism, i.e., expansion of the superbubble, is present. The distribution of the molecular peak is centered at the shell rim, which may be interpreted as the molecular peak is pushed by the expansion of the superbubble. However, as it is also possible to interpret the molecular distribution as the superbubble expands outwardly from the molecular peak, other argument is needed to strengthen or weaken the case. Comparisons among the distributions of YSOs in the three molecular peaks show that the YSOs in the central peak are distributed in a specific pattern, i.e., along the superbubble rim, while the other molecular peaks show a more scattered pattern around the CO contour peak. This resemblance in the distribution of YSOs and the rim structure indicates that the triggering from the expansion of the superbubble must have played an important role in the current star formation in this cloud.

The three molecular peaks show different advancement of star formation, with the central molecular peak being the most advanced and the northern molecular peak being the least advanced. To examine how star formation proceeded across this region, we have first compared the systematic velocities of the three molecular peaks. The northern, central, and southern molecular peaks have V_{LSR} = 283.8, 282.5, and 279.5 km s^{-1}, respectively (Mizuno et al., 2001). These three values are close and thus it is possible that the three clouds are physically close to one another. A comparison between distributions of CO contours and X-ray contours (Fig. 3.13b-c) shows that the outflow of hot gas from the superbubble appears to extend into the south molecular peak. Along the outflow path, two YSOs are found in the southern molecular peak. This spatial arrangement suggests the interaction between the hot gas and the south molecular peak. Therefore, these two YSOs are likely to be triggered. Since the central molecular peak and southern molecular peak interact, it is possible that star formation proceeded from the central to southern molecular peak. There is no morphological feature in X-ray contours or H I map (Fig. 3.13c-d) to indicate that the central and north molecular peaks are related. Therefore, the two molecular peaks are likely to be independent from each other.

3.6 Figures and Tables

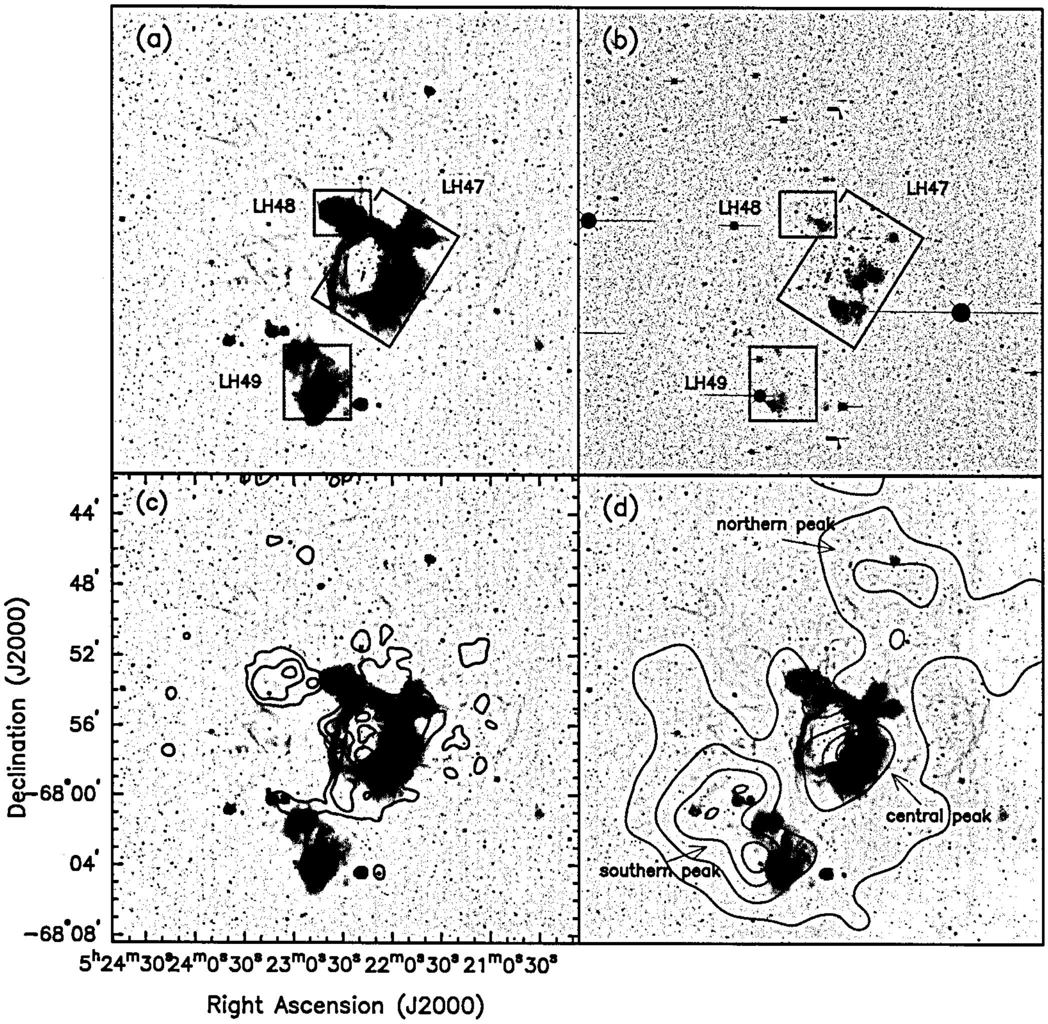

Figure 3.1 MCELS Hα and MOSAIC B-band images of N 44. (a) OB associations LH47/48/49 labeled on MCELS Hα image, (b) OB associations LH47/48/49 labeled on MOSAIC B image, (c) X-ray contours (Chu et al., 1993) over Hα image, and (d) CO contours (Fukui et al., 2001) over Hα image.

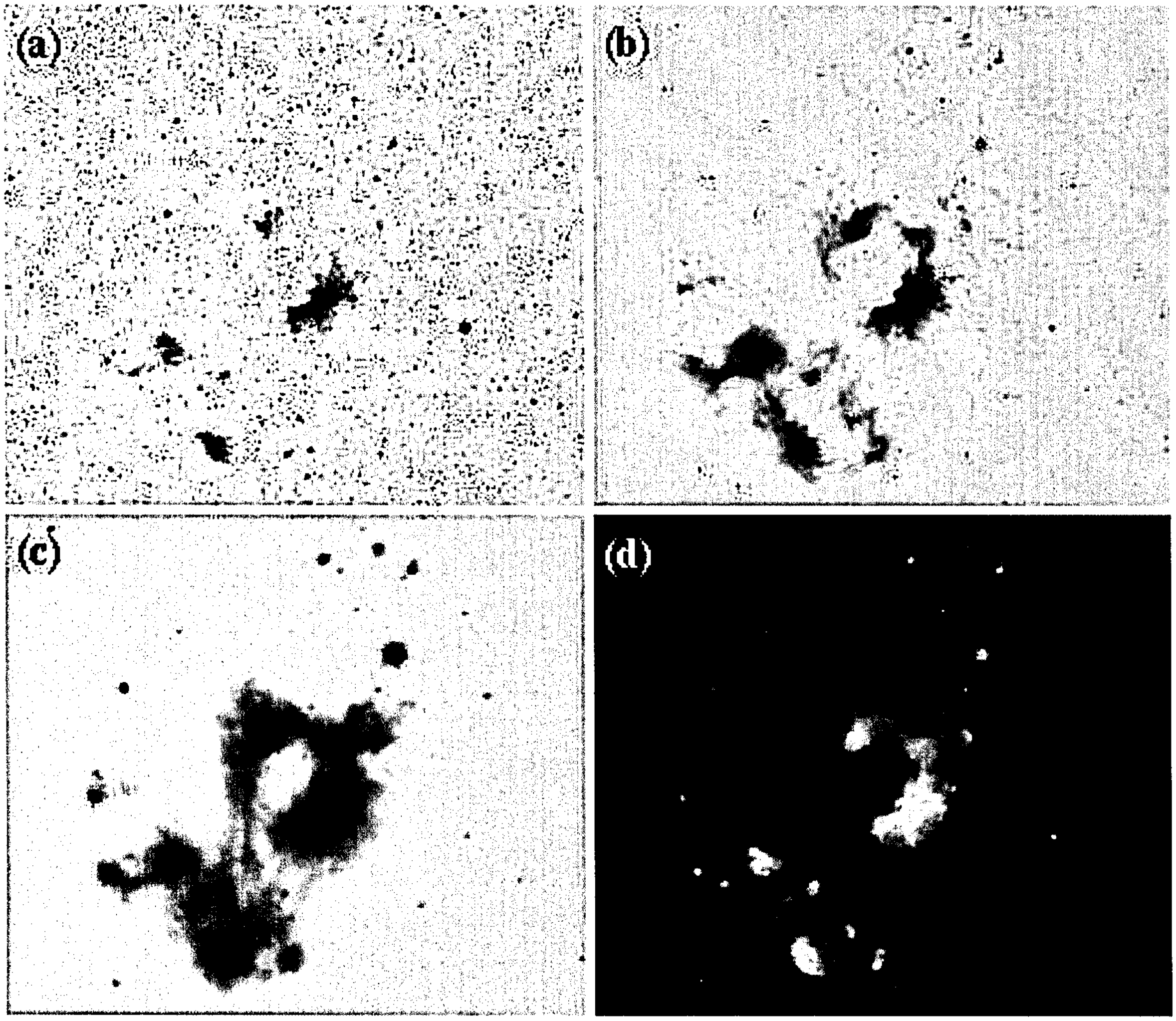

Figure 3.2 IRAC and MIPS images of N 44. (a) 3.6 μm image showing stars and modest PAH emission, (b) 8.0 μm image showing PAH & dust emissions, (c) 24 μm image showing dust emission, and (d) color composite of 3.6, 8.0, and 24 μm images. Dust shrouded objects, e.g., YSOs and AGB stars, appear red.

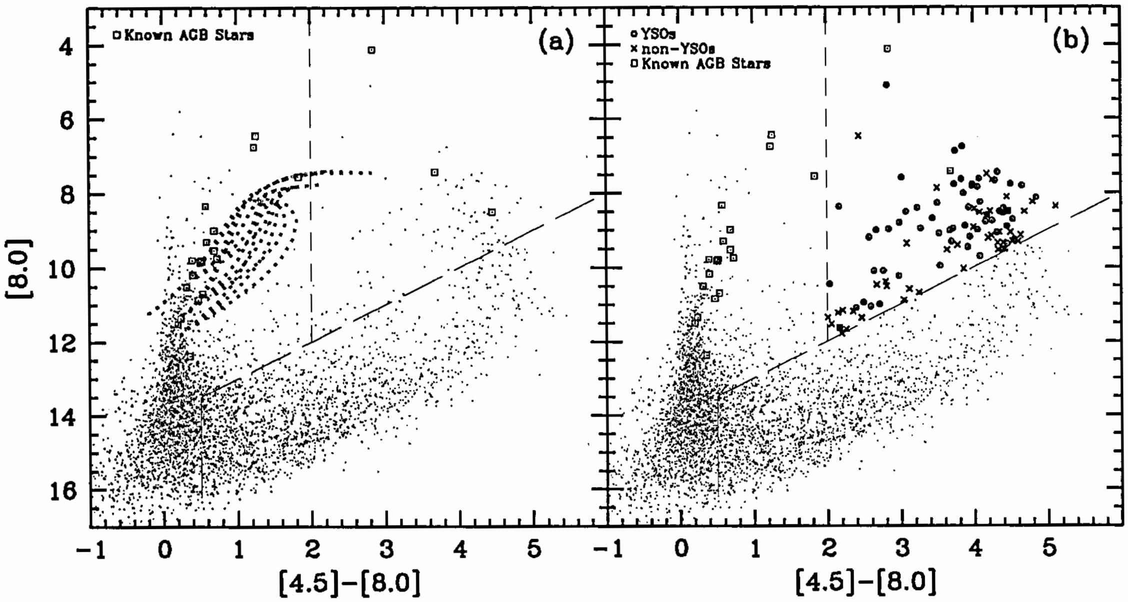

Figure 3.3 CMDs of sources detected in N 44. YSOs lie in the right part of the diagram. (a) Known AGB stars are marked with additional open cyan boxes and predictions from AGB stellar models (Groenewegen, 2006) are shown in filled yellow boxes. The upper right wedge has the minimum contamination from stars and background galaxies. The long and short dashed lines show the color-magnitude cut that defines the criteria for selecting YSO candidates. (b) Confirmed YSOs are marked with additional open red circles and non-YSOs with green crosses.

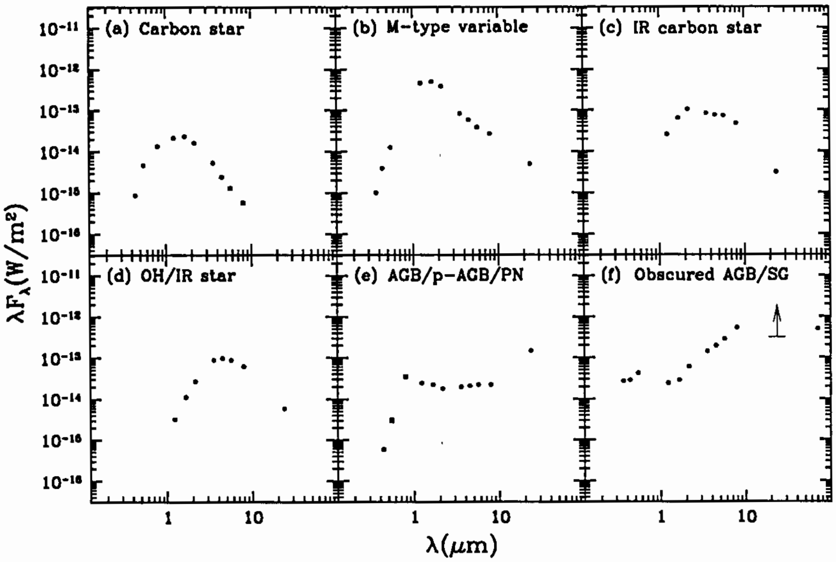

Figure 3.4 Example SEDs of known AGB and obscured SG stars within the field of N 44. (a) Carbon star LMC-BM 24-8 (Blanco & McCarthy, 1990), (b) M-type variable GRV 0523−6752 (Reid et al., 1988), (c) IR carbon star MSX LMC 511 (Egan et al., 2001), (d) OH/IR star MSX LMC 516 (Egan et al., 2001), (e) AGB/post-AGB/PN candidate IRAS 05240−6809 (= LI-LMC 948, Loup et al., 1997), and (f) obscured AGB/SG star IRAS 05216−6753 (= LI-LMC 861, Wood et al., 1992).

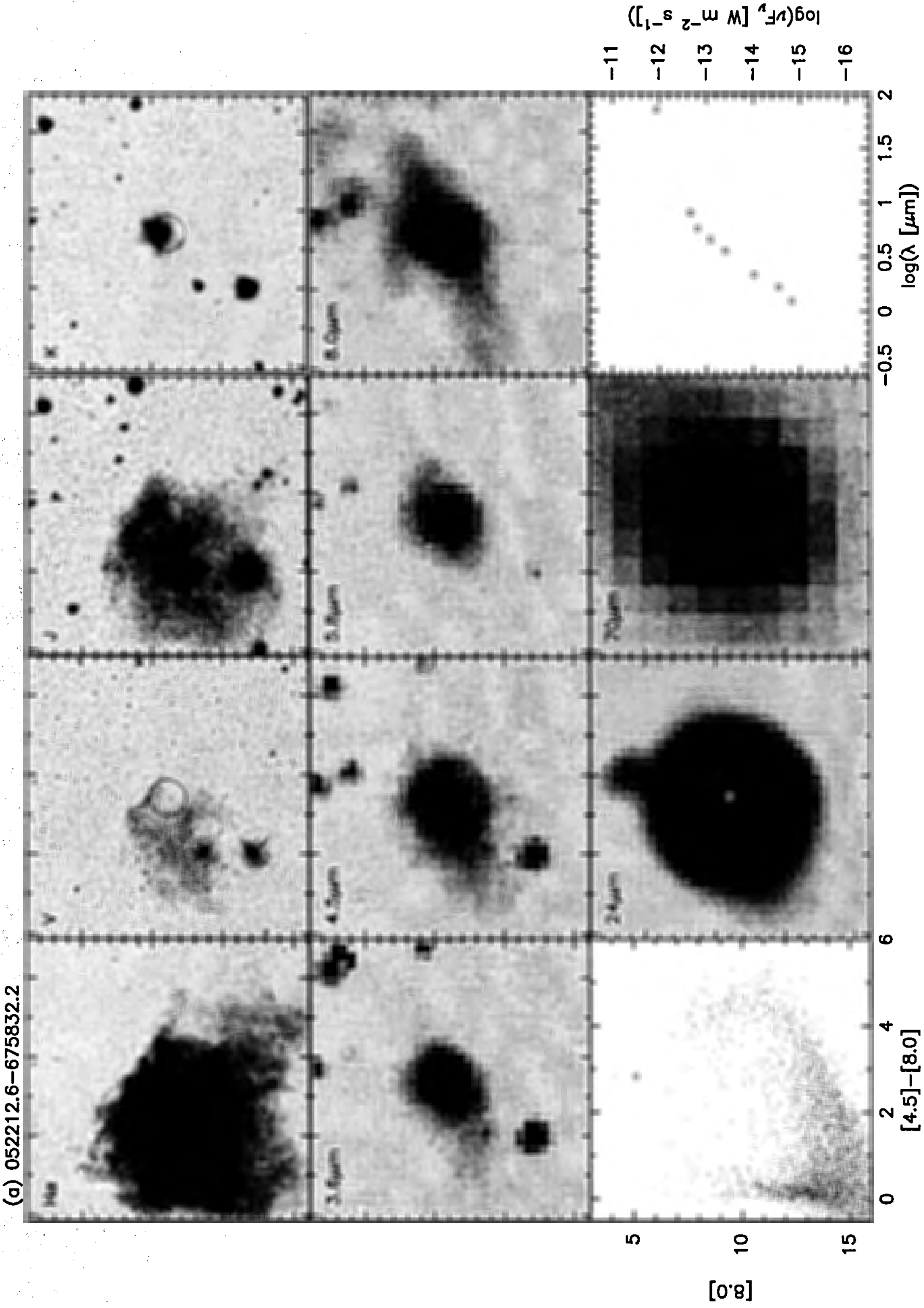

Figure 3.5 Multi-wavelength images, CMD, and SED of example YSOs in N 44. (a) Single-source Class I YSO, (b) single-source Class II YSO, (c) single-source Class III YSO, (d) YSO in a multiple system, and (e) YSO at the peak of a dust pillar.

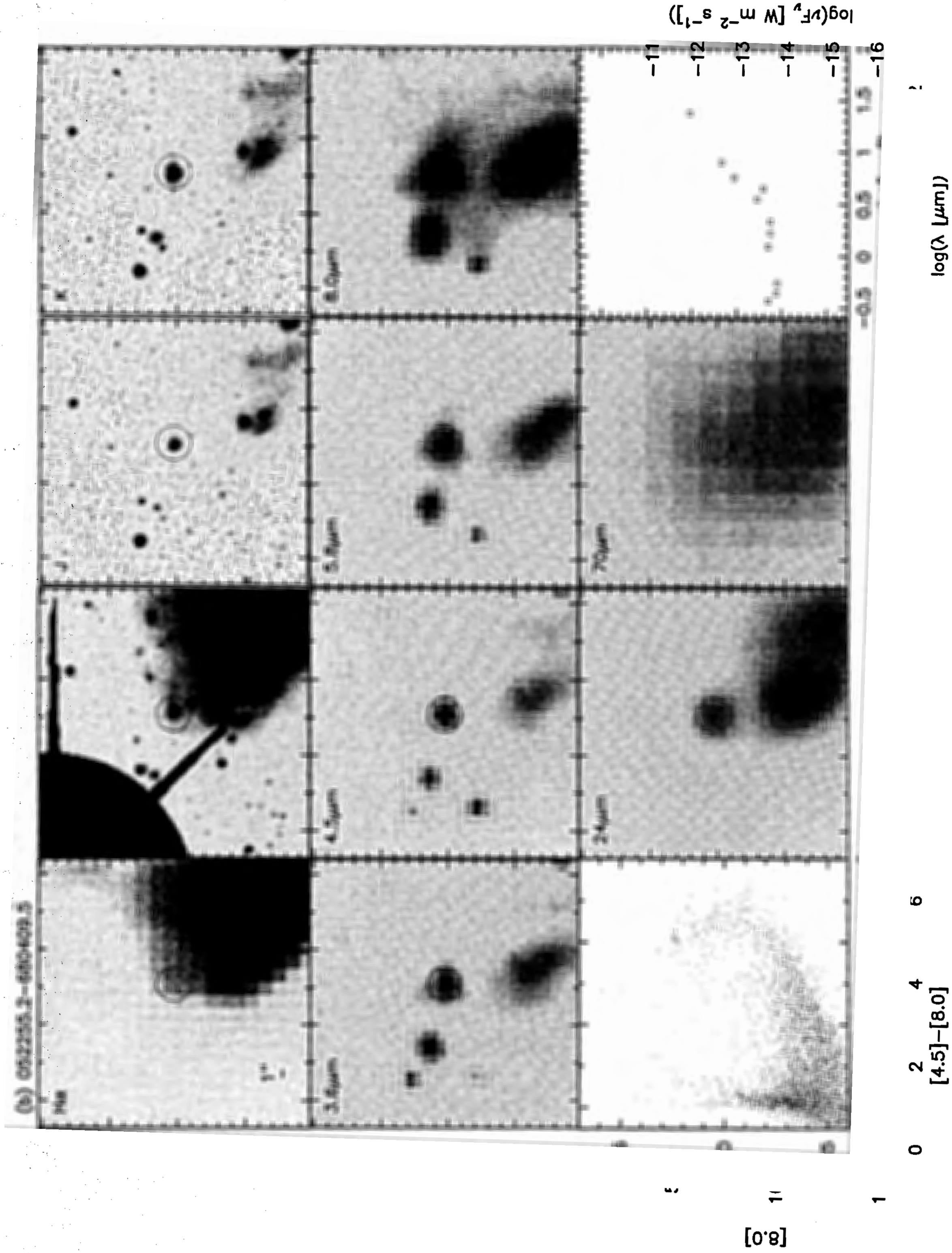

Fig. 3.5 — Continued.

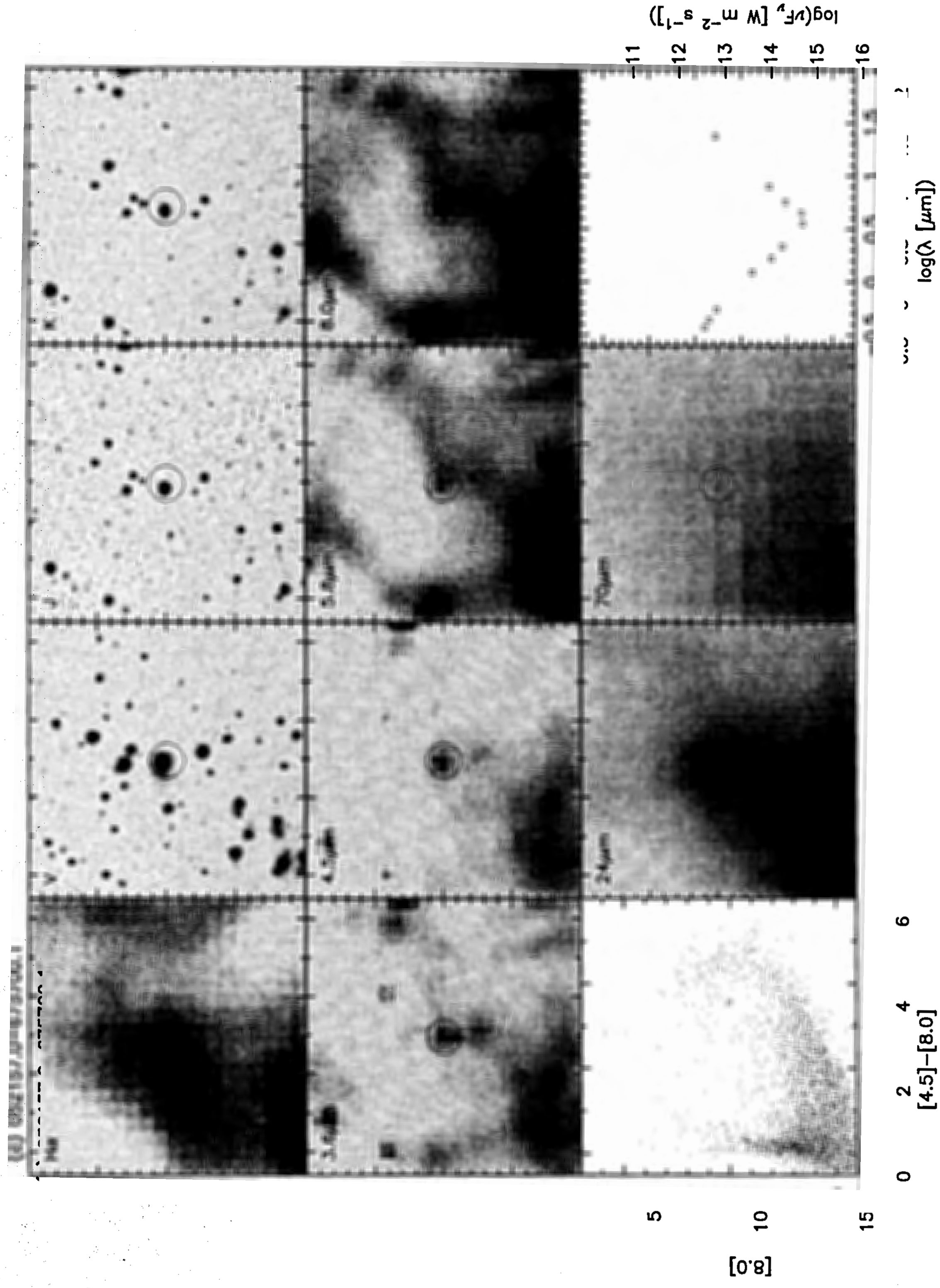

Fig. 3.5 — Continued.

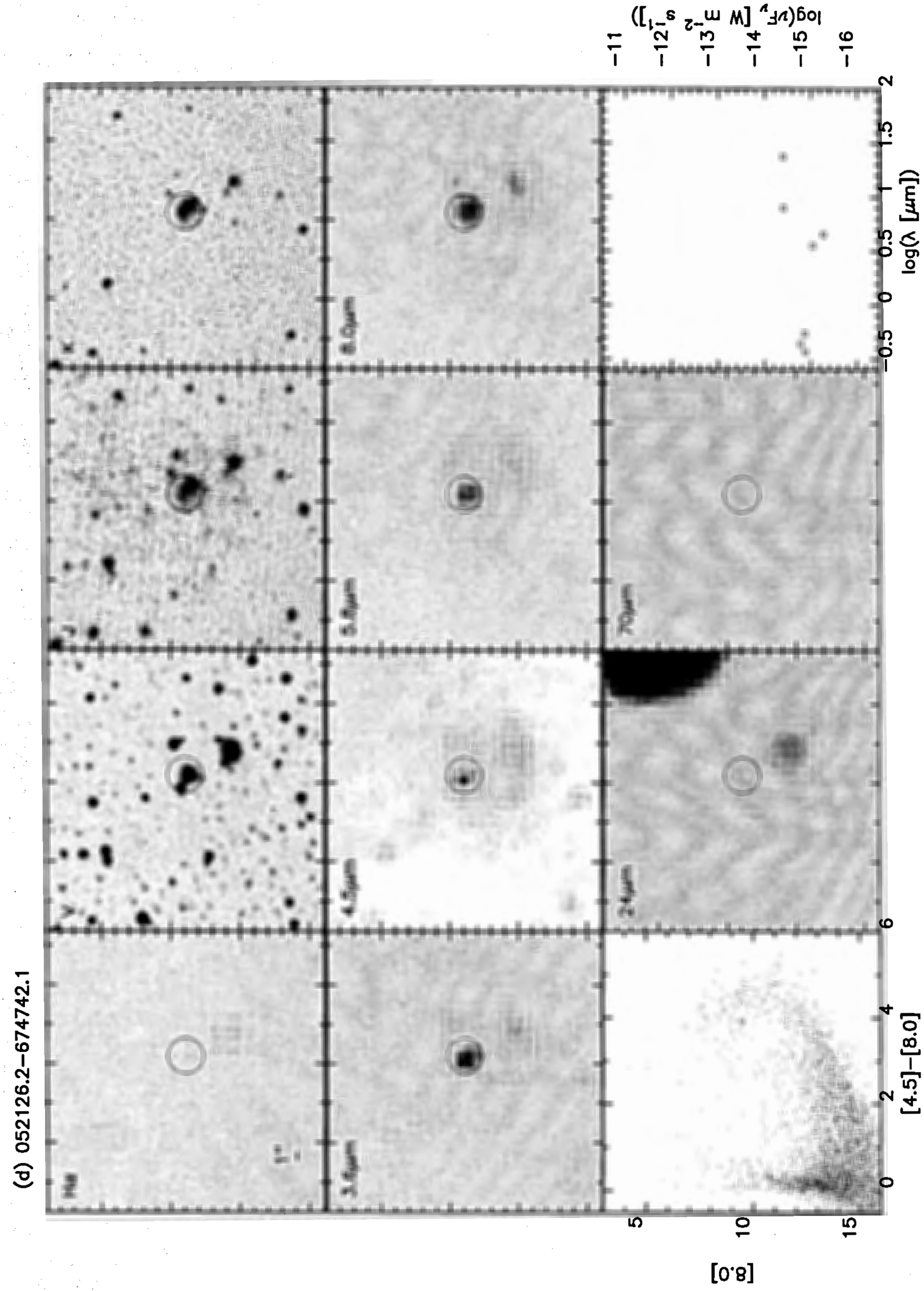

Fig. 3.5 — Continued.

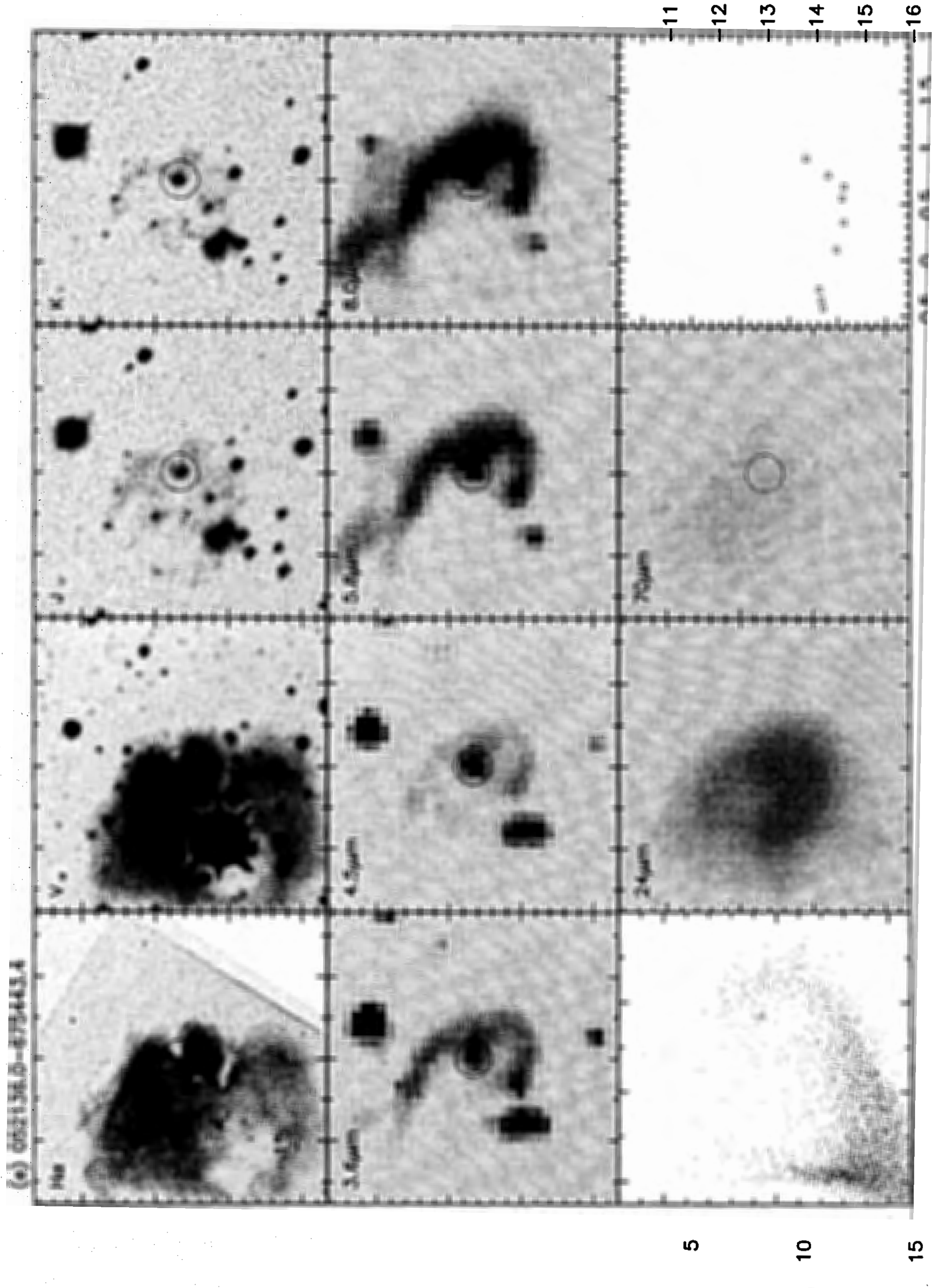

Fig. 3.5 — Continued.

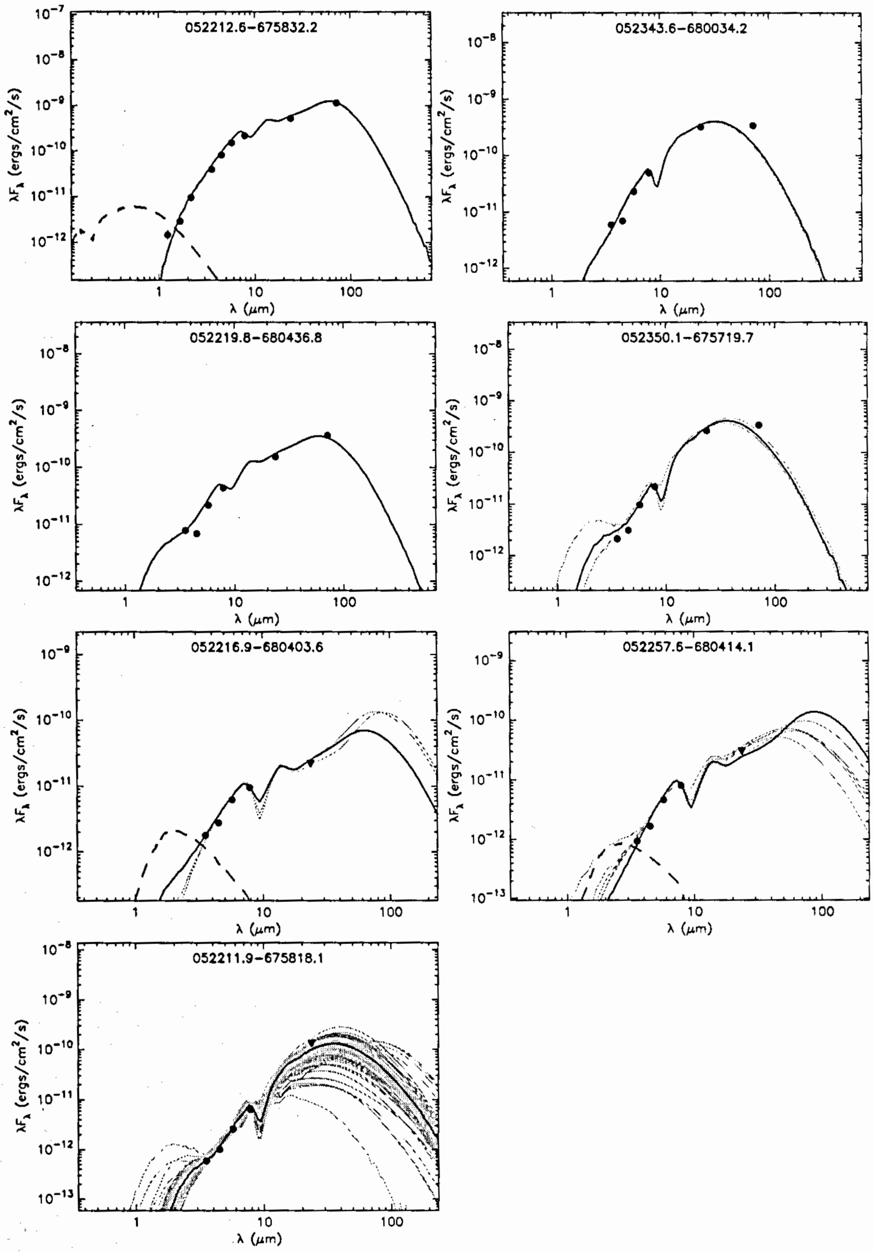

Figure 3.6 SEDs of seven Class I and I/II YSOs analyzed in the paper. Filled circles are the flux values converted from magnitudes listed in Table 3.3. Triangles are upper limits. Error bars are shown if larger than the data points. The solid black line indicates the best-fit model, and the gray lines show all models that also fit the data similarly well (defined by $\chi^2 - \chi^2_{\rm best} < 3$ per datapoint). The dashed line shows the stellar photosphere model that was used as input to the radiation transfer code for the best-fit model, with the best-fit interstellar extinction taken into account.

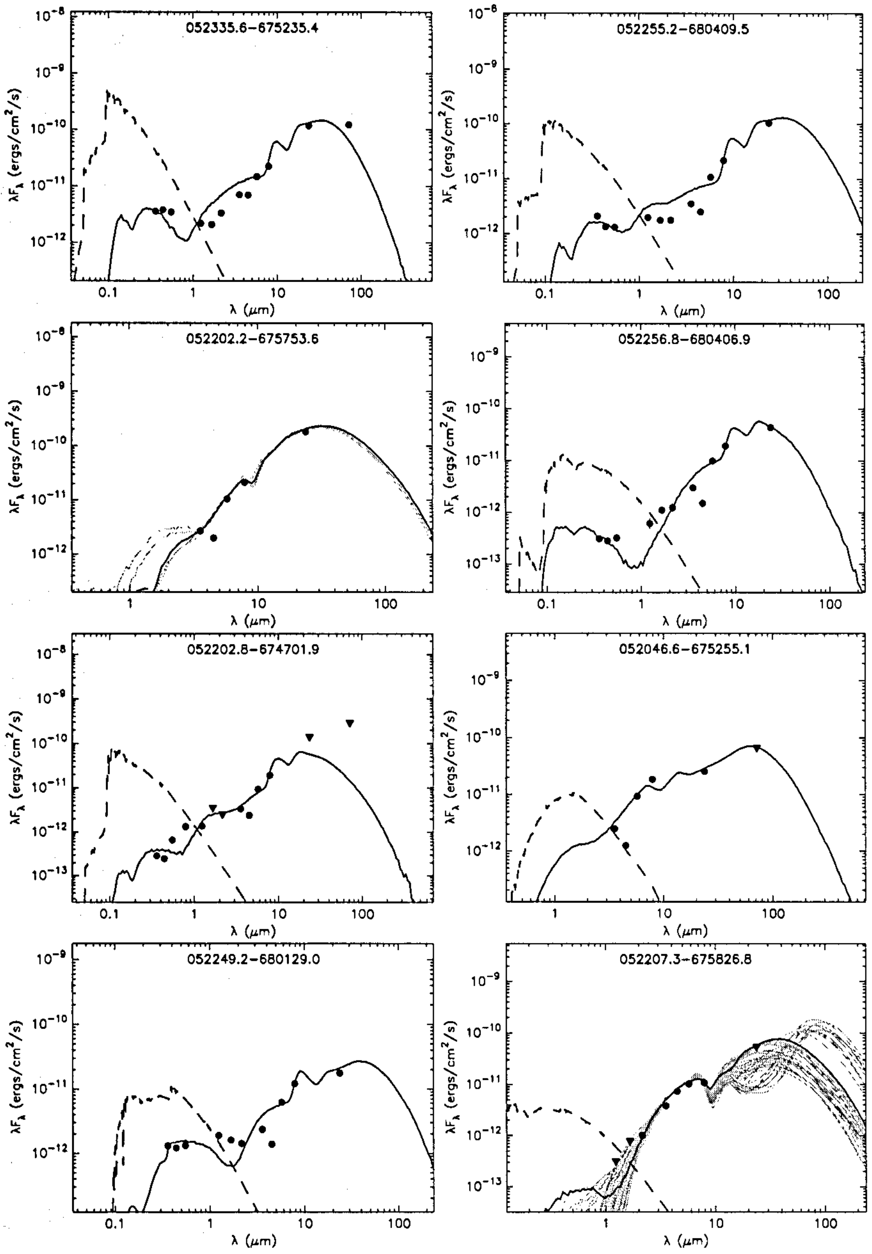

Figure 3.7 SEDs of twelve Class II and II/III YSOs analyzed in the paper. Symbols are the same as Fig. 3.6.

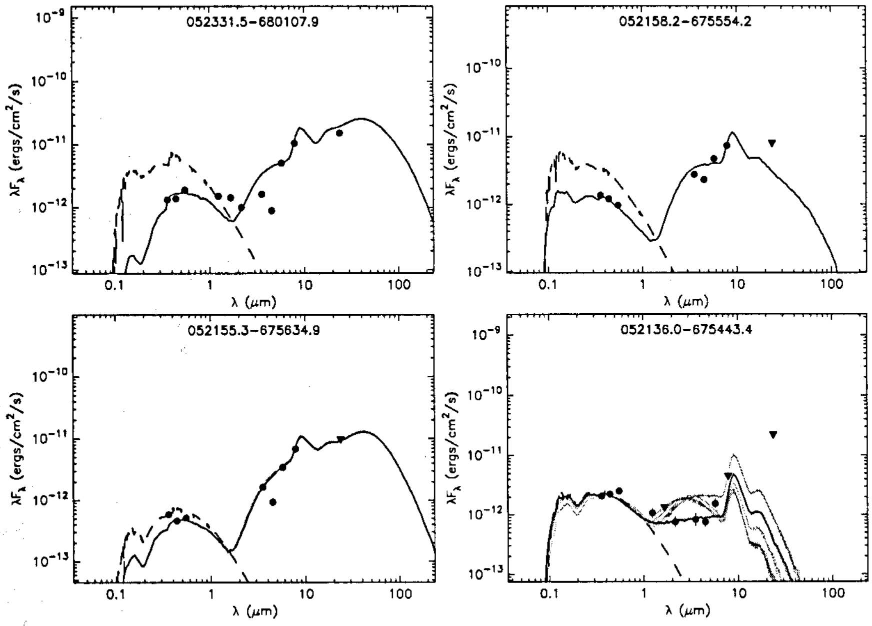

Fig. 3.7 — Continued.

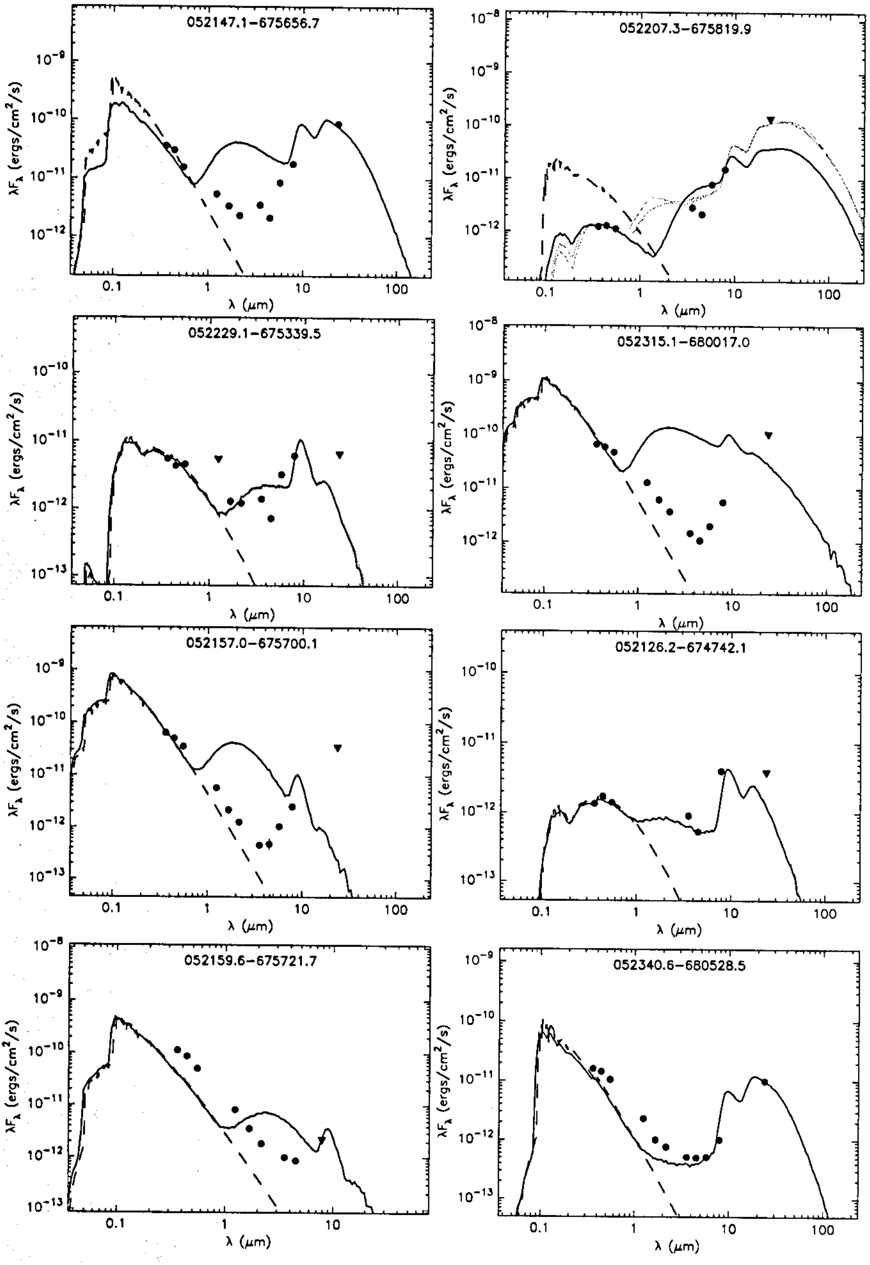

Figure 3.8 SEDs of eight Class III YSOs analyzed in the paper. Symbols are the same as Fig. 3.6.

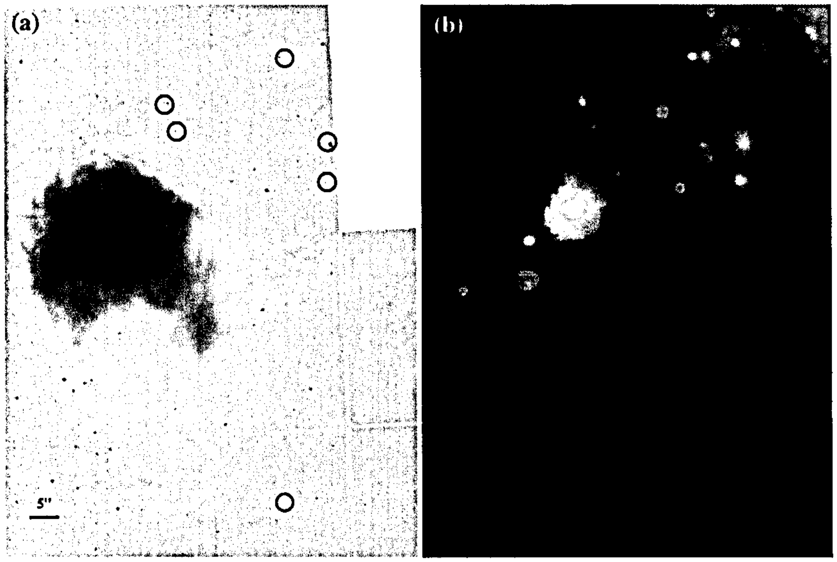

Figure 3.9 YSOs in the H II region N 44C. (a) Positions of YSOs (red) and ionizing stars (cyan) marked on WFPC2 Hα image of N 44C. (b) Color composite with 8 μm, K_s, and Hα images mapped in red, green, and blue.

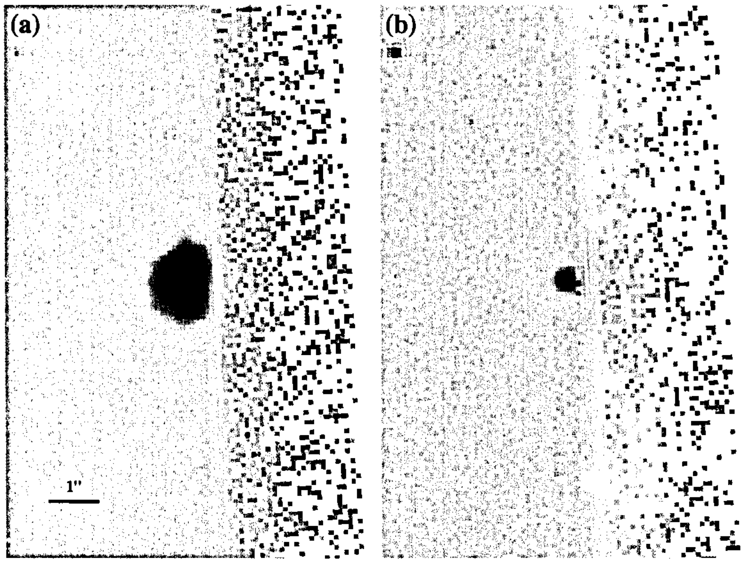

Figure 3.10 Close-up WFPC2 images of the small H II region associated with YSO 052207.3−675819.9 projected within N 44C. The H II region is shown in (a) Hα and (b) R images.

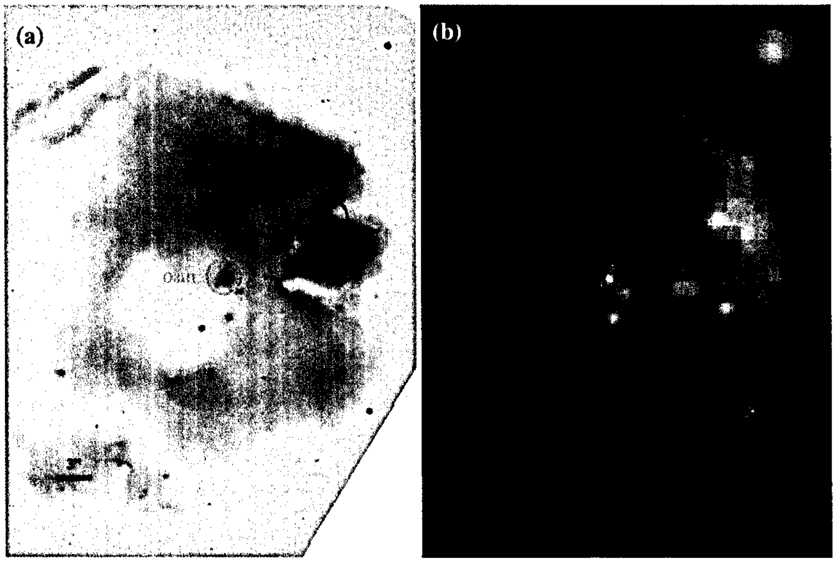

Figure 3.11 YSOs in the H II region N 44F. (a) Positions of YSOs (red) and ionizing stars (cyan) marked on WFPC2 Hα image of N 44F. (b) Color composite with 8 μm, K_s, and Hα images mapped in red, green, and blue.

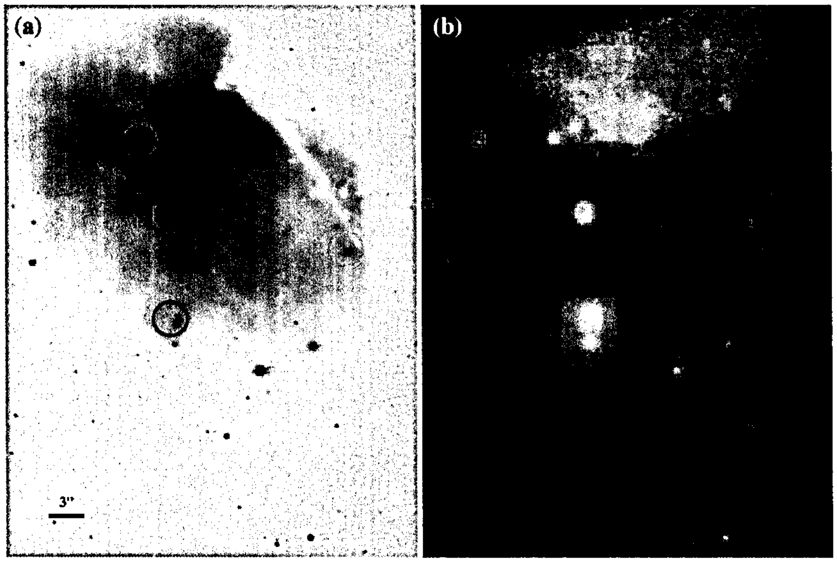

Figure 3.12 YSOs in the H II region N 44H. (a) Positions of YSOs (red) and ionizing stars (cyan) marked on WFPC2 Hα image of N 44H. (b) Color composite with 8 μm, K_s, and Hα images mapped in red, green, and blue.

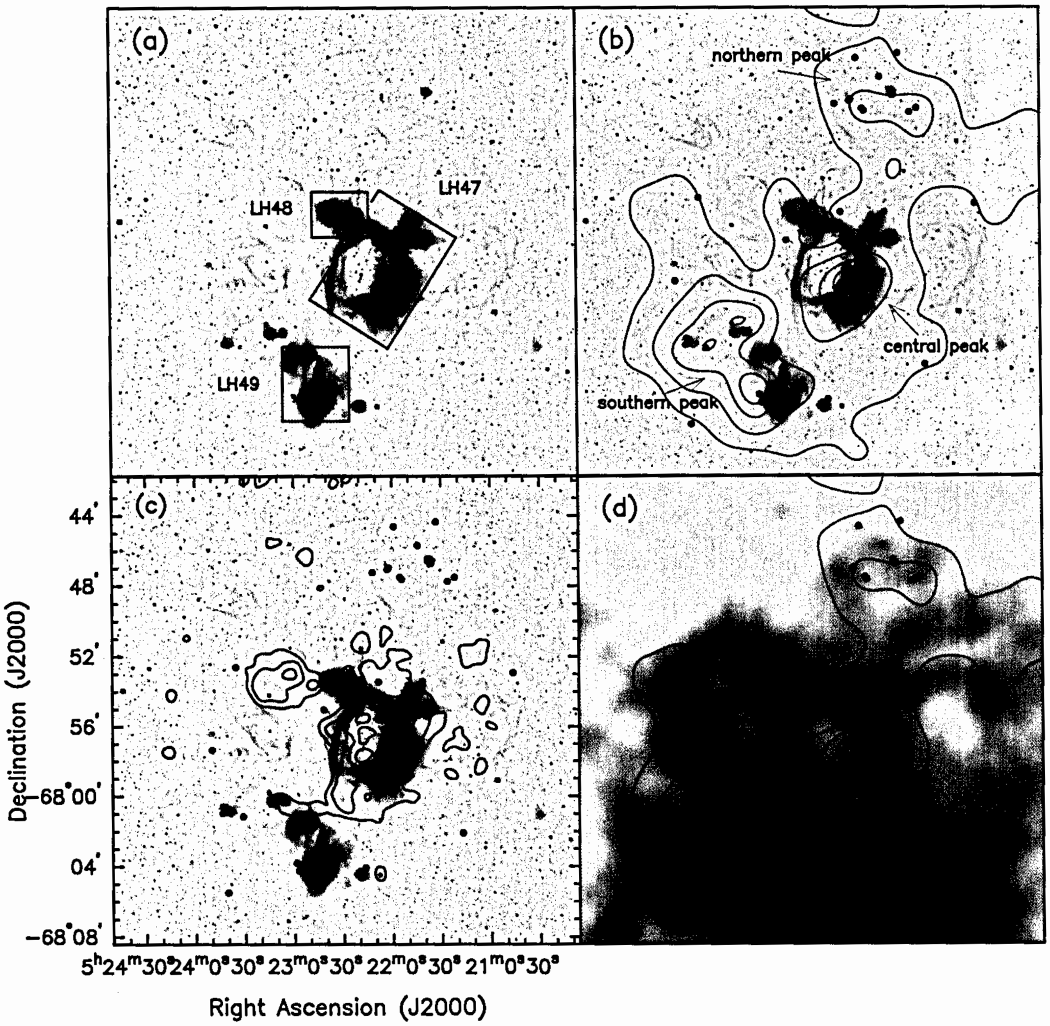

Figure 3.13 Distribution of YSOs with respect to stellar and interstellar environments of N 44. (a) Hα image of N 44. OB associations LH47/48/49 are labeled. (b) YSO positions and CO contours on Hα image of N 44. The three molecular peaks are labeled. (c) YSO positions and X-ray contours on Hα image of N 44s. (d) YSO positions and CO contours on ACTA+Parkes H I map of N 44.

Table 3.1. Parameters used in IRAC and MIPS Photometric Measurements

Band	Aperture Radius ($''$)	Background Annulus ($''$)	Aperture Correction Factor	Zero-Mag. Flux (Jy)
IRAC 3.6 μm	3.6	3.6-8.4	1.124	277.5
4.5 μm	3.6	3.6-8.4	1.127	179.5
5.8 μm	3.6	3.6-8.4	1.143	116.6
8.0 μm	3.6	3.6-8.4	1.234	63.1
MIPS 24 μm	6	20-32	1.699	7.14
70 μm	16	39-65	2.087	0.775
160 μm	40	75-125	1.884	0.159

Table 3.2. Effective Wavelength and Zeroth-Magnitude Flux of $UBVIJHK_s$ Bands

	U	B	V	I	J	H	K_s
Effective Wavelength (μm)	0.367	0.436	0.545	0.797	1.235	1.662	2.159
0^{th} mag F_ν (Jy)	1780	4000	3600	2420	1594	1024	666.8

Note. — Adopted from Bessell & Murdin (2000) for $UBVI$, Cohen et al. (2003) for JHK_s.

Table 3.3: Multi-wavelength Photometry of YSO Candidates Selected from CMD Criteria

Name	R.A.	Decl.	No.	U	B	V	J	H	K_s	[3.6]	[4.5]	[5.8]	[8.0]	[24]	[70]	Type[4]	Remarks[5]
052002.1-680420.9	80.00858	-68.07248	73	...	...	...	15.55	14.79	14.42	13.32	13.19	12.25	9.42	6.20	1.12	G?	
052021.5-674950.1	80.08949	-67.83057	87	...	...	...	14.30	13.50	13.34	13.14	13.15	12.04	10.47	...	...	red S	
052038.6-674031.3	80.16074	-67.67536	97	...	...	...	16.20	15.43	14.51	...	13.55	...	11.20	...	...	G	
052042.0-674307.7	80.17511	-67.71881	102	...	...	...	16.06	15.04	14.71	13.85	13.81	13.61	11.64	9.30	...	G	
052046.6-675255.1	80.19423	-67.88196	17	...	...	...	...	...	...	12.45	12.46	9.53	7.81	3.88	-0.79	C2	
052106.8-675715.9	80.27851	-67.95443	105	...	...	...	16.61	15.44	15.18	14.23	13.99	...	11.79	...	...	G	
052117.5-680204.6	80.32294	-68.03462	43	...	...	...	...	...	...	13.36	13.25	10.52	8.73	5.40	-0.26	G? YSC?	
052120.7-674706.6	80.33626	-67.78516	33	...	...	...	...	...	...	13.03	12.96	10.21	8.51	5.34	...	D	
052120.7-674725.5	80.33627	-67.79042	77	...	...	...	...	...	...	13.65	13.18	11.30	9.54	...	...	S	on IR D
052120.9-674716.7	80.33717	-67.78796	85	...	...	...	...	...	...	13.96	13.20	...	10.40	...	...	D	
052120.9-680217.6	80.33719	-68.03822	104	...	...	...	...	...	...	14.95	13.94	12.70	11.68	7.80	...	ES?	
052122.0-674729.0	80.34170	-67.79138	6	...	...	...	16.08	14.96	14.83	12.08	11.76	9.27	7.44	1.86	-2.17	YSO+RN?	
052126.2-674742.1	80.35918	-67.79504	74	17.62	18.03	17.91	...	...	...	13.54	13.38	...	9.47	5.92	...	C3	in mc
052127.2-675915.1	80.36326	-67.98754	98	15.37	15.43	14.86	13.71	13.38	13.35	13.08	13.38	12.50	11.24	...	...	blue S	
052129.7-675106.9	80.37373	-67.85192	1	14.32	14.96	14.17	13.00	12.02	10.46	8.03	6.96	5.83	4.12	1.00	-2.95	ES	
052133.3-674420.8	80.38864	-67.73912	103	...	...	...	15.90	15.61	14.65	...	13.82	...	11.65	7.98	...	mul YSOs?	
052135.5-675500.2	80.39809	-67.91673	91	...	18.49	17.29	15.09	14.34	14.20	14.04	13.94	12.75	10.89	...	...	S	in dr
052136.0-675443.4	80.39995	-67.91205	67	17.16	17.75	17.28	16.40	15.34	15.23	13.65	13.01	11.48	9.32	...	...	C2/3	
052136.3-674643.2	80.40118	-67.77867	94	...	...	...	...	...	...	15.30	13.65	12.49	11.06	5.36	...	mul YSOs	
052136.6-675449.4	80.40235	-67.91373	78	...	...	...	...	...	...	13.85	13.87	11.44	9.54	4.04	...	D	
052138.0-674630.3	80.40849	-67.77509	75	...	...	...	...	...	...	13.72	13.91	11.20	9.52	4.80	...	C2	
052141.9-675324.1	80.42460	-67.89003	65	...	...	...	...	...	...	13.90	13.81	11.00	9.26	5.32	...	C2, mul?	
052144.5-674541.5	80.43560	-67.76152	47	...	...	...	16.18	15.41	15.04	13.38	13.36	10.65	8.91	5.87	0.37	YSC?	
052147.1-675656.7	80.44630	-67.94908	19	14.05	14.91	15.30	14.64	14.35	14.00	12.07	11.89	9.63	7.84	2.54	...	C3	
052152.8-675449.5	80.47013	-67.91374	96	13.98	14.94	14.97	14.69	14.43	14.25	13.68	13.39	12.62	11.18	...	...	S	
052154.2-674737.1	80.47602	-67.79364	95	...	...	...	...	...	...	14.41	13.50	12.54	11.10	...	...	C2, mul?	in dc
052155.3-674730.2	80.48030	-67.79172	63	...	...	...	...	...	...	12.90	11.77	10.49	9.20	5.00	...	C2, mul	
052155.3-675634.9	80.48033	-67.94302	48	18.54	19.47	19.01	...	...	...	12.90	12.77	10.61	8.89	4.90	...	C2/3	
052157.0-675700.1	80.48768	-67.95002	80	13.43	14.36	14.42	14.57	14.82	14.66	14.29	13.50	11.90	9.96	3.52	...	C3: O8.5V+N	
052157.5-675618.5	80.48949	-67.93847	61	...	...	...	...	...	...	13.60	13.40	10.95	9.16	4.27	...	D	
052157.9-675625.5	80.49138	-67.94043	70	11.96	12.95	13.12	13.32	13.28	13.16	12.57	12.45	10.83	9.37	...	...	S: O7III((f))	
052158.2-675554.2	80.49265	-67.93172	46	17.62	18.42	18.32	...	...	...	12.34	11.79	10.27	8.81	5.12	...	C2/3	
052159.0-674437.2	80.49602	-67.74367	79	...	...	...	...	...	...	14.13	13.79	11.43	9.71	6.68	...	C2	
052159.6-675721.7	80.49813	-67.95603	82	12.82	13.78	14.03	14.19	14.28	14.25	13.43	12.86	...	10.09	...	...	C3: O7.5V+N	
052159.6-675715.6	80.49830	-67.95432	81	...	...	...	...	...	...	14.32	13.90	11.89	10.05	...	...	D	
052200.4-675745.0	80.50157	-67.96250	27	...	...	...	...	...	...	13.01	13.49	10.23	8.37	...	...	D	
052201.9-675732.5	80.50795	-67.95902	58	...	...	...	...	...	...	13.59	13.39	10.57	9.07	...	...	YSO, mul?	in dc
052202.0-675758.2	80.50814	-67.96617	15	...	...	...	...	...	...	12.69	11.50	9.36	7.77	...	...	C2	in dc
052202.2-675753.6	80.50908	-67.96490	13	...	...	...	...	...	...	12.36	11.95	9.40	7.67	1.75	...	C2	
052202.3-674657.5	80.50974	-67.78263	35	...	...	...	...	...	...	13.18	12.86	10.35	8.51	2.41	...	YSO	in dc
052202.8-674701.9	80.51149	-67.78386	16	...	...	...	16.13	14.28	13.90	12.12	11.75	9.54	7.77	2.01	-2.39	C2	at tip of dc
052203.1-674703.5	80.51291	-67.78431	18	...	...	...	15.05	15.37	13.87	12.10	11.78	9.64	7.81	...	...	C2	
052203.4-675746.9	80.51419	-67.96302	26	...	...	...	...	...	...	12.76	11.78	10.01	8.28	1.74	...	YSO	in dc

continued on next page

Table 3.3: *continued*

Name	R.A.	Decl.	No.	U	B	V	J	H	K_s	[3.6]	[4.5]	[5.8]	[8.0]	[24]	[70]	Type[6]	Remarks[7]
052203.9-675743.7	80.51617	-67.96214	54	...	...	...	...	...	...	12.95	11.82	10.77	8.98	...	...	C2	in dc
052204.1-674709.7	80.51695	-67.78603	76	...	...	...	...	...	...	13.92	13.94	11.24	9.52	...	...	S	on IR D
052204.8-675744.6	80.51992	-67.96240	44	...	...	...	...	...	...	13.29	13.00	10.87	8.76	...	...	C3	at edge of dc
052204.9-675720.6	80.52027	-67.95572	64	...	...	...	...	...	...	13.45	13.42	11.16	9.22	...	...	D	
052204.9-675801.6	80.52042	-67.96710	38	20.70	19.87	19.00	...	...	...	13.08	12.61	10.25	8.54	2.08	...	D	
052205.2-675741.6	80.52165	-67.96156	40	...	...	...	...	...	...	13.39	12.79	...	8.61	...	...	YSO	in dc
052205.3-675748.5	80.52211	-67.96347	23	...	...	...	...	...	...	13.12	12.97	9.88	8.13	2.06	...	YSO	in dc
052206.4-675659.2	80.52652	-67.94978	30	...	...	...	...	...	...	12.28	11.64	9.98	8.41	4.37	...	C2	
052207.3-675819.9	80.53034	-67.97219	21	17.73	18.35	18.16	...	...	...	12.30	11.87	9.71	8.01	2.79	...	C3	in HII
052207.3-675826.8	80.53046	-67.97410	28	...	...	...	17.71	15.92	14.92	11.99	10.54	9.43	8.38	3.05	...	C2	in dc
052207.7-675649.4	80.53189	-67.94706	90	18.68	18.91	19.03	...	...	...	14.19	13.94	12.50	10.69	...	...	S	in dr
052208.5-675821.3	80.53526	-67.97258	32	...	...	...	...	...	...	12.93	12.46	10.16	8.45	2.90	...	D	
052208.6-675805.5	80.53580	-67.96819	53	...	...	...	...	...	...	12.32	11.68	10.42	9.01	4.44	...	mul YSOs	
052208.6-675921.9	80.53599	-67.98942	72	18.00	18.75	18.68	...	...	...	13.79	13.83	11.10	9.38	5.92	...	C2, mul?	
052208.8-675325.2	80.53664	-67.89034	62	18.61	18.98	18.68	...	...	...	13.35	13.13	10.79	9.19	5.63	...	C2 + C3/S	
052208.9-674703.4	80.53724	-67.78427	99	...	...	...	14.11	13.61	13.52	13.33	13.38	12.64	11.37	...	...	blue S	
052211.9-675818.1	80.54972	-67.97169	50	...	...	...	...	...	...	14.01	12.69	10.92	8.97	2.04	...	C1	in dc
052212.0-674713.9	80.55009	-67.78720	83	...	...	...	...	...	...	13.63	12.74	11.40	10.10	6.43	...	C2	
052212.3-675813.4	80.55122	-67.97040	51	...	...	...	16.50	15.34	14.87	12.99	12.24	10.61	8.97	...	...	C2 or 2/3	on dc
052212.6-675832.2	80.55242	-67.97562	2	...	...	...	16.03	14.51	12.47	9.44	7.92	6.51	5.10	0.61	-3.85	C1	
052216.7-675837.7	80.56976	-67.97715	57	...	...	...	...	...	...	13.92	13.57	10.85	9.07	...	...	D	
052216.8-680428.3	80.57004	-68.07453	68	...	...	...	...	...	...	13.91	13.92	11.12	9.32	4.96	...	D peak	
052216.9-680403.6	80.57053	-68.06766	36	...	...	...	...	...	...	12.81	11.59	9.96	8.52	4.01	...	C1	
052217.8-680432.9	80.57411	-68.07580	71	...	...	...	...	...	...	13.80	13.68	11.07	9.36	...	...	D	
052218.9-675813.8	80.57877	-67.97051	66	...	...	...	...	...	...	...	13.84	11.21	9.31	...	...	D	
052219.8-680436.8	80.58243	-68.07690	5	...	18.24	18.16	...	...	...	11.20	10.61	8.60	6.87	1.93	-2.62	C1/2	in dc
052221.0-680515.3	80.58770	-68.08759	100	...	...	...	...	...	...	15.35	13.85	12.81	11.38	8.32	...	ES?	
052227.7-675412.8	80.61540	-67.90356	39	...	...	...	...	...	...	13.05	12.95	10.32	8.55	4.20	...	YSO	in dc
052229.1-675339.5	80.62127	-67.89430	52	16.11	17.04	16.65	14.62	15.40	14.71	13.08	13.05	10.68	9.00	5.34	...	C3	
052230.4-675443.9	80.62659	-67.91219	20	16.11	16.75	16.40	14.84	14.42	13.62	11.93	11.38	...	7.88	2.38	-2.69	S	in HII
052231.8-680319.2	80.63232	-68.05534	29	18.75	19.65	19.59	...	...	...	12.75	12.33	10.11	8.40	3.85	...	C2	in dc?
052232.7-680301.7	80.63607	-68.05046	55	...	...	...	...	...	...	13.06	12.69	10.90	9.02	4.42	...	C2 mul	in dc
052241.4-675508.2	80.67255	-67.91894	88	16.15	16.19	15.55	14.12	13.62	13.57	13.37	13.33	12.02	10.52	...	...	S	
052242.0-675500.5	80.67508	-67.91680	84	...	...	...	...	...	...	14.04	13.21	11.66	10.24	5.50	...	C2	
052249.0-680111.1	80.70409	-68.01975	69	...	...	...	...	...	...	13.93	13.76	11.20	9.36	...	...	D	
052249.2-680129.0	80.70512	-68.02471	25	17.66	18.41	17.98	15.78	15.15	14.53	12.51	12.34	9.97	8.26	4.27	...	C2	
052251.0-680401.0	80.71251	-68.06694	37	...	...	...	...	...	...	13.16	13.21	10.32	8.52	...	...	D	
052251.7-680436.7	80.71540	-68.07687	41	18.35	19.07	18.76	...	...	...	12.98	12.80	10.41	8.63	...	...	S	near dc
052253.7-680434.8	80.72392	-68.07632	22	...	...	...	...	...	...	12.85	12.57	9.82	8.12	2.01	...	D	
052254.6-680424.3	80.72737	-68.07342	12	...	...	...	...	...	...	12.04	11.90	9.52	7.65	...	...	D	
052254.9-680422.2	80.72855	-68.07282	8	...	...	...	...	...	...	11.93	11.67	9.32	7.49	1.64	...	D	
052255.2-680409.5	80.72985	-68.06930	10	17.16	18.31	18.00	15.74	15.06	14.31	12.08	11.70	9.37	7.63	2.35	...	C2	
052255.4-680431.6	80.73093	-68.07545	24	...	20.69	20.15	...	...	...	13.15	13.05	...	8.25	...	...	D	

continued on next page

Table 3.3: *continued*

Name	R.A.	Decl.	No.	U	B	V	J	H	K_s	[3.6]	[4.5]	[5.8]	[8.0]	[24]	[70]	Type[6]	Remarks[7]
052256.8-680406.9	80.73687	-68.06858	14	19.23	20.00	19.52	17.00	15.56	14.69	12.25	12.26	9.46	7.76	3.29	...	C2	
052257.6-680414.1	80.74003	-68.07059	42	...	...	...	...	...	...	13.52	12.14	10.28	8.70	3.65	...	C1/2	
052259.0-680346.3	80.74566	-68.06287	86	...	...	...	...	...	...	13.16	12.49	11.61	10.46	5.49	...	C1/2	
052308.7-680006.8	80.78623	-68.00188	45	...	...	...	...	...	...	13.53	12.94	10.61	8.78	3.51	...	YSC	in dc
052309.4-680205.5	80.78932	-68.03487	60	18.48	18.91	18.63	...	...	...	13.69	13.78	10.88	9.15	6.04	...	D peak	
052311.4-680040.9	80.79755	-68.01137	56	...	...	...	...	...	...	13.52	13.41	10.81	9.07	4.62	...	D peak	
052315.1-680017.0	80.81296	-68.00473	59	13.40	14.19	14.10	13.70	13.68	13.49	13.02	12.62	11.20	9.10	2.32	...	C3	in HII
052318.0-675938.6	80.82502	-67.99405	34	...	...	...	16.34	15.94	14.70	13.15	12.73	10.25	8.51	...	...	D	
052318.0-675942.8	80.82519	-67.99521	49	...	...	...	...	...	...	13.49	12.94	10.59	8.94	...	...	D peak	
052331.5-680107.9	80.88107	-68.01887	31	17.64	18.27	17.59	16.02	15.28	14.92	12.91	12.83	10.19	8.42	4.44	...	C2	
052335.6-675235.4	80.89829	-67.87650	9	16.58	17.19	16.95	15.63	14.88	13.62	11.33	10.60	9.03	7.59	2.22	-1.43	C2	
052340.6-680528.5	80.91909	-68.09126	92	...	...	...	15.56	15.66	15.20	14.16	13.45	12.67	10.95	4.90	0.58	C3 or B[e]	
052343.6-680034.2	80.93160	-68.00951	4	...	...	...	...	...	...	11.50	10.59	8.54	6.75	1.12	-2.55	C1/2	
052343.9-680056.1	80.93304	-68.01557	93	...	...	...	...	...	...	14.16	13.71	12.40	11.00	...	...	mul YSOs	
052350.1-675719.7	80.95866	-67.95546	11	...	...	...	...	...	...	12.62	11.46	9.48	7.63	1.35	-2.54	C1	
052351.1-675326.6	80.96288	-67.89073	101	...	...	...	...	...	...	14.54	13.60	12.52	11.54	9.07	...	ES?	
052409.0-674541.3	81.03730	-67.76145	7	...	...	...	...	...	...	...	11.10	9.33	7.42	3.64	...	AGB/pAGB	
052443.0-675709.1	81.17898	-67.95253	89	...	...	...	15.62	14.99	14.95	14.11	13.71	13.37	10.60	...	...	G?	
052458.5-675838.6	81.24359	-67.97729	3	...	...	...	...	...	...	10.32	8.91	7.65	6.48	4.30	...	ES	

---

[7] G: background galaxy, N: nebula, RN: reflection nebula, S: star, YSC: young star cluster, dc: dark cloud, dr: dusty region, mc: molecular cloud, mul: multiple.

Table 3.4 Inferred Physical Parameters from SED Fits to YSOs

			Physical Properties Inferred from the Best-Fit Model							
	# of		A_V	M_*	T_*	Age	M_{env}	M_{disk}	M_{disk}	L_{tot}
YSO Name/Class	Fits	χ^2	mag	$M_\odot$	K	yr	$M_\odot$/yr	$M_\odot$/yr	$M_\odot$	$L_\odot$
052212.6-675832.2/C1	1	120.64	2.4	23.2	3.2E+04	2.0E+04	5.1E-03	4.0E-06	2.6E-01	9.2E+04
052343.6-680034.2/C1/2	3	481.03	20.8	24.7	3.8E+04	7.9E+04	1.9E-04	3.5E-07	4.5E-03	7.8E+04
052219.8-680436.8/C1/2	1	338.72	8.2	14.0	2.7E+04	4.8E+04	2.4E-03	6.1E-05	7.5E-02	2.7E+04
052350.1-675719.7/C1	3	312.18	14.1	22.8	3.7E+04	1.0E+05	3.3E-04	6.2E-07	2.9E-03	6.4E+04
052216.9-680403.6/C1	4	15.62	13.6	12.2	5.7E+03	1.3E+04	1.8E-03	5.5E-07	1.8E-02	5.5E+03
052257.6-680414.1/C1/2	13	4.46	23.0	14.7	7.0E+03	1.0E+04	6.0E-03	5.4E-06	7.9E-03	1.1E+04
052211.9-675818.1/C1	236	0.22	26.9	15.7	3.2E+04	2.8E+05	1.2E-04	4.7E-06	7.7E-02	2.4E+04
052335.6-675235.4/C2	1	3186.11	0.0	16.0	3.2E+04	7.9E+05	3.2E-07	3.2E-08	2.2E-02	2.5E+04
052255.2-680409.5/C2	1	596.72	0.3	15.0	3.1E+04	7.8E+05	2.9E-07	4.4E-10	3.0E-03	2.1E+04
052202.2-675753.6/C2	11	61.56	7.9	18.7	3.4E+04	3.7E+05	1.8E-04	1.9E-09	6.8E-04	3.8E+04
052256.8-680406.9/C2	1	384.64	1.1	14.5	3.1E+04	1.8E+06	0.0E+00	2.1E-08	2.8E-01	1.9E+04
052202.8-674701.9/C2	3	320.71	0.3	11.6	2.8E+04	1.2E+05	2.0E-05	9.4E-08	8.9E-04	9.9E+03
052046.6-675255.1/C2	1	2699.02	4.1	12.2	5.7E+03	1.3E+04	1.8E-03	5.5E-07	1.8E-02	5.5E+03
052249.2-680129.0/C2	2	1121.38	0.7	7.9	1.6E+04	1.7E+05	1.0E-05	1.8E-07	6.0E-02	4.3E+03
052207.3-675826.8/C2	144	9.19	1.3	11.8	2.8E+04	1.4E+05	1.7E-04	8.5E-06	1.4E-02	1.1E+04
052331.5-680107.9/C2	1	725.30	0.9	7.9	1.6E+04	1.7E+05	1.0E-05	1.8E-07	6.0E-02	4.3E+03
052158.2-675554.2/C2/3	3	98.91	0.8	8.7	2.4E+04	1.9E+06	0.0E+00	1.1E-06	6.0E-02	4.0E+03
052155.3-675634.9/C2/3	15	112.41	1.7	7.7	2.2E+04	7.6E+05	5.0E-07	5.5E-06	1.2E-01	2.7E+03
052136.0-675443.4/C2/3	86	79.71	1.4	10.9	2.7E+04	2.7E+06	0.0E+00	3.5E-14	9.4E-08	8.3E+03
052147.1-675656.7/C3	1	17240.04	0.0	16.1	3.2E+04	1.3E+06	0.0E+00	2.4E-08	1.5E-01	2.5E+04
052207.3-675819.9/C3	5	359.92	0.5	10.1	2.6E+04	2.4E+05	9.2E-06	3.0E-07	5.2E-02	6.4E+03
052229.1-675339.5/C3	10	494.13	1.1	13.4	3.0E+04	1.9E+06	0.0E+00	4.8E-12	3.2E-06	1.5E+04
052315.1-680017.0/C3	1	36467.65	0.0	24.6	3.8E+04	1.1E+06	0.0E+00	2.8E-07	1.8E-01	7.7E+04
052126.2-674742.1/C3	4	652.78	1.6	10.6	2.6E+04	2.8E+06	0.0E+00	2.1E-13	1.1E-07	7.4E+03
052157.0-675700.1/C3	1	5896.11	0.0	20.7	3.6E+04	1.3E+06	0.0E+00	4.7E-12	2.4E-06	5.0E+04
052159.6-675721.7/C3	1	89567.12	0.0	16.0	3.2E+04	1.4E+06	0.0E+00	1.5E-11	4.7E-07	2.5E+04
052340.6-680528.5/C3	2	2773.92	0.0	9.4	2.5E+04	2.3E+06	0.0E+00	5.6E-12	5.5E-07	5.0E+03

Chapter 4

Massive Star Formation in Giant H II Regions in M101

Previously published in The Astrophysical Journal as Chen, Chu, & Johnson, 2005 ApJ, 619, 779-799, reproduced by permission of the American Astronomical Society.

4.1 Introduction

Giant H II regions (GHRs) are sites of intense massive star formation. Their Hα luminosities, 10^{39}–10^{41} ergs s^{-1} (Kennicutt, 1984), require an ionizing power equivalent to that of 24–2400 O5V stars (Schaerer & de Koter, 1997). With such high concentrations of massive stars, GHRs provide an excellent laboratory to study the modes of massive star formation, and in particular to probe whether they are birthplaces of globular clusters (Kennicutt & Chu, 1988).

In the two nearest GHRs, 30 Dor in the Large Magellanic Cloud (LMC) and NGC 604 in M33, where stellar contents are well resolved, two distinct types of stellar groupings have been observed: 30 Dor is dominated by one central massive cluster R136 (Hunter et al., 1995; Walborn & Blades, 1997), while NGC 604 contains multiple OB associations spreading over a large area (Hunter et al., 1996). Evidently, not all GHRs contain massive compact clusters; what physical environments give rise to the various cluster morphologies is currently under investigation.

One obvious way to elucidate this issue is to carry out detailed examinations of relatively nearby clusters and their environments. Maíz-Apellániz (2001) studied 27 nearby (< 5 Mpc) clusters of varying morphological types, primarily classifying clusters based on their core and halo sizes. He suggests that compactness of clusters is predominantly related to the central density of the progenitor giant molecular cloud, i.e., extremely high pressure environments may be required to form massive compact clusters. However, this scenario has not been observationally tested; we do not know the pressures and densities of the giant molecular cloud in which optically visible clusters were formed. Examining clusters in a range of present-day environments may help us gain insight into their properties and relationship to their natal interstellar medium.

Of all massive compact clusters, the most impressive ones are the super-star clusters (SSCs) with masses of 10^5–10^6 $M_\odot$. SSCs are frequently observed in galaxy mergers and starburst galaxies (Whitmore, 2003, and references therein), and they are believed to be preferentially formed in high-pressure interstellar conditions (e.g., Elmegreen & Efremov, 1997). However, some GHRs in non-interacting, late-type spiral galaxies may also host SSCs, especially those GHRs that are several times as luminous as 30 Dor and require ionizing powers rivaling those of young SSCs (e.g., Luridiana & Peimbert, 2001). It is thus intriguing to examine the cluster content of such GHRs and investigate whether these relatively quiescent environments can also produce SSCs.

The giant spiral galaxy M101 contains a large number of very luminous GHRs whose stellar content can be resolved and studied with *Hubble Space Telescope* (*HST*) images. We have therefore obtained *HST* observations of three M101 GHRs with different morphologies and galactic locations: NGC 5461, NGC 5462, and NGC 5471. The locations of these GHRs in M101 are marked on a Second Palomar Observatory Sky Survey (POSS-II) red image in Figure 4.1. The properties of these GHRs are summarized in Table 4.1; for comparison, 30 Dor is also included in this table. We have used the *HST* continuum and Hα images of these three GHRs to carry out a detailed photometric study of their clusters. This paper reports our observations (§4.2) and methodology (§4.3), describes the cluster content in each GHR (§4.4), discusses cluster properties and their implications in studying massive star formation and cluster formation (§4.5), and summarizes our results (§4.6).

4.2 Observations and Data Reduction

The *HST* WFPC2 images of the GHRs NGC 5461, NGC 5462, and NGC 5471 were obtained for the Cycle 6 program GO-6829. The observations were made through the continuum filters F547M (Strömgren y) and F675W (WFPC2 R), and the Hα filter F656N (for filter characteristics, see Biretta et al., 1996). Multiple exposures in each filter were made with a GHR centered on a Wide Field Camera (WFC) for photometric measurements. Two short exposures in F547M with the GHR centered on the Planetary Camera (PC) were also made for cluster size measurements. The observations are listed in Table 4.2.

We received the *HST* pipeline processed WFPC2 images and then reduced them further with the IRAF and STSDAS routines. All images were corrected for the intensity- and position-dependent charge transfer efficiency (CTE) by applying a linear ramp with a correction factor chosen according to the average counts of the sky background (Holtzman et al., 1995). Images in each filter were then combined to remove cosmic rays and to produce a total-exposure map. To better illustrate the spatial correlation between the stars/clusters and the ionized gas, we have produced color images of the three GHRs using a customized IDL routine. The individual F547M, F675W, and Hα images were mapped to the colors blue, green, and red, respectively. These images were transformed to a logarithmic scale, and the maximum and minimum flux values for each filter were chosen in order to maximize the dynamic range of the image while also creating a relatively black background. The color images of NGC 5461, NGC 5462, and NGC 5471 are shown in Figures 4.2–4.4, where the ionized gas appears red and most stars blue. The individual F547M, F675W, and Hα images of NGC 5461, NGC 5462 and NGC 5471 are presented in Figures 4.5–4.7, respectively.

Aperture photometry was carried out using the IRAF task `apphot` for the F547M and F675W images. Owing to the small number of identifiable candidate sources and the complex blending and irregular background in some regions, we manually selected compact sources with obvious peaks as candidate clusters in the three GHRs. The candidate clusters in the three GHRs are marked in Figures 4.5–4.7. The apparent magnitudes, $m_{\rm F547M}$ and $m_{\rm F675W}$, were measured with the WFC images using a source aperture of radius 2 pixels ($0\farcs2$) and an annular background aperture of radii 6–11 pixels. For clusters with neighboring clusters within $\lesssim 0\farcs3$, such as #8, #9 and #10 in NGC 5461 and #1 and #2 in NGC 5471, the photometry was measured with a $0\farcs15$-radius source aperture using both the WFC and PC images. The corrections from the $0\farcs15$-radius aperture to the $0\farcs2$-radius aperture are determined by measuring isolated resolved and unresolved sources in each image, and are in the range of -0.2 to -0.3 mag. The fluxes of these clusters will be over-estimated from the WFC images due to the inclusion of neighbor's light, and the errors are larger for the fainter clusters. For example, the error in the $m_{\rm F675W}$ of NGC 5461-9 may be as large as -0.4 mag, which is estimated by comparing its $m_{\rm F547M}$ measured from the PC and WFC images.

We have derived the magnitudes in the VEGAMAG system. The errors in $m_{\rm F547M}$ given by `apphot` are ~ 0.01 mag for $m_{\rm F547M} \leq 20$, and rise to 0.02–0.03 mag for $m_{\rm F547M} = 20$–21. The errors in $m_{\rm F675W}$ are generally larger, with most of them ≤ 0.02 mag but some as high as 0.04 mag. These formal errors are derived from the flux variations in the background annulus used in the photometric measurements. In regions with bright irregular backgrounds, using different background apertures may produce different photometric results and the uncertainties in photometry will be larger than the formal errors given by `apphot`. We have taken these uncertainties into account and estimated realistic errors.

The bright irregular sky background is attributed to both stars and nebulosity. The extended distribution of unresolved stars, similar to the "star clouds" defined by Lucke & Hodge (1970) for OB associations in the LMC, raises the background in both the F547M and F675W images. We find that using different annular sky backgrounds results in uncertainties of $\sim$ 0.03–0.05 mag in $m_{\rm F547M}$ for sources near modest star clouds, $\sim$ 0.1 mag for sources surrounded by bright star clouds, and up to $\sim$ 0.2 mag for faint sources near bright star clouds. The stellar background does not affect the $(m_{\rm F547M} - m_{\rm F675W})$ color as much because the variations in m_{F547M} and m_{F675W} are correlated. The bright nebular background, on the other hand, contributes uncertainties only to m_{F675W} and hence affects the color. The uncertainties in the $(m_{\mathrm{F547M}} - m_{\mathrm{F675W}})$ color are $\sim$ 0.05–0.06 mag for most sources near nebulosities, and up to $\sim$ 0.16 mag for faint stellar sources near bright nebulosity.

To reduce the uncertainties introduced by nebular contamination in the F675W images, we have produced Hα-free F675W images by subtracting scaled Hα images from the F675W images. The Hα-subtracted F675W images of the three GHRs are also presented in Figures 4.5–4.7. Aperture photometry has been carried out for the Hα-subtracted F675W images, and the apparent magnitude is designated as $m_{\mathrm{F675W'}}$. The uncertainties in the $(m_{\mathrm{F547M}} - m_{\mathrm{F675W'}})$ color with different annular sky backgrounds are reduced to $\sim$ 0.02–0.05 mag for most candidate cluster sources near nebulosities.

Our $0\farcs2$-radius source aperture does not include all the light from a cluster. The correction from a $0\farcs2$-radius aperture to a $0\farcs5$-radius aperture, which includes $\sim$ 95% of the light of a point source (Holtzman et al., 1995), is $\sim -0.20 \pm 0.06$ mag for unresolved sources and larger for resolved sources. As the cluster candidates are resolved to different extents, the aperture corrections are in the range of -0.2 to -0.3 mag but difficult to determine exactly. We have chosen not to apply aperture corrections; therefore, our photometric measurements are systematically fainter by 0.2–0.3 mag, but the analysis and conclusions of this paper are not sensitive to such small offsets that incur on the magnitudes and colors of the clusters.

The photometric results of NGC 5461, NGC 5462 and NGC 5471 are presented in Tables 4.3–4.5, and plotted in the color-magnitude diagram (CMD) of M_{F547M} versus $(M_{\mathrm{F547M}} - M_{\mathrm{F675W'}})$ in Figures 4.8–4.10, respectively. For clusters with close neighbors, their M_{F547M} measured from the PC images and their $(M_{\mathrm{F547M}} - M_{\mathrm{F675W'}})$ measured from the WFC images are used in the CMD. These absolute magnitudes are derived using a distance modulus of $(m - M) = 29.3$ (Stetson et al., 1998). The Galactic foreground extinction toward M101, $E(B-V) = 0.01$ (Schlegel et al., 1998), is corrected, although its effect is negligible. The internal extinction from M101 is not individually corrected for, given that it is highly variable and the measurements are only available for certain parts of the GHRs.

4.3 Methodology

The observed magnitudes and colors of the clusters can be used to determine their ages and masses through comparisons with those predicted by population synthesis models (e.g., Elson & Fall, 1985; Bruzual A. & Charlot, 1993; Bruzual & Charlot, 2003; Leitherer et al., 1999). Below we describe the synthetic photometry derived from models and how we use it to estimate the properties of clusters. We have also used the Larsen

(1999) method to measure the sizes of clusters from their surface brightness profiles. The procedures of cluster size measurements are outlined at the end of the section.

4.3.1 Synthetic Photometry

We have used the Starburst99 models (Leitherer et al., 1999) and the Bruzual & Charlot (2003, hereafter BC03) models to generate synthetic photometry for comparison with observations of our cluster candidates in GHRs. We have adopted a Salpeter initial mass function (IMF) with lower and upper mass limits of 1 $M_\odot$ and 100 $M_\odot$, which are commonly used in population synthesis models for star-forming and starburst regions. The luminosity, colors, and evolution of a cluster depend on its metallicity. To select appropriate models, we have used the observed oxygen abundances of the GHRs to assess their metallicities, because clusters and their surrounding GHRs are expected to have the same abundances and the oxygen abundances are well determined. Oxygen abundances of NGC 5461 and NGC 5462, relative to the solar value, have been measured to be 0.6–0.9, while that of NGC 5471 is ~ 0.25 (e.g., Evans, 1986; Scowen et al., 1992; Pilyugin, 2001; Luridiana et al., 2002). Therefore, we adopt the 1 $Z_\odot$ model for NGC 5461 and NGC 5462, and the 0.2 $Z_\odot$ model for NGC 5471.

The F547M and F675W filters we used are not included in the default filter systems of Starburst99 or BC03 for which synthetic photometry is readily available; thus, customized procedures are needed to derive synthetic $M_{\rm F547M}$ and $M_{\rm F675W'}$. As the first step, we use Starburst99 Version 4.0 to generate integrated stellar spectra for a simple stellar population (SSP; i.e., a single-age and single-abundance group of stars) from ages of 0 to 30 Myr at 1 Myr intervals and from 30 to 150 Myr at 3 Myr intervals. This step is not necessary for the BC03 models, as integrated spectra for an SSP are available for most of these age intervals. These model spectra are those without nebular line and continuum emission because the clusters are generally well resolved from the superposed extended nebular emission and the background-subtraction in `apphot` adequately removes the extended nebular emission. The synthetic spectra from Starburst99 and BC03 are then convolved with filter transmission curves, using the IRAF/STSDAS task `calcphot`, to calculate the synthetic $M_{\rm F547M}$ and $M_{\rm F675W'}$. We have produced synthetic photometry for SSPs with metallicities of 0.2 $Z_\odot$ and 1 $Z_\odot$, and generated evolutionary tracks in the CMDs in Figures 4.8–4.10 for comparisons with observations of NGC 5461, NGC 5462, and NGC 5471, respectively. The differences in the two sets of evolutionary tracks reflect the differences between the Geneva and Padova stellar evolution models used by Starburst99 and BC03, respectively. However, the effects of these differences are small compared to the uncertainties in the cluster mass estimates.

We use the R136 cluster at the core of 30 Dor as a reference point, because it is an archetypical populous blue cluster and possibly a young globular cluster. The R136 cluster is $\sim$ 3 Myr old (Hunter et al., 1995; Walborn & Blades, 1997). Its spatially resolved photometry in the V band has been measured and the absolute visual magnitude within a radius of 7 pc is $M_V = -11.1$ (Moffat et al., 1985). This V band magnitude is adopted directly because its central wavelength is similar to that of F547M and the 7-pc-radius aperture matches that used in the photometric measurements of M101 clusters. The $(M_{\rm F547M} - M_{\rm F675W'})$ color of R136 is not available, so we use the synthetic color generated by Starburst99 for a 3 Myr old cluster with $Z = 0.2$–$0.4\ Z_\odot$. As no extinction correction has been applied to the M101 clusters, we have reddened the synthetic color of R136 with its visual extinction $A_V = 1.2$ (Moffat et al., 1985) and marked both the dereddened and reddened R136 in the CMDs in Figures 4.8–4.10.

4.3.2 Assessing Masses and Ages of Clusters

The mass and age of a cluster can be assessed by comparing its magnitudes and colors to model predictions if photometric data are available in three passbands. For a young cluster, it is important to include a U band or a B band because the spectral energy distribution of young massive stars peaks in the ultraviolet wavelengths. Unfortunately, only F547M and F675W photometry is available for the clusters in M101 GHRs, and these two bands are not as sensitive to the young massive stars as the U and B bands. We cannot determine unambiguously the cluster masses and ages by comparing the photometric measurements with the evolutionary tracks of SSPs in the CMDs. However, we may use the interstellar environment as an independent diagnostic of the cluster age, as the interstellar medium around a cluster evolves as a result of stellar energy feedback.

At ages < 5 Myr, a cluster has the highest ionizing power, and hence will be in a dense, luminous H II region. At ages 5–10 Myr, the fast stellar winds and supernova explosions from a cluster have swept up the ambient ISM into a supershell with a visible cavity around the cluster. At ages > 10 Myr, a cluster loses its ionizing power and has dispersed its ambient gas, so it will be surrounded only by diffuse gas with low surface brightness. We have compared the Hα images with the continuum images to examine the interstellar environment of the clusters and to assess the approximate ages of the clusters. In Figures 4.8–4.10, we mark circles around the clusters that are coincident with compact, luminous H II regions, and dashed circles around the clusters that are in supershells, indicating that their ages are < 5 Myr and 5–10 Myr, respectively. The unmarked clusters, not surrounded by bright Hα emission, are older than 10 Myr, but their exact ages are poorly constrained.

With a rough estimate of the cluster age, it is then possible to compare the location of a cluster in the CMD with the synthetic evolutionary tracks of clusters to determine the cluster mass. The photometric measurements of the clusters have not been corrected for the extinction within M101, thus using these reddened magnitudes would underestimate cluster masses. To illustrate the effect of extinction and to make a rough correction, we take the visual extinctions of the GHRs determined from their Balmer decrements by Kennicutt & Garnett (1996), and plot the corresponding reddening vectors in Figures 4.8–4.10. We have adopted these nebular extinctions and made reddening-corrected estimates of masses for clusters more luminous than $M_{\rm F547M} = -9$. The age and mass estimates of these luminous clusters are given in Table 4.6. We do not attempt to estimate masses for fainter clusters because these luminosities overlap those of single supergiants (Humphreys & Davidson, 1979). Furthermore, many faint clusters are not surrounded by bright nebulosity, indicating poorly constrained ages at >10 Myr, so their mass estimates would be highly uncertain.

We have used the R136 cluster to estimate the uncertainties in our cluster mass estimates. From the extinction-corrected location of R136 in the CMD, we estimate a mass of $\sim 2 \times 10^4$ $M_\odot$. The mass of R136 has been derived from its resolved stellar content to be 2.2 $\times 10^4$ $M_\odot$ (Hunter et al., 1995) by summing the masses of stars ≥ 2.8 $M_\odot$ (mass cutoff limited by completeness) within a 4.7-pc radius. Note however that our estimate of mass is based on the luminosity of R136 within a 7-pc radius and a minimum stellar mass of 1 $M_\odot$. Our mass estimate of R136 using the 4.7-pc radius aperture (Moffat et al., 1985) and the 2.8 $M_\odot$ lower mass limit is 1.4 $\times 10^4$ $M_\odot$, about 40% lower than that derived from the resolved stellar content. Therefore, the uncertainties in our cluster mass estimates are at least 40%.

4.3.3 Assessing Cluster Sizes

Some of our clusters appear resolved in the PC images, so it is possible to determine their sizes. The size of a cluster can be described by its effective radius, $R_{\rm eff}$, the radius that encircles half of the cluster light. The $R_{\rm eff}$ of a cluster can be estimated with the routine `ishape` developed by Larsen (1999). In this routine, the surface brightness profile of a cluster is modeled by an analytic function and convolved with a point spread function (PSF) calculated with the TINY TIM Version 6.0 (Krist, 1995) for the cluster's position on the PC chip. The PSF-convolved model profile is then compared with the observed cluster profile. The best-fit model, judged by the χ^2 statistics, gives the full width at half maximum (FWHM) of the analytic function, which is then used to determine $R_{\rm eff}$.

We have used the two most common analytic functions, the Gaussian and the King (1962) profiles, to model the clusters. The King profile contains a concentration parameter $c = \log(r_{\rm t}/r_{\rm c})$, where $r_{\rm t}$ is the tidal radius and $r_{\rm c}$ is the core radius. Typically c is within the range of 1.0–2.0 for globular clusters in the Galaxy (Harris, 1996) and young rich clusters in the LMC (Elson et al., 1987). We have experimented with different values of c within this range in the model fits, and found that for a cluster detected with $S/N \geq 15$, the best-fit $R_{\rm eff}$ is insensitive to the concentration parameter c or even the form of the analytic function. For a bright cluster with adequate S/N, the $R_{\rm eff}$ is estimated using both the Gaussian and the King profiles, and the average of the two estimates is adopted and given in Table 4.6.

All but one of the cluster sizes we measured are in the range of $R_{\rm eff} = 0\farcs02$–$0\farcs09$, corresponding to 0.7–2.9 pc. (Note that $R_{\rm eff}$ can be smaller than the pixel size of $0\farcs0455$, because the PSF effects have been considered and removed in the profile fitting.) The only exception is NGC 5471–9, whose $R_{\rm eff}$ is only $0\farcs005$; as we discuss later in §4.4.3, NGC 5471–9 is most likely a luminous A-F supergiant, instead of a cluster. The sizes of these M101 clusters are within the range of clusters in the Galaxy and nearby galaxies. For example, the globular clusters in the Galaxy have $R_{\rm eff} \sim$ 1–5 pc, with a median of ~3 pc (Harris, 1996); the compact young cluster R136 in the LMC has $R_{\rm eff} \sim 0.9$ pc (Mackey & Gilmore, 2003)[1]; compact young massive clusters in nearby starburst galaxies where stars are not resolved have $R_{\rm eff} \sim$ 2–4 pc (Meurer et al., 1995). Comparisons between the M101 clusters and R136 will be discussed in more detail in §4.4.

4.4 Clusters in Three Luminous GHRs in M101

Below we describe the spatial distribution, ages, masses, and sizes of the clusters in NGC 5461, NGC 5462, and NGC 5471. The extinctions of individual H II regions in these GHRs are taken from Kennicutt & Garnett (1996).

4.4.1 Clusters in NGC 5461

The GHR NGC 5461 has been loosely defined to be the H II complex extending over a 66″ × 26″ region in ground-based Hα images (Israel et al., 1975). Considering that this area corresponds to a linear size of ~ 2.3 kpc × 0.9 kpc, it is unlikely that the entire region is associated with one coherent star formation event. Indeed, 12 H II regions have been identified within NGC 5461 by Hodge et al. (1990). Our WFPC2 Hα image shows that NGC 5461 contains two regions that would have been individually identified as GHRs if they were in the Local Group: H 1105 and H 1098 (marked in Figure 4.5e; designation from Hodge et al., 1990). H 1105 is 3 times as luminous as 30 Dor, and H 1098 is as luminous as NGC 604, or 1/3 as luminous as 30 Dor. The 10 fainter H II regions are distributed roughly along the axis connecting H 1105 and H 1098 with a higher concentration toward H 1105. We define the "main body" of NGC 5461 to be the region containing H 1105 and H 1098 and their vicinity, as in the field-of-view of Figure 4.5.

The relationship between the stars/clusters and the H II regions is clearly illustrated in the color image

---

[1] The surface brightness profile of R136 indicates a compact, dominant component on top of a broad, shallow component. The $R_{\rm eff}$ is estimated using its core radius of 0.32 pc and a King profile with $c = 1.5$ to approximate the compact component.

of NGC 5461 (Figure 4.2). In addition to the bright H II regions, NGC 5461 also has nebular filaments, loops, and well-defined shells with stars/clusters underneath these interstellar structures. A total of 12 cluster candidates are identified in the main body of NGC 5461; they are listed in Table 4.3 and marked in Figure 4.5f. Only six clusters have $M_{\rm F547M} \leq -9$: five in H 1105 (#6, #8, #9, #10, and #11) and one in H 1098 (#1). A careful inspection of their immediate surroundings shows that all six clusters are superposed on bright H II regions, indicating ages of < 5 Myr. To estimate the masses of these young luminous clusters, we adopt the visual extinctions of $A_V = 1.7 \pm 0.4$ and 0.8 ± 0.1 of H 1098 and H 1105, apply the respective extinction correction, and compare the dereddened cluster positions in the CMD in Figure 4.8 with the evolutionary tracks generated by Starburst99 and BC03 for different SSP masses. Four of the clusters, #1, #6, #9, and #10, show dereddened colors consistent with SSPs at ages < 5 Myr; thus their masses can be estimated in a straightforward manner. The two remaining clusters, on the other hand, have dereddened colors consistent with SSPs at ages greater than 6 Myr. The red colors of clusters #8 and #11 can be caused by large local extinction excesses or stochastic color deviation for low-mass SSPs. We consider the latter more likely, i.e., the cluster contains or is projected near a red supergiant and the cluster color is thus confused. For example, cluster #11 may consist of (or be projected towards) a K0 Ia-O supergiant with $M_V = -9.4$ (Humphreys, 1978) and $(V\text{-}R)_0 = 0.76$ (Johnson, 1966) and a young cluster with $M_{\rm F547M} = -9.2$. The masses of clusters #8 and #11 are determined with the ad hoc assumption of a contaminating red supergiant, which reduces the luminosity of the cluster and lowers the mass estimate accordingly. The mass estimates of the six brightest clusters in NGC 5461 are mostly in the range of 1–3 $\times 10^4$ $M_\odot$ (see Table 4.6). These masses are comparable to that of R136, $\sim 2 \times 10^4$ $M_\odot$.

The PC images of NGC 5461 are used to determine the cluster sizes, but only three clusters, #6, #8, and #10, are detected with $S/N \geq 15$ for reliable size measurements. The $R_{\rm eff}$ estimated for these three clusters are 0.8, 0.7, and 2.1 pc, respectively. While the sizes of clusters #6 and #8 are comparable to that of R136, $R_{\rm eff} = 0.9$ pc, cluster #10 is more extended and shows visible departure from spherical symmetry in the PC image in Figure 4.11. The morphology of cluster #10 suggests that it may be a composite of two clusters with the southwest object brighter than the northeast object.

Among the three GHRs we studied in M101, NGC 5461 is particularly interesting because it is one of the most luminous GHRs in galaxies within 10 Mpc (Kennicutt, 1984). Furthermore, the core of NGC 5461 (i.e., H 1105) has a remarkably high surface brightness with a peak emission measure of 4.4×10^5 cm^{-6} pc, comparable to those of the most active starburst regions. The Hα luminosity of H 1105 implies an ionizing flux rivaling those of SSCs (Kennicutt & Chu, 1988; Luridiana & Peimbert, 2001); thus, NGC 5461 has been considered the most promising site in M101 where SSCs might be found. However, our analysis shows that

H 1105 contains five R136-class clusters, which are by no means in the same league as the SSCs with masses $\sim 10^5$–10^6 $M_\odot$ commonly found in starburst galaxies or mergers (e.g., O'Connell et al., 1994; Whitmore et al., 1999). The core of NGC 5461 is nevertheless striking in its high concentration of stars in a small volume – three clusters with a total mass of 6×10^4 $M_\odot$ in a region of ~ 32 pc ($0\farcs9$) across. It is possible that these clusters are subclusters that will dynamically interact and merge into a cluster that has a mass more typical for SSCs. As shown in the numerical simulations of Bonnell et al. (2003), the hierarchical fragmentation of giant molecular clouds naturally leads to the formation of subclusters that can merge to form the final stellar cluster. If H 1105 were projected to a distance similar to that of the Antennae galaxies (~ 20 Mpc, Whitmore et al., 1999), it would imitate a single cluster as shown in Figure 4.11b, and the combined light of the clusters and the bright stellar background in a $0\farcs2$-radius aperture would have $M_{\rm F547M} = -13.0$, corresponding to a mass of $\sim 10^5$ $M_\odot$. These results suggest that some young SSCs previously identified at distances of $\gtrsim 20$ Mpc may be tight groups of R136-class clusters as seen in the core of NGC 5461.

4.4.2 Clusters in NGC 5462

The GHR NGC 5462 corresponds to a large H II complex with a dimension of $90'' \times 34''$, or 3.2 kpc × 1.2 kpc, in ground-based Hα images (Israel et al., 1975). Thirty-three H II regions have been identified within NGC 5462 (Hodge et al., 1990), but none are comparable to 30 Dor. The overall morphology of NGC 5462 consists of a few bright H II regions distributed along an axis from northeast to southwest and fainter filaments and loops extending outwards from this axis. The two brightest H II regions, H 1170 and H 1176, are each only comparable to NGC 604, or 1/3 as luminous as 30 Dor; the others are much fainter. The distribution of star formation in NGC 5462 is apparently not as concentrated as in NGC 5461. We define the "main body" of NGC 5462 to be the region containing H 1176, H 1170, H 1159 and their vicinity, as in the field-of-view of Figure 4.6.

The color image of NGC 5462 (Figure 4.3) shows a distinct offset between the ionized gas and concentrations of stars, suggesting that the star formation has proceeded from the southeast to northwest. A total of 25 loosely distributed cluster candidates are identified in NGC 5462 (see Table 4.4 and Figure 4.6f). Most of these clusters are faint; only three clusters, #6, #18, and #23, have $M_{\rm F547M} \leq -9$ and are analyzed for their masses. While cluster #18 is superposed on a bright H II region H 1176, indicating an age of < 5 Myr, clusters #6 and #23 are not associated with any H II regions or supershells, indicating ages > 10 Myr. For cluster #18 the visual extinction $A_V = 0.9 \pm 0.4$ of the surrounding H II region H 1176 is adopted, and for the other two clusters the visual extinctions of their nearest H II regions are adopted, i.e., $A_V = 0.6 \pm 0.2$ of H 1159 for cluster #6 and $A_V = 0.9 \pm 0.4$ of H 1176 for cluster #23. We apply the respective extinction correction to each of the three bright clusters and compare their dereddened cluster positions in the CMD in Figure 4.9 with the evolutionary tracks. The young cluster #18 shows a dereddened color consistent with SSPs at ages of < 5 Myr and the estimated mass is $\lesssim 1 \times 10^4$ $M_\odot$. The two older clusters #6 and #23 show dereddened colors consistent with SSPs at ages of > 10 Myr; however, as their ages are poorly constrained, we only obtain their lower mass limits by assuming cluster ages of ~ 10 Myr. We note that unless the two clusters have ages > 30 Myr, their masses would be within a factor of 1.5 of the lower mass limits. The mass estimates of the three brightest clusters in NGC 5462 are in the range of 1–2 $\times 10^4$ $M_\odot$ (see Table 4.6), comparable to the mass of R136.

In the PC images of NGC 5462, only cluster #6 is detected with $S/N \geq 15$ for size measurements. The $R_{\rm eff}$ estimated for this cluster is 2.3 pc, more extended than that of R136. As shown in Figure 4.12, cluster #6 has an asymmetric morphology elongated along the northwest and southeast direction, indicating a complex structure.

NGC 5462 has the lowest Hα surface brightness among the three GHRs we studied in M101. It has a larger number of clusters than the other two GHRs, but only three are R136-class clusters. Furthermore, the clusters do not show obvious spatial concentrations, in sharp contrast to those seen in NGC 5461. The combination of the low Hα surface brightness and sparse distribution of small-mass clusters suggests that the star formation and cluster formation is more spread-out and modest in NGC 5462.

4.4.3 Clusters in NGC 5471

The GHR NGC 5471 extends over a diameter of $\sim 17''$, or ~ 600 pc. Ground-based images of NGC 5471 show five bright knots, which are designated as A, B, C, D, and E components by Skillman (1985) and have been called NGC 5471A–E, respectively. Our color image of NGC 5471 (Figure 4.4) shows that the A-, B-, C-, and E-components display bright H II regions centered on clusters. However, the D-component displays an offset between the H II region and the clusters, which are located to the north and the east sides of a dark cloud, respectively; it is uncertain whether the clusters and the H II region are physically associated. The A-component is as luminous as 30 Dor, and the B-, C-, and E-components are comparable to or fainter than NGC 604.

A total of 19 cluster candidates are identified in NGC 5471; they are listed in Table 4.5 and marked in Figure 4.7f. Most of the clusters reside within the A–E components, with the highest concentration located in the A-component and its western extension. The eight clusters with $M_{\rm F547M} \leq -9$ have been analyzed. We have adopted the visual extinction of each component, applied the respective extinction correction to the eight brightest clusters, and compared the dereddened cluster positions in the CMD with the evolutionary tracks (see Figure 4.10). The comparisons are problematic because most of the dereddened cluster colors do not agree with those expected from the evolutionary tracks. While the disagreements are partially attributed to errors in the extinction and photometric measurements, the dominant cause of the disagreements is probably uncertainties in the stellar evolution models at low metallicities. It is known that at $Z \leq 0.2\ Z_\odot$ stellar evolution models cannot reproduce the observed luminosities and colors of red supergiants or the number ratios of blue to red supergiants (Mayya, 1997; Origlia et al., 1999; Leitherer et al., 1999). These uncertainties directly affect the luminosities and colors of SSPs, particularly at ages around 7 to 14 Myr when red supergiants are significant contributors of the total light. Given these uncertainties, we can make only order-of-magnitude mass estimates for the clusters in NGC 5471.

Four of the clusters we analyzed (#2, #7, #12, and #16) are superposed on bright H II regions, suggesting that they are < 5 Myr old. Clusters #7, #12, and #16 are only ~ 0.1 mag bluer or redder than those expected for young clusters; therefore, we disregard these color differences and use only the $M_{\rm F547M}$ to estimate their cluster masses. Cluster #2, on the other hand, is ~ 0.6 mag redder than the color expected for its young age, and this discrepancy is larger than the known errors in photometry or stellar evolution models. We suggest that this red color excess is likely attributed to a contaminating post-outburst luminous blue variable (LBV) because cluster #2 is located in the C-component where high-velocity (> 1000 km s^{-1}), [N II]-bright nebular emission similar to that of η Car's ejecta nebula has been reported (Castaneda et al., 1990). We assume that cluster #2 contains an LBV similar to η Car, which has $V = 6.22$ and $R = 4.90$ at quiescent states (Mendoza, 1967) and can brighten up by 1–2 mag during outbursts or 3–5 mag during super-outbursts (Humphreys & Davidson, 1994). These quiescent V and R magnitudes can be converted to $M_{\rm F547M} = -8.5$ and $M_{\rm F675W} = -9.4$ using the distance modulus of $(m - M)_0 = 12.79$ and the extinction of $A_V = 1.92$ for η Car's host cluster Trumpler 16 (DeGioia-Eastwood et al., 2001). The remaining members of cluster #2 would have $(M_{\rm F547M} - M_{\rm F675W}) = 0.44$, which is still too red for a < 5 Myr old cluster. However, if the hypothesized LBV is 0.4 mag brighter (during or after an outburst), the rest of cluster #2 would have $(M_{\rm F547M} - M_{\rm F675W}) = -0.1$ as expected for a young cluster and $M_{\rm F547M} = 8.2$. These resultant color and magnitude are used to estimate the mass of cluster #2.

The other four clusters we analyzed (#3, #4, #5, and #9) are not associated with H II regions or supershells, suggesting that their ages are > 10 Myr. However, as discussed in the next paragraph, #9 has a small intrinsic size which makes it more likely a luminous supergiant rather than a cluster. Among the remaining clusters, #4 shows a dereddened color consistent with SSPs at ages > 10 Myr and thus its lower mass limit is easily estimated. Clusters #3 and #5, on the other hand, have dereddened colors ~ 0.2 mag bluer than that of SSPs at ages > 10 Myr. Since their extinction corrections are already small, the disagreements are unlikely to be caused by the uncertainty in extinction measurements. It is most likely that the disagreements arise from the uncertainties in the modeled colors and photometry, so we disregard the blue color excesses when estimating the cluster masses. The mass estimates for the eight bright clusters are in the range of ~ 0.5–2×10^4 $M_\odot$ (see Table 4.6), approaching or comparable to R136.

The cluster sizes are determined using the PC images of NGC 5471. Four clusters, #4, #5, #9, and #16, are detected with $S/N \geq 15$. The $R_{\rm eff}$ estimated for these four clusters are 2.9, 1.4, 0.2, and 1.1 pc, respectively. The small size of cluster #9 suggests that it is either an unresolved star or a post-core-collapse globular cluster (Harris, 1996). Post-core-collapse globular clusters are at least 10^9 yr old (e.g., Heggie, 1985) and thus unlikely to exist in GHRs. We consider it more likely that cluster #9 is a star with magnitudes and colors compatible to those of a luminous A-F supergiant (Moffat & Fitzgerald, 1977; Humphreys et al., 1990). For the three resolved clusters, #16 has a size comparable to that of R136, while #4 and #5 are more extended and show asymmetric, elongated morphologies in the PC image in Figure 4.12.

NGC 5471 has a large number of young clusters with ages < 5 Myr. However, the majority of these young clusters are faint with $M_{\rm F547M} \geq -9$, which may be small clusters with masses of a few $\times 10^3$ $M_\odot$ or just luminous supergiants. Among the cluster candidates in NGC 5471, #4 and #5 are the most massive ones since they are older than 10 Myr and still as luminous as the young R136 cluster, suggesting that their masses are higher that that of R136.

4.5 Discussion

4.5.1 Nature of Faint Cluster Candidates in GHRs

A large number of cluster candidates have been identified in the three M101 GHRs, but the nature of the faintest objects is uncertain. It is possible that some of these faint cluster candidates consist of multiple OB associations as observed in the nearby GHR NGC 604 (Hunter et al., 1996) and some are simply luminous supergiants frequently seen near high concentrations of massive stars, such as 30 Dor (Walborn & Blades, 1997). We have therefore simulated WFPC2 images of 30 Dor and NGC 604 at a distance of 7.2 Mpc and searched for "clusters" using the same criteria as we did for cluster candidates in the M101 GHRs. The spurious clusters in 30 Dor and NGC 604 can be identified because their resolved stellar contents are known. The real and spurious clusters in these two GHRs can then be compared with the cluster candidates in M101 to better assess the nature of the latter.

To simulate a WFPC2 image of 30 Dor at 7.2 Mpc, we have used a green continuum (λ_c = 5130 Å, $\Delta\lambda$ = 155 Å) image from the Magellanic Clouds Emission-Line Survey (MCELS, Smith & The MCELS Team, 1999), and binned the data to 3.5 pc per pixel. The resultant image is displayed in Figure 4.13a. Using the same identification criteria for clusters in M101 GHRs, the two brightest objects in 30 Dor will be selected as clusters: R136 and R131. While R136 is a bona fide cluster, R131 (= HD 269902) is an A0 supergiant with $V = 10.0$ (corresponding to $M_V + A_V = -8.5$) and hence a spurious cluster. The mis-identification of R131 as a cluster bolsters our choice of a luminosity cutoff of $M_{\rm F547M} = -9.0$ for cluster mass estimates (§4.3.2), as the fainter cluster candidates may be single supergiants. It is interesting to note that two other concentrations of stars in 30 Dor are not identified as clusters: the Hodge 301 cluster (Hodge, 1988) and the OB association LH 99 (Lucke & Hodge, 1970). The Hodge 301 cluster, with an age of ~ 20–25 Myr and a mass of a few 10^3 $M_\odot$ (Grebel & Chu, 2000), is too faint to meet our cluster identification criteria. LH 99, on the other hand, is too distributed to mimic a cluster.

A WFPC2 image of NGC 604 at 7.2 Mpc is simulated with its archival WFPC2 F547M image. Adopting a distance of 0.84 Mpc to M33 (Freedman et al., 1991), the data are binned to 3.5 pc per pixel, and the resultant image is displayed in Figure 4.13b. The OB associations in NGC 604 appear as small concentrations on top of an irregular stellar background. The four brightest concentrations have $M_{\rm F547M} = -8.0$ to -9.0, luminous enough to meet our identification criteria for M101 clusters. However, most of the concentrations have irregular shapes, and the brightest one does not even have an obvious boundary. Therefore, the NGC 604-type OB associations may mimic faint clusters at best, with luminosities rivaled by those of supergiant stars.

For a direct comparison between M101 GHRs and the simulated 30 Dor and NGC 604 at 7.2 Mpc, Figure 4.13 displays their images in the same spatial and intensity scales[2] over a 350 pc × 350 pc field-of-view. It is immediately clear that the brightest cluster candidates in M101 GHRs are more luminous than R136 and are most likely bona fide clusters. The nature of the cluster candidates fainter than $M_{\rm F547M} = -9.0$, marked in Figure 4.13, is less obvious. Some faint cluster candidates may be blue supergiants because they have sharp images and appear isolated, and the blue color excludes the possibility of post-core-collapse clusters; examples of these include NGC 5461-7, NGC 5462-20, and perhaps NGC 5471-13 and 14. Some faint cluster candidates may be OB associations because they appear extended without a sharp boundary; examples of these include NGC 5461-5, NGC 5462-13 and 15, and NGC 5471-10, 11, and 17.

---

[2] The green image of 30 Dor was taken in a similar but not identical wavelength band. The intensity scale of the 30 Dor image is selected to match that of the F547M images as much as possible so that objects with similar magnitudes appear similar in both F547M and green band images.

4.5.2 The Fraction of Massive Stars Formed in Clusters

It has been suggested that massive stars form preferentially in associations and clusters (Stahler et al., 2000, and references therein). Our *HST* WFPC2 images of the M101 GHRs show that several young R136-class clusters are superposed on discrete regions of unresolved stellar emission, e.g., clusters #8, #9, and #10 at the core of NGC 5461 and cluster #16 at the core of NGC 5471A. The unresolved stellar backgrounds are most likely star clouds that contain field stars and loosely assembled associations. The similarities in locations and colors suggest that the clusters and the background star clouds are formed from the same episode of star formation. It is then interesting to determine the fraction of massive stars that are formed in R136-class clusters in these regions. We have used two different methods to determine this fraction: one is based on the contribution of cluster light to the total light, and the other is based on a comparison between the ionization flux expected from the clusters and the ionizing flux required by the surrounding H II region.

We have selected four regions for this analysis: two in NGC 5461, one in NGC 5462, and one in NGC 5471. These regions are listed in Table 4.7, and their close-up F547M and Hα images are presented in Figure 4.14. The F547M images show that the clusters in these four regions are all superposed on discrete bright diffuse stellar backgrounds, and the Hα images show that all are at the cores of bright compact H II regions. We have measured the total light from these four regions in both F547M and F675W$'$ bands using the apertures marked on the F547M images in Figure 4.14 and described in column 3 of Table 4.7. The background, determined from the median of an annular region outside the H II region, has been subtracted, although it contributes to only 1–2% of the total light. For the clusters, we have applied aperture corrections of ~ -0.2 mag to our photometric measurements made with a $0\farcs2$-radius `apphot` aperture to account for the missing light. The cluster-to-total light ratios, $L_{\text{cluster}}/L_{\text{total}}$ given in columns 4 and 5 of Table 4.7, are in the range of 0.25–0.5; the uncertainties are dominated by the photometry and aperture corrections of the clusters, as they are superposed on bright local stellar background. The light ratios are slightly larger in the F547M band than in the F675W band, because the clusters are 0.1–0.2 mag bluer than their diffuse stellar background. This color difference can be caused by an age difference of a few Myr, assuming that the clusters and the underlying star clouds have the same initial mass function. As the precise ages are unknown, we cannot model the star clouds to determine their masses; therefore, the cluster-to-total light ratio can be considered only as an approximation of the fraction of massive stars formed in clusters. In the four regions we analyzed, about 25–50% of the massive stars are formed in R136-class clusters.

The Hα images in Figure 4.14 show that the H II regions around the clusters have rather well-defined boundaries where the surface brightness drops off sharply. Such morphology suggests that the H II regions are likely ionization-bounded, or optically thick to ionizing radiation. We have measured the Hα fluxes[3] of these four regions using the apertures marked on the Hα images in Figure 4.14 and described in column 6 of Table 4.7. The continuum-subtracted Hα images are used for the flux measurements, and extinction corrections are made. Assuming a 10^4 K optically thick H II region, the derived Hα luminosity, $L_{\mathrm{H}\alpha}$, can be used to determine the required ionizing luminosity, $Q(\mathrm{H}^0)$, through the relation

$$Q(\mathrm{H}^0) = 7.4 \times 10^{11}\ L_{\mathrm{H}\alpha} \text{ photons s}^{-1}, \tag{4.1}$$

where $L_{\mathrm{H}\alpha}$ is in units of ergs s^{-1}. The resultant ionizing luminosities (Q_{HII}) of the four regions are given in column 7 of Table 4.7.

The ionizing luminosity expected from the clusters at different ages can be calculated using the Starburst99 models. The ages of the clusters in the four selected regions are < 5 Myr, as indicated by the associated bright H II regions. Unfortunately, during the first 5 Myr a cluster's ionizing luminosity decreases rapidly, dropping from the maximum at ~ 1 Myr to a factor of 5–7 lower at 5 Myr (Leitherer et al., 1999); therefore, the uncertainty in cluster age directly propagates into the uncertainty in ionizing luminosity of a cluster. We have adopted a cluster age of 3 Myr and calculated the expected ionizing luminosities of the clusters (Q_{cluster}) and their ratios to those required by the surrounding H II regions. These results are given in columns 8 and 9 of Table 4.7. These ratios, 0.2–0.6, can be viewed as a very crude approximation of the fractions of massive stars formed in clusters. An interesting corollary of this result is that the ionizing luminosity, or Hα luminosity, of an H II region is not a sufficient diagnostic for the existence of SSCs because the majority of stars may reside outside clusters.

In the four regions of star formation we considered, the fraction of massive stars in clusters estimated from the cluster-to-total light ratio is, within the uncertainties, consistent with that estimated from the cluster-to-H II-region ionizing luminosity ratio – no more than about half of the massive stars are formed in the R136-class clusters. On the other hand, some R136-class clusters, such as #4 and #5 in NGC 5471D, are not superposed on a bright stellar background, and constitute the dominant components in their associated episode of star formation. The fraction of stars formed in clusters must cover a range, which varies according to the physical conditions of star formation.

---

[3] Owing to the ~ 300 km s^{-1} redshift of M101, two corrections need to be considered. First, the filter transmission of the red-shifted Hα line is $\sim 93\%$ of the peak transmission, thus the extracted Hα flux should be multiplied by a correction factor of 1.07. Second, the [N II]λ6548 line is red-shifted into the Hα bandpass at $\sim 91\%$ of the peak transmission and needs to be removed. The [N II] contamination, estimated from the [N II]/Hα ratios reported by Kennicutt & Garnett (1996), amounts to 1–3% of the Hα flux in most cases.

4.5.3 Interstellar Environments of the GHRs

We examine the distribution of interstellar molecular clouds and H I gas in the three M101 GHRs in order to gain insight on the cluster formation process. Molecular CO observations of these GHRs have been made by Giannakopoulou-Creighton et al. (1999) using both single-dish telescopes and interferometers. NGC 5461 has the strongest CO emission among the three GHRs, and its CO peaks appear concentrated toward the peaks of the Hα emission (see Figure 4 in Giannakopoulou-Creighton et al., 1999), where the massive clusters are located. The CO emission toward NGC 5462 is detected in single-dish observations but not in interferometric observations, indicating that the molecular gas is distributed over a scale larger than the synthesized beam, $\sim 3''$. No CO emission is detected in NGC 5471, which may be attributed to its low metallicity. In the two GHRs where CO is detected, the distribution of molecular clouds is similar to that of clusters: concentrated in NGC 5461 and distributed in NGC 5462.

The distribution of H I gas in M101 and its relation with ionized gas have been reported by Smith et al. (2000, see their Figures 1–2). Their H I map shows that NGC 5461 and NGC 5462 are in the same spiral arm. Assuming a trailing arm, the offsets of H I ridge downstream from the stars in NGC 5461 and NGC 5462 are consistent with the expectations of star formation triggered by density waves (Roberts, 1969). NGC 5471 has a concentration of H I gas but the large-scale distribution of H I show a complex inter-arm structure, which may have resulted from tidal interactions during the last 10^9 yr (Waller et al., 1997, and references therein). As H I gas can be produced by photodissociation of the natal molecular clouds (Allen et al., 1985, 1986; Smith et al., 2000), converted to H II by photoionization, and dispersed by fast stellar winds and supernova explosions, the distribution of H I does not provide adequately pertinent information about the cluster formation.

To study the physical conditions for cluster formation, it is necessary to examine the interstellar environment of the youngest clusters before the interstellar conditions have been altered by stellar energy feedback. The embedded young clusters that are observable in the infrared but not yet in the optical wavelengths (e.g., Kobulnicky & Johnson, 1999; Turner et al., 2000; Johnson & Kobulnicky, 2003) provide promising locations to study the physical conditions of cluster formation.

4.5.4 Cluster Luminosity Function

The luminosity functions (LFs) of young compact clusters have been studied in various types of galaxies with different star formation rates as a means to gain insight into the cluster formation process. To first order, the measured LFs for young compact cluster systems in merging or starburst galaxies are remarkably universal, and can be approximated by a power-law of the form $dN(L)/dL \propto L^{\alpha}$, with the exponent $\alpha \approx -2 \pm 0.2$

(see Whitmore, 2003, and references therein). The cluster LFs for a sample of nearby non-starburst spiral galaxies also show similar α, -2.0 to -2.4 (Larsen, 2002). It has been suggested that this roughly universal LF is the result of fractal structure in turbulent gas (Elmegreen & Efremov, 1997). Since the three M101 GHRs show different age and spatial distributions of clusters, it is interesting to intercompare their cluster LFs and see if they also follow the universal cluster LFs.

The LFs of clusters in NGC 5461, NGC 5462, and NGC 5471 are presented in Figure 4.15. These LFs are constructed using raw $M_{\rm F547M}$ (without extinction correction). No completeness correction to the LFs is needed because the cutoff of our sample at the faint end, $m_{\rm F547M} \leq 21.3$, is much brighter than the detection limit, $m_{\rm F547M} \sim 25.5$. Note however that the two faintest bins, $M_{\rm F547M} = -8.0$ to -9.0, should be viewed with caution, as some of the "clusters" may be spurious as discussed in §4.5.1. The number of clusters in each GHR is modest, so we have also constructed a combined cluster LF of the three GHRs, shown in the bottom panel of Figure 4.15. We have carried out linear least-squares fits to the logarithmic LFs of clusters for the three GHRs individually and combined. The logarithmic LFs of clusters in the individual GHRs appear to have different slopes; the best-fit slopes for NGC 5461, NGC 5462, and NGC 5471 are -1.5 ± 0.3, -3.0 ± 0.2, and -1.9 ± 0.4, respectively. The logarithmic LF of clusters in all three GHRs has a best-fit slope of -2.3 ± 0.1.

Compared with the universal cluster LFs, NGC 5461 and NGC 5471 are on the flatter side, and NGC 5462 is on the steeper side. The small difference between NGC 5461 and NGC 5471 is not statistically significant, as each has only a small number of clusters and the numbers of clusters in the brightest bins are only 1–2. On the other hand, it may be statistically significant that NGC 5462 has a much steeper LF than NGC 5461 and NGC 5471, or NGC 5462 has a larger proportion of low-mass clusters. It is possible that the slope of a cluster LF varies according to the interstellar environment at the time when clusters were formed. As discussed in §4.5.3, the current molecular environments of NGC 5461 and NGC 5462 are quite different, with molecular CO highly concentrated in NGC 5461 and diffuse in NGC 5462. If the current environments reflect the conditions when the clusters were formed, the clusters in NGC 5462 would have been formed in a lower-pressure, lower-concentration interstellar environment. The association between a steep cluster LF and a low-pressure, low-concentration star formation condition is consistent with the previously suggested hypothesis that massive clusters are formed in high-pressure, high-concentration molecular clouds.

The cluster LF for NGC 5461, NGC 5462, and NGC 5471 combined has an α within the range of the universal value, -2 to -2.4. If clusters in spiral or starburst galaxies are formed under conditions similar to NGC 5461 and NGC 5462 in random proportions, the cluster LFs should show a larger range of α. The scarcity of cluster LFs with α steeper than -2.5 might be an observational effect to some extent. Surveys of clusters in galaxies preferentially detect the most luminous clusters that are likely formed in high-pressure environments and follow an LF similar to those of NGC 5461 and NGC 5471; therefore, the cluster LF of a galaxy would be biased toward $\alpha = -2$.

4.5.5 Evolutionary Aspects of the Clusters

The cluster mass, age, and size distribution of a cluster system may be used to investigate the dynamic evolution of clusters. Recent studies of rich clusters in the LMC have shown that the spread in core radius increases with cluster age, suggesting that all clusters were formed with small core radii but subsequently some experienced core expansion while others did not (Elson et al., 1989; Mackey & Gilmore, 2003). It would be interesting to examine the clusters in M101 GHRs to see whether they follow the same core radius-age relation.

The mass, age, and core radius of the LMC clusters have been derived by Mackey & Gilmore (2003), using the Fioc & Rocca-Volmerange (1997) population synthesis code, the Kroupa et al. (1993) IMF slope, and a stellar mass range of 0.1–120 $M_\odot$. To compare the M101 clusters with the LMC clusters, we have followed the Mackey & Gilmore (2003) method and re-estimated the masses of M101 clusters, using the same code, IMF slope, and stellar mass range. The new cluster mass estimates are $\sim$ 2–3 times as high as the cluster masses estimated earlier in this paper, owing to the addition of stars in the mass range of 0.1–1 $M_\odot$. The M101 clusters are not sufficiently resolved for measurements of their core radii (r_c); therefore, we have adopted the relation $r_c \sim 0.35 R_{\rm eff}$ derived from a King profile with a concentration parameter of $c = 1.5$, a median value for LMC clusters (Elson et al., 1987). The core radii of M101 clusters thus estimated are 0.25–1 pc, and may be uncertain by up to a factor of 2, if its concentration parameter spans the same range as that in the LMC clusters.

To compare the M101 clusters with the LMC clusters, we present a 3-D diagram of cluster mass, age, and core radius in Figure 4.16. The data of the LMC clusters are adopted from Mackey & Gilmore (2003). The M101 clusters are plotted in open rhombuses, while the LMC clusters are plotted in filled ellipses, with the R136 cluster in a larger ellipse for easy identification. The M101 cluster masses were estimated using 7-pc-radius apertures, so we repeated Mackey & Gilmore's derivation of the mass of R136 using this larger aperture and obtained a mass that is 40% higher, shown as a large open ellipse in Figure 4.16. While the LMC clusters span a large age range and show an increasing spread in core radii with the cluster age, the M101 clusters we analyzed are all young and small, sharing a similar parameter space with the R136 cluster. Among the small number of M101 clusters with size measurements, the younger clusters are generally smaller, but the accuracy of the size measurements is too limited by the linear resolution for definitive conclusions.

Finally, we discuss the disruption time of our M101 clusters and investigate whether dynamical evolution has caused a significant mass change in these clusters. The disruption time can be assessed empirically from the break in slopes of the logarithmic age distribution of clusters (Boutloukos & Lamers, 2003), or from comparisons with N-body simulations (Baumgardt & Makino, 2003). Recent studies using the empirical method have shown that the disruption time for a 10^4 $M_\odot$ cluster varies greatly among galaxies, from 10^7 to 10^{10} yr, with the shortest being ~30–40 Myr in M82 and at 1–3 kpc from the nucleus of M51 (Boutloukos & Lamers, 2003; de Grijs et al., 2003). Our M101 clusters in GHRs are apparently younger than these disruption timescales. Thus we determine the disruption time, $T_{\rm dis}$, following the simulations of Baumgardt & Makino (2003):

$$\frac{T_{\rm dis}}{\rm Myr} = \beta \left[\frac{N}{\ln(\gamma N)}\right]^x \frac{R_{\rm G}}{\rm kpc} \left(\frac{V_{\rm G}}{220\ {\rm km\ s^{-1}}}\right)^{-1} \qquad (4.2)$$

where $R_{\rm G}$ is the galactocentric radius, $V_{\rm G}$ is the circular velocity in a galaxy, N is the number of stars in a cluster, $\beta \sim 1$–2, $\gamma = 0.02$, and $x \sim 0.8$. For a cluster with a Salpeter mass function and a stellar mass range of 1–100 $M_\odot$, the average mass of a star is 3.09 $M_\odot$ and the number of stars is N = cluster mass/(3.09 $M_\odot$). NGC 5461 and NGC 5462 have $R_{\rm G} \sim 10$ kpc and $V_{\rm G} = 185$ km s^{-1}, and NGC 5471 has $R_{\rm G} \sim 25$ kpc and $V_{\rm G} = 195$ km s^{-1} (Roberts & Rots, 1973). A 10^4 $M_\odot$ cluster in NGC 5461/NGC 5462 or NGC 5471 would have disruption times of 2.4–4.8 $\times 10^9$ and 5.8–11.6 $\times 10^9$ yr, respectively. The real disruption time must be shorter because the above estimates do not take into account processes that are important in disrupting clusters in GHRs, i.e., interactions with other clusters and with giant molecular clouds. In cases where massive clusters are concentrated in a small volume, such as the core of NGC 5461, cluster merger is a more important dynamic process and operates in a much shorter timescale than tidal disruption (Bonnell et al., 2003). Future simulations of dynamical evolution of clusters in GHRs using realistic conditions are needed.

4.6 Summary

GHRs contains high concentrations of massive stars; thus, they provide an excellent laboratory to study modes of massive star formation and possible sites to form globular clusters. We have selected three very luminous but morphologically different GHRs in M101, NGC 5461, NGC 5462, and NGC 5471, to determine their cluster content in order to understand cluster formation in different environments. We have obtained *HST* WFPC2 images of these GHRs with the F547M and F675W continuum filters and the F656N Hα filter. The continuum images are used to identify cluster candidates in each GHR and to carry out photometric measurements, and the Hα images are used to examine the distribution of interstellar gas and to determine the ionizing flux requirement.

We have used the Starburst99 (Leitherer et al., 1999) and BC03 (Bruzual & Charlot, 2003) population synthesis models to compute the colors and magnitudes of clusters of different ages and masses. The colors of a cluster are dependent on its age; however, our two continuum passbands are not blue enough to be sensitive to young massive stars for age determination. Therefore, we use the distribution of ionized interstellar gas to estimate the approximate cluster ages, then compare the measured colors and magnitudes of cluster candidates to the synthetic evolutionary tracks to determine their masses. To avoid confusion by luminous single supergiants, only cluster candidates more luminous than $M_{\rm F547M} = -9.0$ are analyzed for their masses.

NGC 5461 is dominated by a very luminous core, and has been suggested as a likely host of SSCs (Kennicutt & Chu, 1988; Luridiana & Peimbert, 2001). Our observations show that the core of NGC 5461 contains three R136-class clusters superposed on a bright stellar background in a small region ~32 pc across. It is possible that the three R136-class clusters will dynamically interact and merge into an SSC. If NGC 5461 were at a distance $\gtrsim$ 20 Mpc, the clusters at its core would appear as a single cluster, and the total light would be $M_{\rm F547M} = -13.0$, corresponding to a mass of $\sim 10^5$ $M_\odot$, reaching those of SSCs. It is possible that some of the previously reported SSCs at large distances are actually made up by tight groups of R136-class clusters similar to those in NGC 5461.

NGC 5462 consists of numerous loosely-distributed H II regions that are individually much fainter than 30 Dor. Its clusters also show a loose distribution across the GHR. NGC 5462 has the largest number of clusters among the three GHRs studied, but most of the clusters are older than 10 Myr and fainter than $M_{\rm F547M} = -9.0$.

NGC 5471 contains multiple bright H II regions, some of which are comparable to 30 Dor. A large number of cluster candidates are identified in NGC 5471; the majority of the clusters are fainter than $M_{\rm F547M} = -9.0$ and they are in bright H II regions. The mass determination for clusters in NGC 5471 is problematic because the observed cluster colors are bluer than those spanned by the synthetic cluster evolutionary tracks for $Z = 0.2Z_\odot$, possibly as a result of uncertainties in stellar evolution models at low metallicities. The cluster masses are thus estimated from the magnitudes alone and may be subject to large errors.

The most massive clusters in the three GHRs are in the mass range of $\sim$ 1–3 $\times 10^4$ $M_\odot$, similar to R136. Two clusters in NGC 5471 might be more massive as they are not surrounded by H II regions and are each as luminous as R136; these two may be the most massive clusters in the three GHRs studied. No SSCs are present in any of the three GHRs. We have also estimated the sizes of some clusters on their PC images, using the routine developed by Larsen (1999). The effective radii of these clusters are in the range of 0.7–2.9 pc, $\sim$ 1–3 times that of R136 (Mackey & Gilmore, 2003).

To understand the makeup of the faint cluster candidates, we have simulated WFPC2 images of 30 Dor and NGC 604 at the distance of M101. We find that single supergiants similar to R131 and OB associations as those in NGC 604 may contribute to the population of faint clusters ($M_{\rm F547M} > -9.0$) in distant galaxies, while clusters similar to Hodge 301 or OB associations similar to LH 99 will be too faint or too extended to be identified as clusters even in M101.

The three M101 GHRs show different cluster LFs. The cluster LFs of spiral galaxies can be described by a power-law with the exponent α in the range of -2.0 to -2.4 (Larsen, 2002). We find that the cluster LFs of NGC 5461 and NGC 5471 are on the flatter side of the range, but the number of clusters is small in each GHR. NGC 5462 has the largest number of clusters and its cluster LF is significantly steeper, with $\alpha = -3.0 \pm 0.2$. It is possible that the clusters in NGC 5462 were formed in a low-pressure, low-concentration interstellar environment. The combined cluster LF of the three GHRs has an α of -2.3 ± 0.1, well within the range for those of spiral galaxies. The universality of cluster LFs may be a statistical result from a cluster population with an observational bias toward the most luminous clusters.

The distribution of molecular clouds is concentrated in NGC 5461 and diffuse in NGC 5462, similar to the spatial distribution of their clusters. The diffuse interstellar environment and the larger proportion of low-mass clusters (steep cluster LF) of NGC 5462 qualitatively support the hypothesis that massive clusters are formed in high-pressure, high-concentration interstellar medium.

We have estimated the fraction of massive stars formed in clusters using (1) clusters' contribution to the total stellar continuum, and (2) comparison between the ionizing flux expected from the clusters and the ionizing flux required by the associated H II region. Both methods show that $\lesssim 50\%$ of massive stars are formed in R136-class clusters. Consequently, the Hα luminosity of an H II region does not provide a sufficient diagnostic for the existence of SSCs.

4.7 Figures and Tables

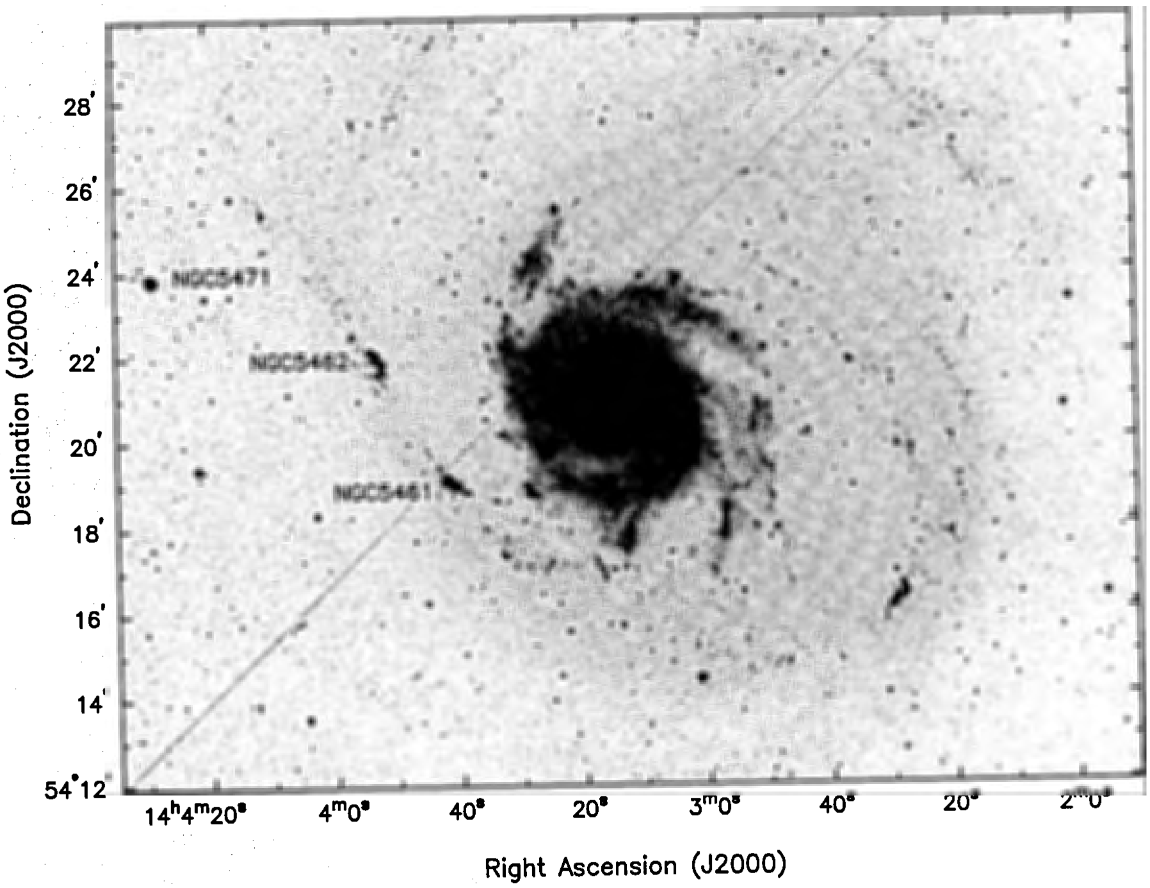

Figure 4.1 The POSS-II red image of M101 from the Digitized Sky Survey. The three luminous GHRs studied in this paper, NGC 5461, NGC 5462, and NGC 5471, are marked.

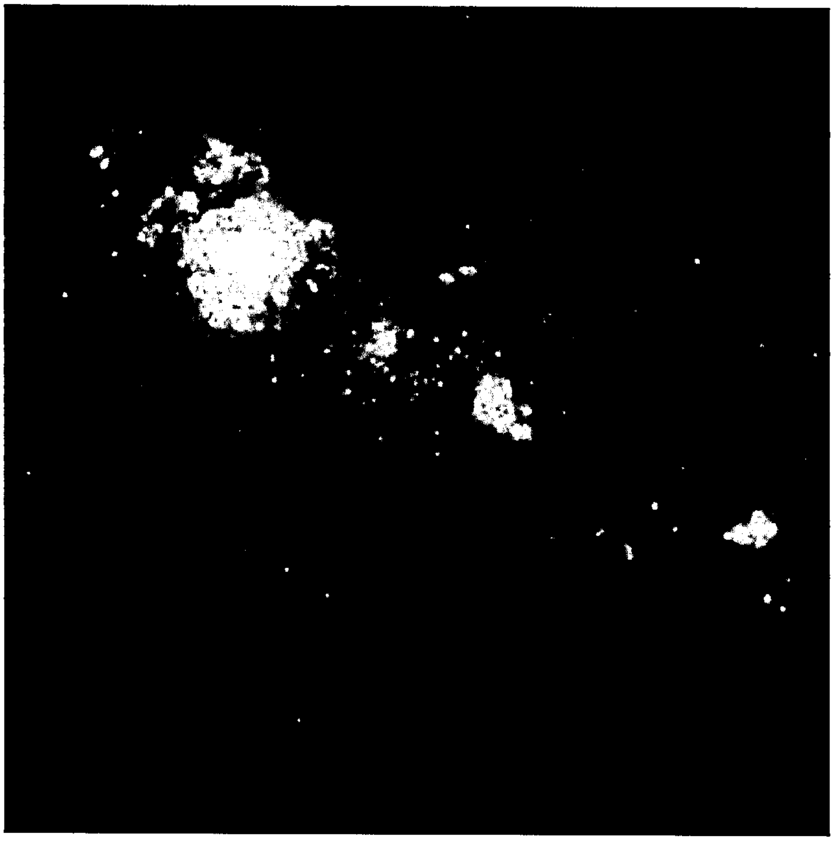

Figure 4.2 Color composite of *HST* WFPC2 images of NGC 5461, with F547M in blue, F675W in green, and Hα in red. North is up and east to the left. The field-of-view is $45'' \times 45''$, or 1.6 kpc × 1.6 kpc.

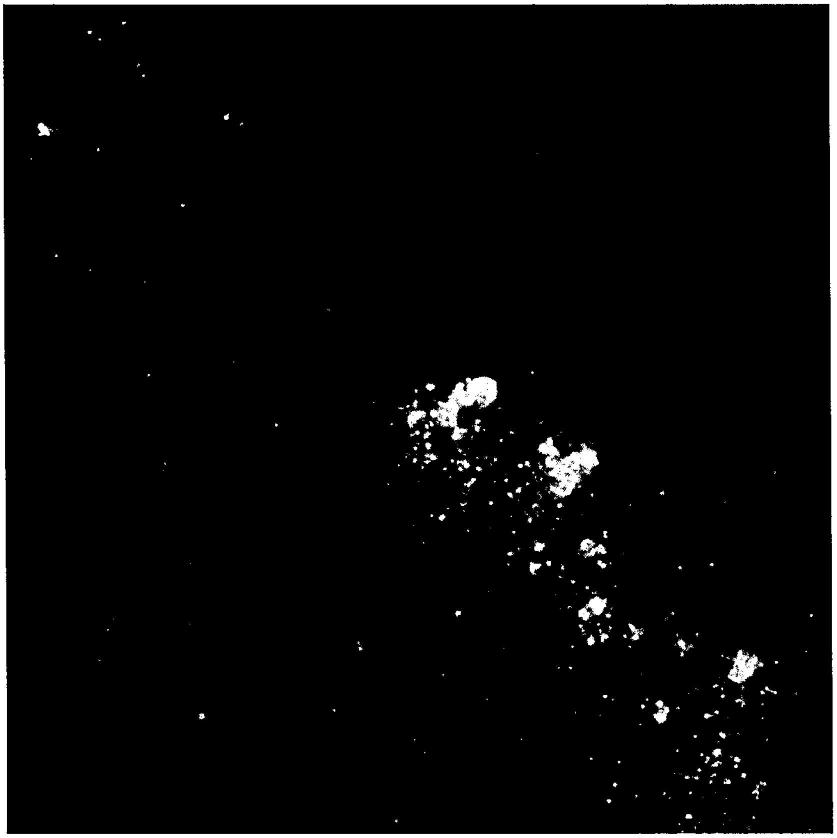

Figure 4.3 Color composite of *HST* WFPC2 images of NGC 5462, with F547M in blue, F675W in green, and Hα in red. North is up and east to the left. The field-of-view is $56'' \times 56''$, or 2.0 kpc × 2.0 kpc.

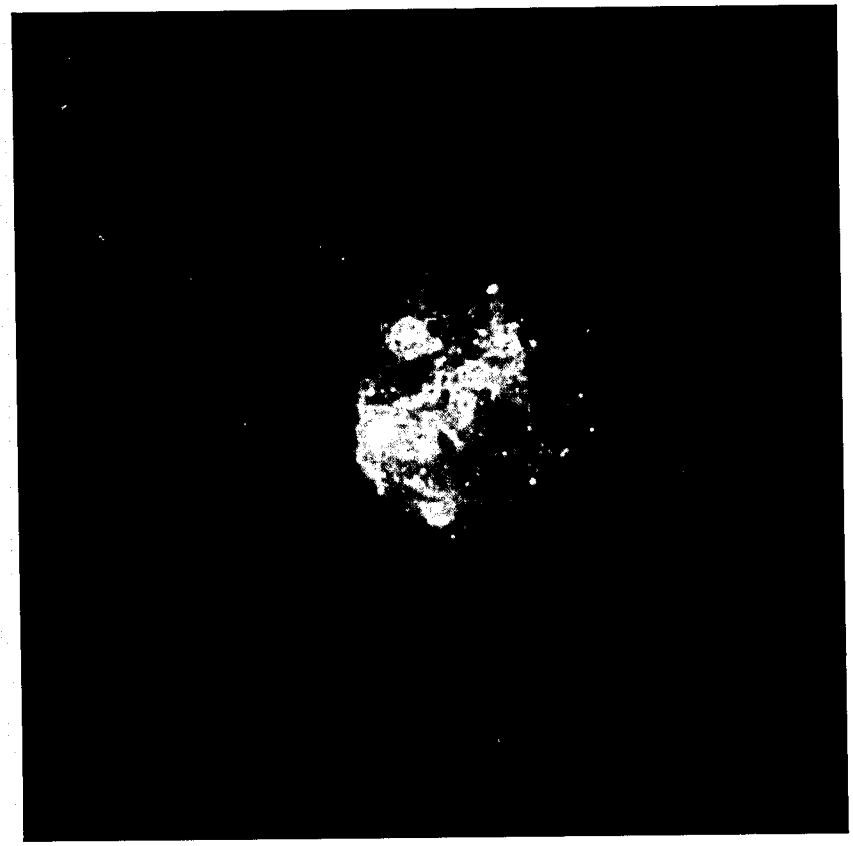

Figure 4.4 Color composite of *HST* WFPC2 images of NGC 5471, with F547M in blue, F675W in green, and Hα in red. North is up and east to the left. The field-of-view is $51'' \times 51''$, or 1.8 kpc × 1.8 kpc.

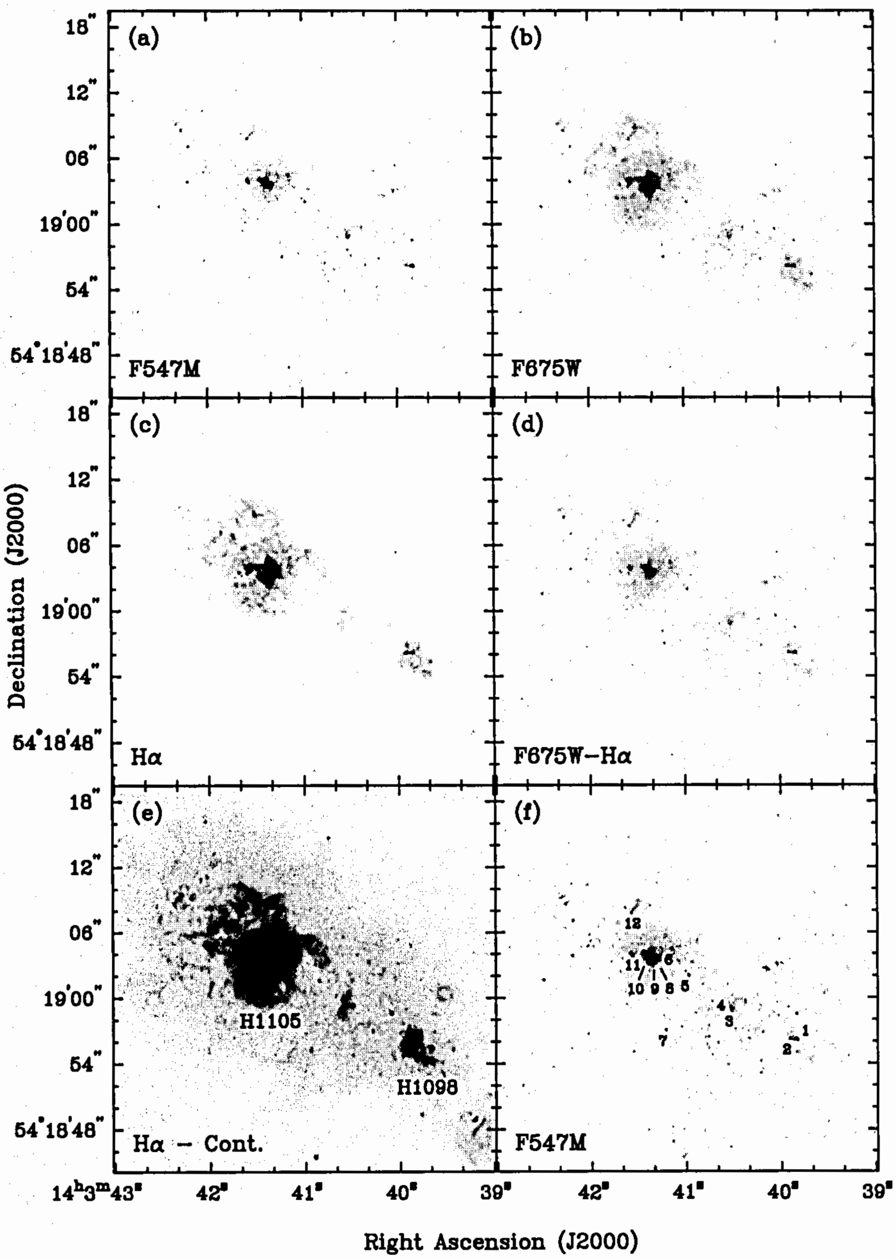

Figure 4.5 *HST* WFPC2 images of the main body of NGC 5461 in (a) F547M, (b) F675W, (c) Hα, (d) Hα-subtracted F675W, (e) continuum-subtracted Hα, and (f) F547M bands. Note that this field-of-view is smaller than that shown in Figure 4.2. The Hα images (c) and (e) are presented in different stretches to show bright and faint features, and similarly the F547M images (a) and (f) to show bright and faint stars/clusters. The two brightest H II regions from Hodge et al. (1990) are marked in (e), and cluster candidates are marked in (f).

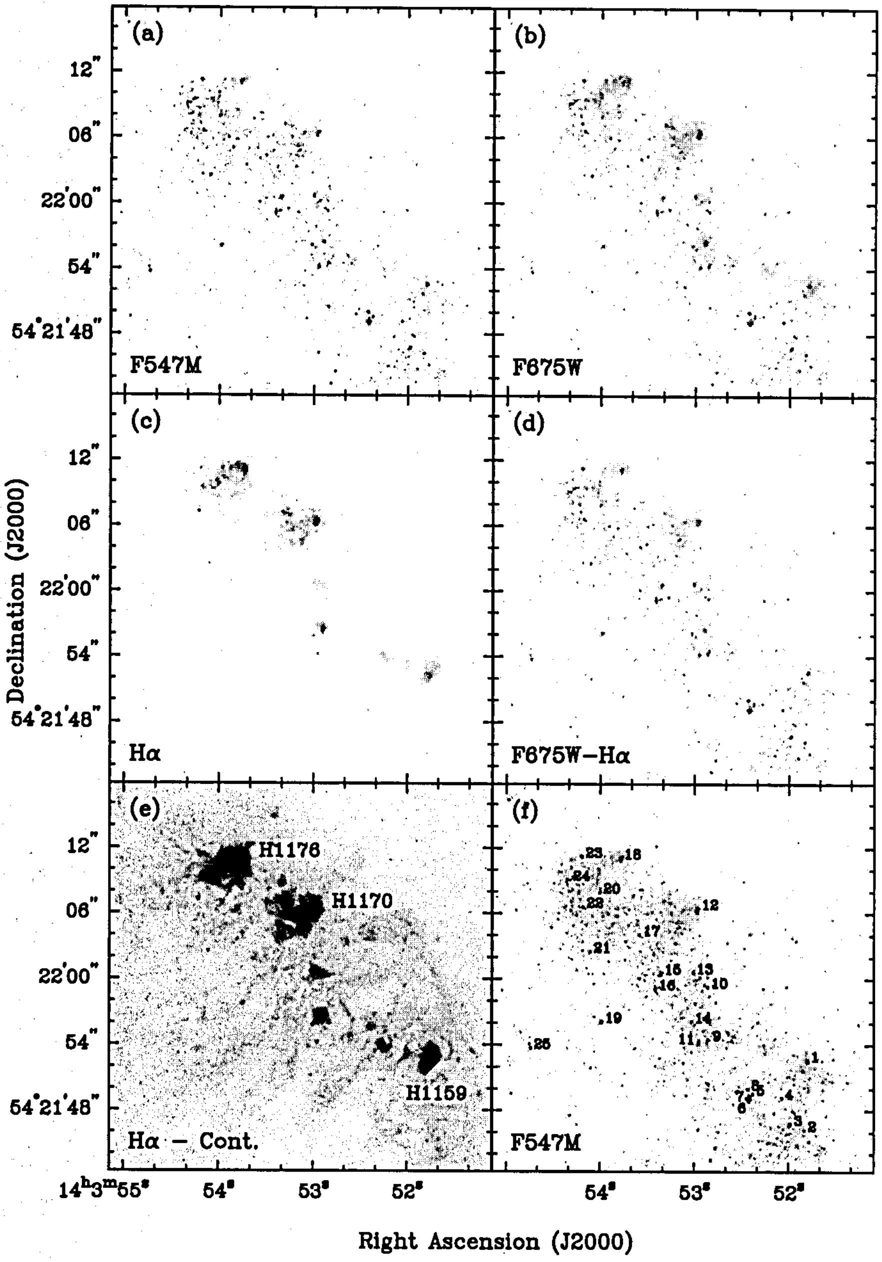

Figure 4.6 *HST* WFPC2 images of the main body of NGC 5462, displayed in a format identical to that of Figure 4.5. Note that this field-of-view is smaller than that shown in Figure 4.3. The three brightest H II regions from Hodge et al. (1990) are marked in (e), and cluster candidates are marked in (f).

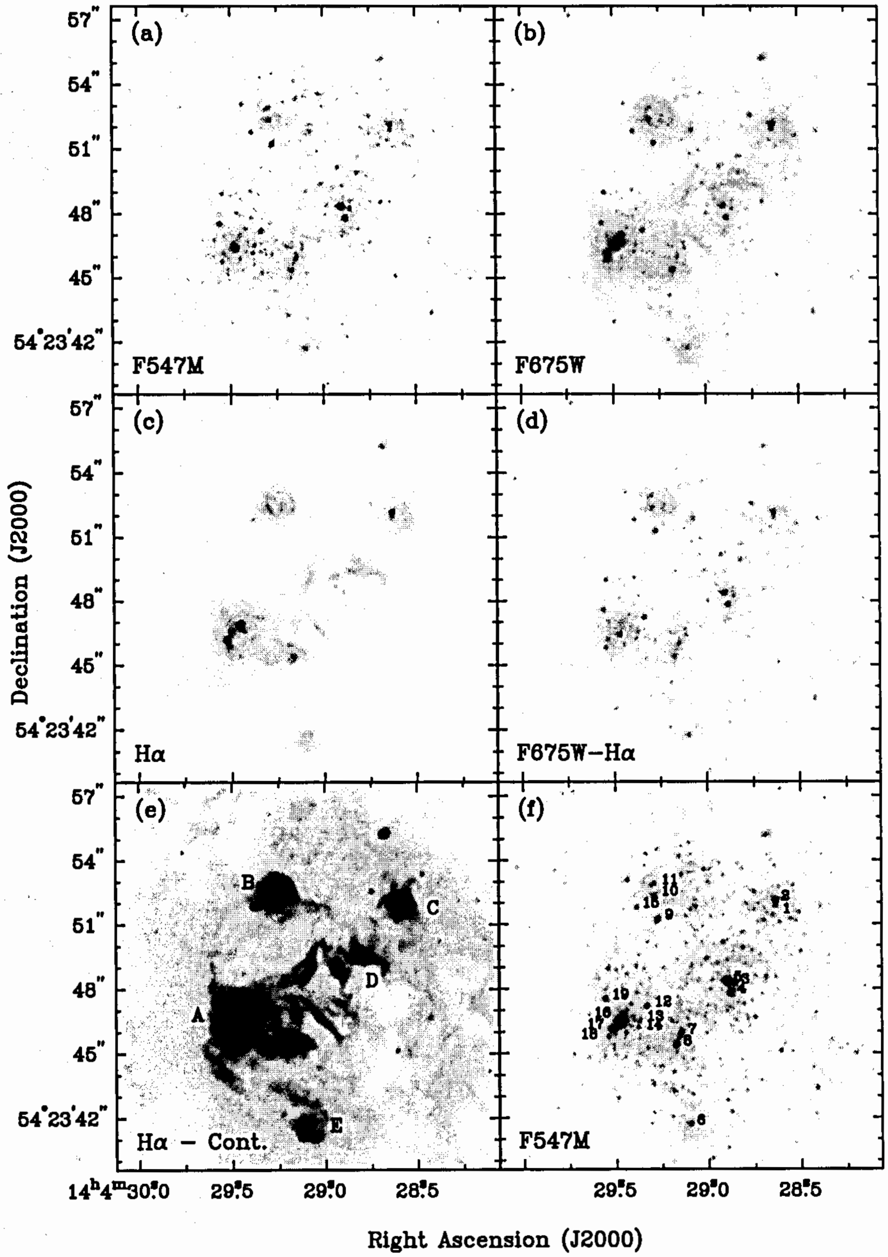

Figure 4.7 *HST* WFPC2 images of NGC 5471, displayed in a format identical to that of Figure 4.5. Note that this field-of-view is smaller than that shown in Figure 4.4. The five brightest components from Skillman (1985) are marked in (e), and cluster candidates are marked in (f).

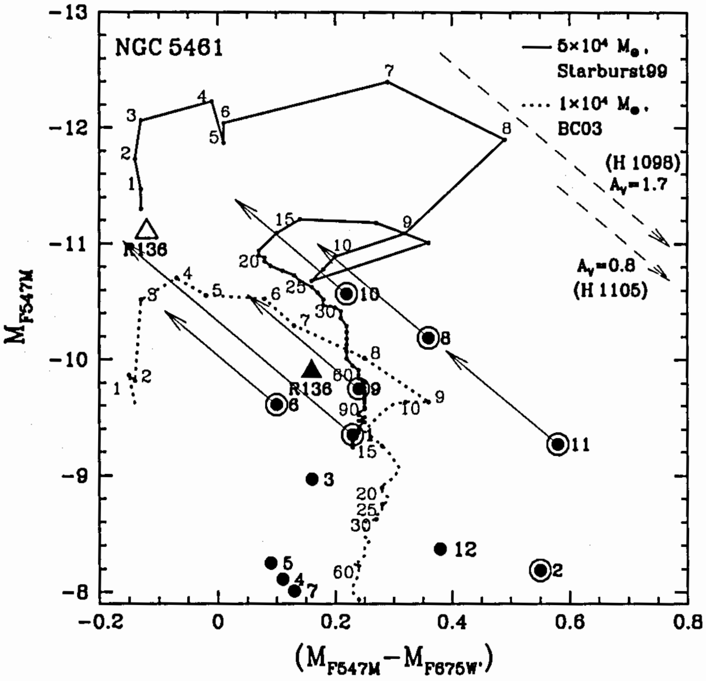

Figure 4.8 $M_{\rm F547M}$ versus $(M_{\rm F547M} - M_{\rm F675W'})$ diagram of cluster candidates in NGC 5461. Observations of the clusters are plotted in filled circles. Additional circles are draw around clusters that are embedded in bright H II regions. Evolutionary tracks generated from Starburst99 and BC03 for a Salpeter initial mass function and a metallicity of $Z = 1\ Z_\odot$ are plotted in solid and dotted curves, respectively. Ages in Myr are marked along the evolutionary tracks. To avoid crowding, the Starburst99 evolutionary track is shown for a cluster mass of 5×10^4 M$_\odot$ and the BC03 track for 1×10^4 M$_\odot$. The reddening vectors of associated H II regions are plotted in dashed arrows, and the possible dereddening vectors are marked with solid arrows for clusters brighter than $M_{\rm F547M} = -9.0$. The R136 cluster is plotted as a reference point: reddened R136 in a filled triangle and dereddened R136 in an open triangle.

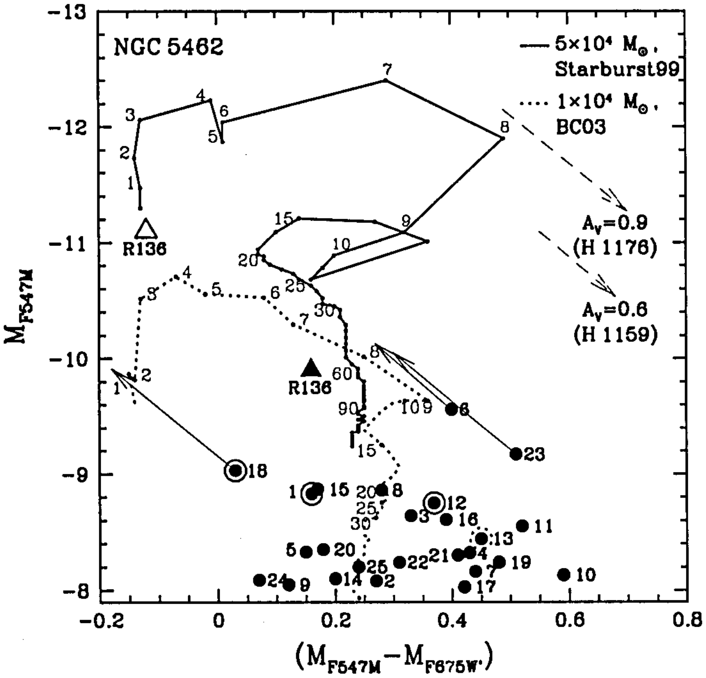

Figure 4.9 M_{F547M} versus ($M_{\mathrm{F547M}} - M_{\mathrm{F675W'}}$) diagram of cluster candidates in NGC 5462. Symbols are the same as in Figure 4.8 with the addition of a dashed circle for the cluster candidate in an interstellar shell. The evolutionary tracks are the same as in Figure 4.8.

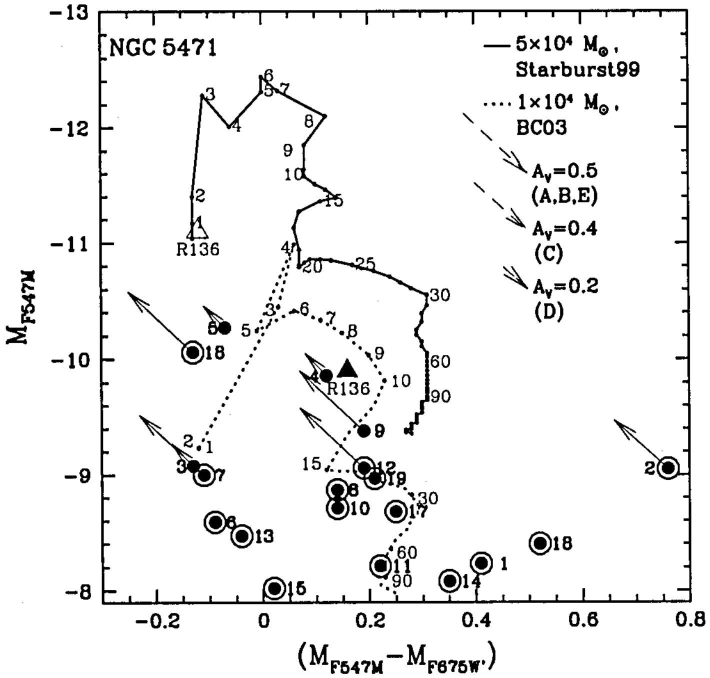

Figure 4.10 M_{F547M} versus ($M_{\mathrm{F547M}} - M_{\mathrm{F675W'}}$) diagram of cluster candidates in NGC 5471. Symbols are the same as in Figure 4.8. The evolutionary tracks are generated from population synthesis models using the same parameters as those generated for NGC 5461 and NGC 5462, but with a metallicity of $Z = 0.2\ Z_{\odot}$.

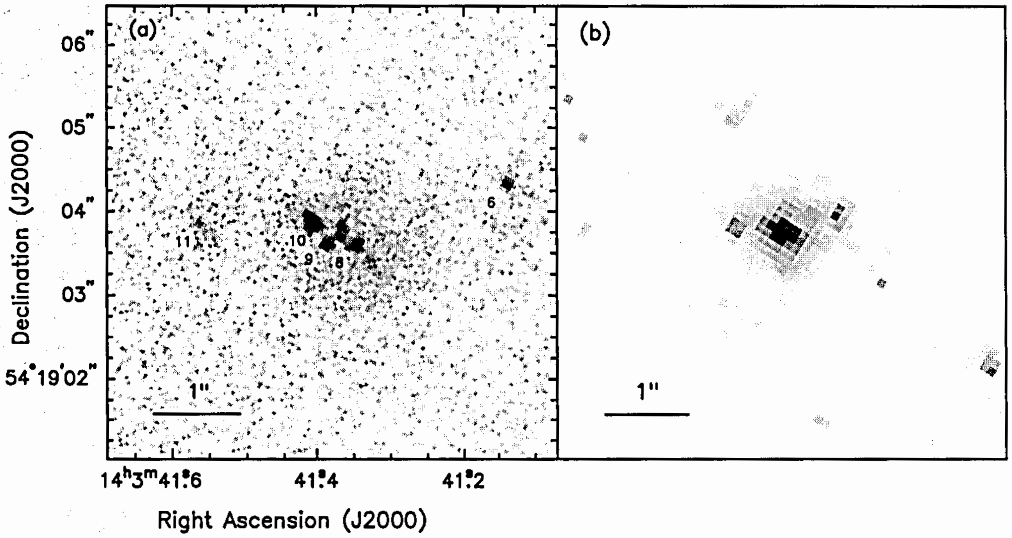

Figure 4.11 (a) *HST* WFPC2 PC image of the clusters in the core of NGC 5461 (i.e., H 1105) in the F547M band. The cluster numbers given in Figure 4.5 are again marked. (b) Binned *HST* WFPC2 WFC image in the F547M band for the same region to simulate a WFC image at 20 Mpc. At such a large distance, the three clusters at the core of NGC 5461 are no longer distinguishable from a single super-star cluster.

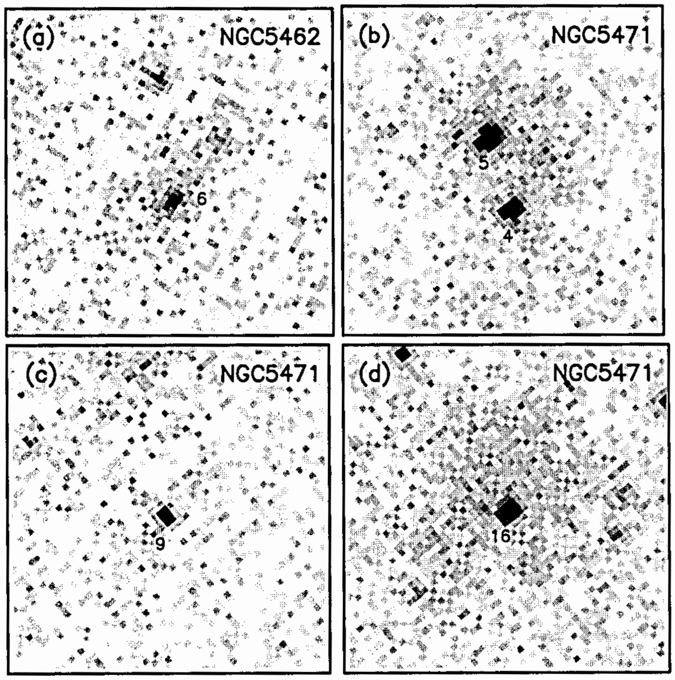

Figure 4.12 *HST* WFPC2 PC images of the brightest clusters in NGC 5462 and NGC 5471 for which cluster sizes were measured: (a) NGC 5462-6, (b) NGC 5471-4 & -5, (c) NGC 5471-9, and (d) NGC 5471-16. The pixel size of a PC image is 0.″0455, corresponding to a linear size of 1.6 pc in M101. The field-of-view of each image is 2.″4 × 2.″4.

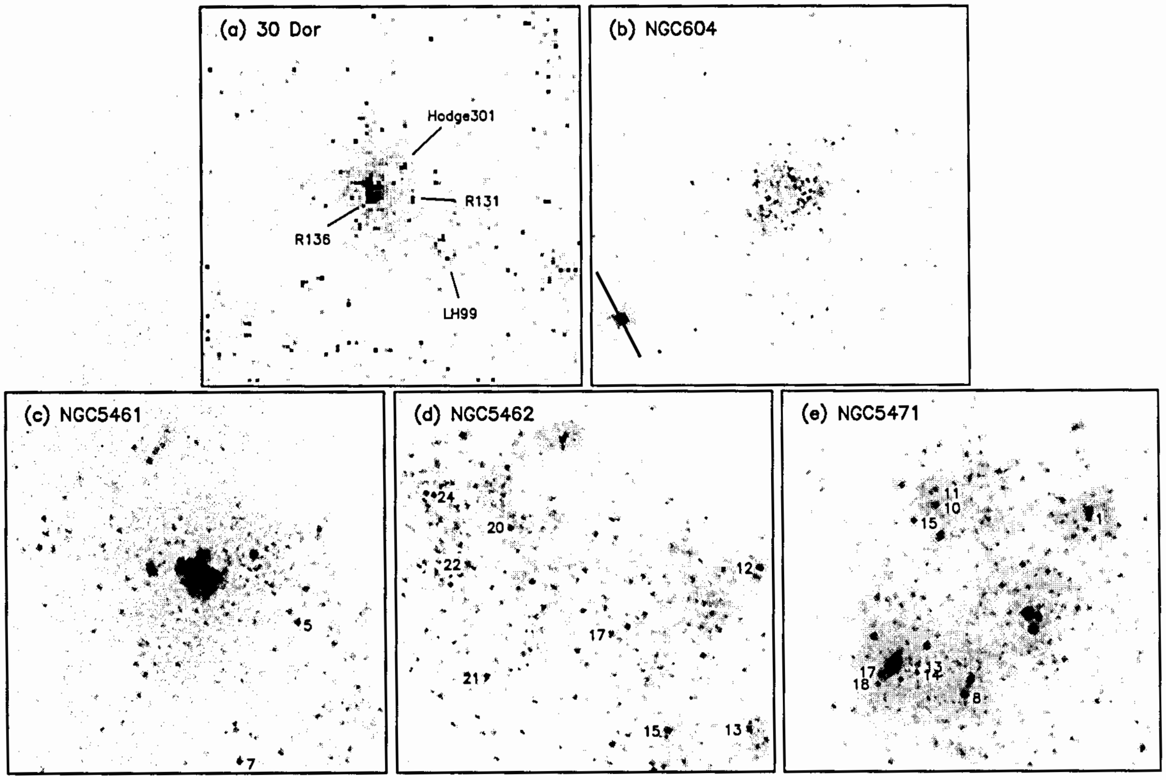

Figure 4.13 Comparison of binned continuum images of 30 Dor and NGC 604 with M101 GHRs. (a) Binned MCELS green band image of 30 Dor and (b) binned *HST* WFPC2 F547M images of NGC 604 to simulate WFPC2 images of 30 Dor and NGC 604 at the distance of M101. (c)–(e) *HST* WFPC2 F547M images of M101 GHRs NGC 5461, NGC 5462, and NGC 5471. The cluster candidates with $M_{\mathrm{F547M}} > -9.0$ are marked. All images have the same linear field-of-view, 350 pc × 350 pc. The four F547M images are displayed with the same intensity scale, while the green band image of 30 Dor is displayed with an intensity scale matching that of the F547M images as much as possible.

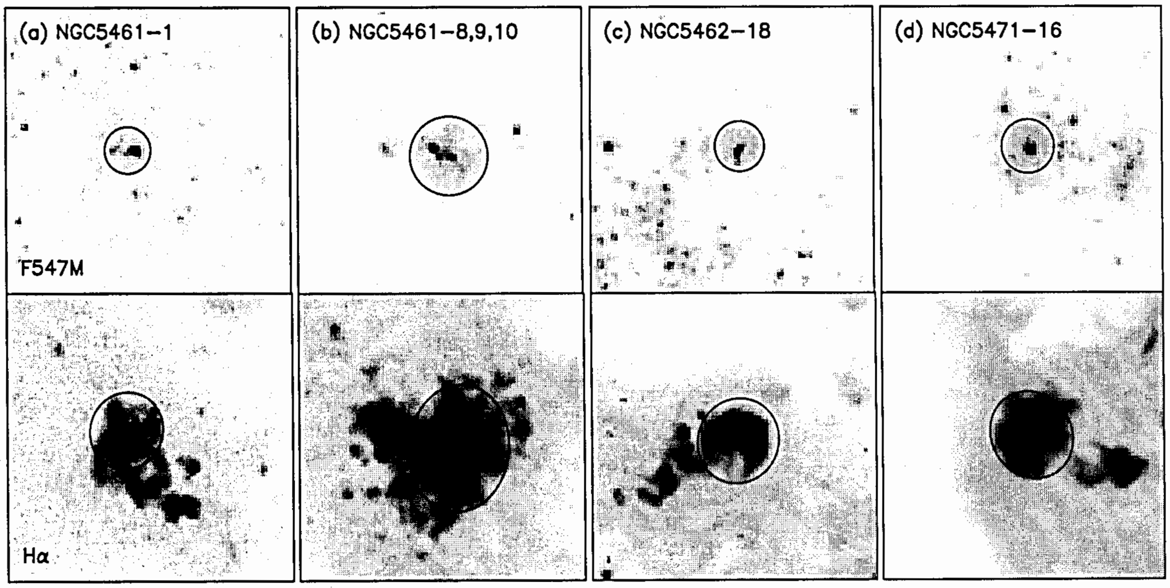

Figure 4.14 *HST* WFPC2 images of four regions with R136-class clusters coexistent with bright diffuse stellar background in the F547M band (upper panels) and Hα band (bottom panels): (a) NGC 5461-1, (b) NGC 5461-8, 9, 10, (c) NGC 5462-18, and (d) NGC 5471-16. Circles in the F547M images mark the apertures used to measure the total stellar continuum emission of each region, and ellipses in the Hα images mark the apertures used to measure the Hα fluxes of the associated H II region. The field-of-view of each image is 8″ × 8″.

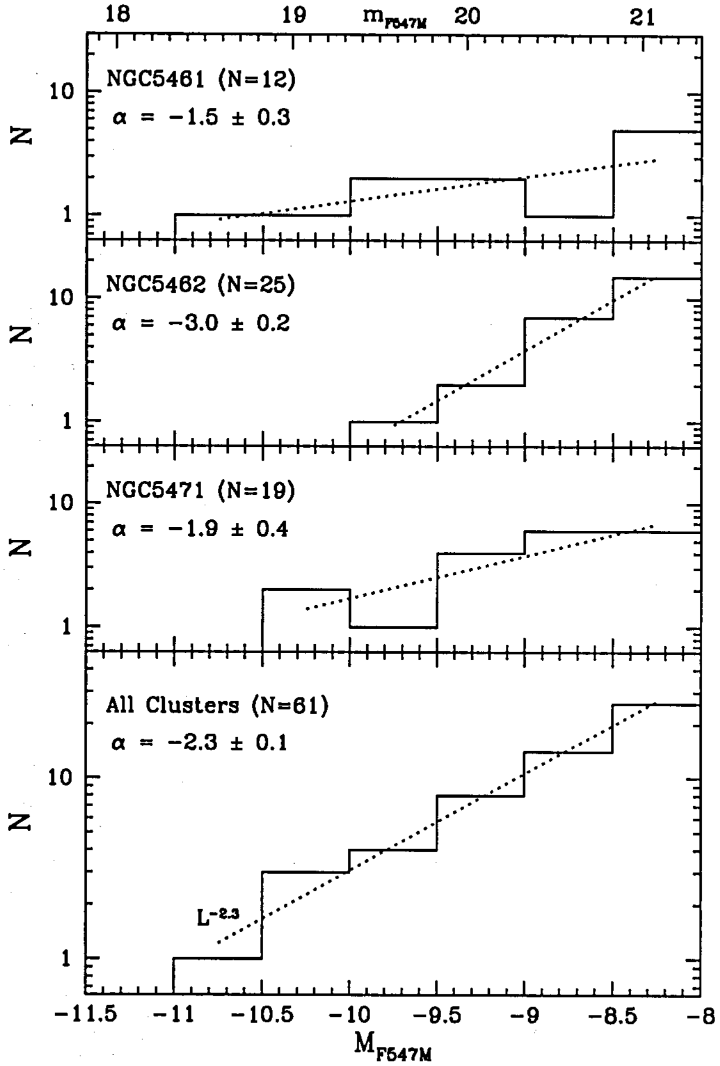

Figure 4.15 $M_{\rm F547M}$ LFs of candidate clusters in NGC 5461, NGC 5462, NGC 5471, and of the combined sample of all three GHRs. Solid lines are cluster LFs and dotted lines are power-law fits to these LFs. The best-fit α value and the number of cluster candidates are labeled in the upper left corner of each panel.

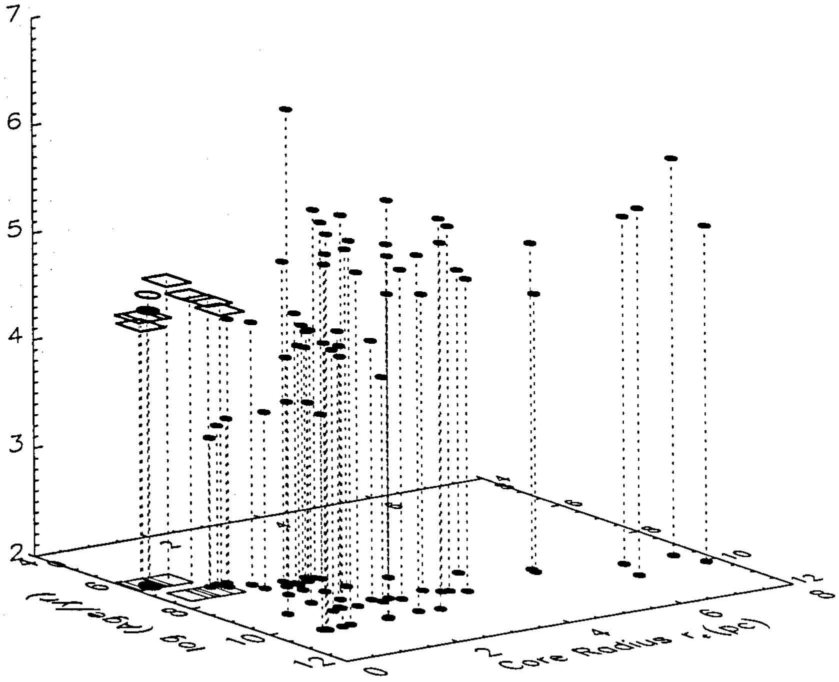

Figure 4.16 A 3-D diagram of age, core radius, and mass of clusters in the LMC and M101. The M101 clusters are shown as open rhombuses, while the LMC clusters (Mackey & Gilmore, 2003) are shown as filled ellipses. The R136 cluster is shown as a larger filled ellipse and open ellipse for the mass estimates from Mackey & Gilmore (2003) and this study, respectively.

Table 4.1. Properties of the Three Luminous GHRs in M101 and 30 Dor in the LMC

	NGC 5461	NGC 5462	NGC 5471	30 Dor
Angular Size	$40'' \times 25''$	$48'' \times 33''$	$17'' \times 17''$	$20' \times 20'$
Linear Size[a](pc)	1400×875	1680×1150	600×600	290×290
$L_{\mathrm{H}\alpha}$[b](ergs s^{-1})	2.7×10^{40}	1.3×10^{40}	2.2×10^{40}	3.9×10^{39}
Location	in spiral arm	in spiral arm	outlier	above one end of the LMC bar
Hα Morphology	one dominant core with filaments & small cores around	weak cores with long filaments & loops extending out	multiple cores with filaments around	one core with bright loops & filaments around

[a] We adopted the distances of 7.2 Mpc to M101 (Stetson et al., 1998) and 50 kpc to the LMC (Feast, 1999).

[b] The $L_{\mathrm{H}\alpha}$ of NGC 5461, NGC 5462, and NGC 5471 are measured using *HST* WFPC2 Hα images in this study, and the $L_{\mathrm{H}\alpha}$ of 30 Dor is adopted from Kennicutt & Hodge (1986). Note that these $L_{\mathrm{H}\alpha}$ are not corrected for extinction.

Table 4.2. Table of Observations

Object	Obs. Date (y/m/d)	Filter	Camera	Exp. Time
NGC 5461	1999/03/24	F547M	WF2	600s ×2, 100s ×2, 20s ×1
		F547M	PC1	20s ×2
		F675W	WF2	400s ×2, 50s ×2, 10s ×1
	1999/03/23	F656N	WF2	600s ×2, 160s ×1
NGC 5462	2000/02/01	F547M	WF2	600s ×2, 100s ×2, 20s ×1
		F547M	PC1	20s ×2
		F675W	WF2	400s ×2, 50s ×2, 10s ×1
		F656N	WF2	600s ×2, 160s ×1
NGC 5471	1997/11/01	F547M	WF3	600s ×2, 100s ×2, 20s ×1
		F547M	PC1	20s ×2
		F675W	WF3	400s ×2, 50s ×2, 10s ×1
		F656N	WF3	600s ×2, 180s ×1

Table 4.3. Photometry of Candidate Clusters in NGC 5461

ID	α_{J2000}	δ_{J2000}	M_{F547M}	$M_{\mathrm{F547M}} - M_{\mathrm{F675W}}$	$M_{\mathrm{F547M}} - M_{\mathrm{F675W'}}$
1	14 03 39.84	54 18 56.2	−9.35±0.01	0.45±0.05	0.23±0.02
2	14 03 39.91	54 18 56.2	−8.19±0.05	1.26±0.06	0.55±0.06
3	14 03 40.52	54 18 58.8	−8.97±0.01	0.17±0.03	0.16±0.02
4	14 03 40.54	54 18 59.2	−8.11±0.03	0.14±0.08	0.11±0.04
5	14 03 40.98	54 19 02.1	−8.25±0.02	0.11±0.06	0.09±0.03
6	14 03 41.15	54 19 04.5	−9.61±0.03	0.21±0.09	0.10±0.04
7	14 03 41.22	54 18 57.0	−8.01±0.02	0.17±0.02	0.13±0.02
8[a]	14 03 41.36	54 19 03.7	−10.40±0.10	0.59±0.13	0.36±0.10
			−10.19±0.06		
9[a]	14 03 41.40	54 19 03.8	−10.17±0.12	0.39±0.16	0.24±0.14
			−9.75±0.11		
10[a]	14 03 41.42	54 19 04.0	−10.81±0.06	0.27±0.09	0.22±0.07
			−10.57±0.06		
11	14 03 41.58	54 19 04.0	−9.27±0.05	1.37±0.05	0.58±0.05
12	14 03 41.58	54 19 07.8	−8.37±0.01	0.38±0.03	0.38±0.02

[a] The photometry is given in two rows, with the first row measured with the WFC images and the second row measured with the PC images.

Table 4.4. Photometry of Candidate Clusters in NGC 5462

ID	α_{J2000}	δ_{J2000}	M_{F547M}	$M_{\mathrm{F547M}} - M_{\mathrm{F675W}}$	$M_{\mathrm{F547M}} - M_{\mathrm{F675W'}}$
1	14 03 51.80	54 21 52.6	−8.83±0.04	0.32±0.05	0.16±0.04
2	14 03 51.83	54 21 46.2	−8.08±0.01	0.31±0.02	0.27±0.02
3	14 03 51.98	54 21 46.7	−8.64±0.01	0.36±0.02	0.33±0.02
4	14 03 52.07	54 21 49.1	−8.32±0.01	0.46±0.01	0.43±0.01
5	14 03 52.38	54 21 49.5	−8.33±0.02	0.20±0.03	0.15±0.03
6	14 03 52.41	54 21 49.1	−9.56±0.01	0.43±0.01	0.40±0.01
7	14 03 52.42	54 21 49.4	−8.16±0.05	0.47±0.05	0.44±0.05
8	14 03 52.43	54 21 50.0	−8.86±0.02	0.30±0.02	0.28±0.02
9	14 03 52.84	54 21 54.5	−8.05±0.02	0.14±0.03	0.12±0.03
10	14 03 52.86	54 21 59.3	−8.13±0.02	0.63±0.02	0.59±0.02
11	14 03 52.95	54 21 54.2	−8.55±0.01	0.65±0.02	0.52±0.02
12	14 03 52.96	54 22 06.4	−8.75±0.03	1.41±0.03	0.37±0.03
13	14 03 53.01	54 22 00.6	−8.44±0.02	0.51±0.02	0.45±0.02
14	14 03 53.03	54 21 56.1	−8.10±0.02	0.23±0.03	0.20±0.03
15	14 03 53.35	54 22 00.5	−8.87±0.01	0.20±0.01	0.17±0.01
16	14 03 53.41	54 21 59.1	−8.61±0.01	0.41±0.02	0.39±0.02
17	14 03 53.58	54 22 04.0	−8.03±0.02	0.44±0.03	0.42±0.02
18	14 03 53.78	54 22 11.1	−9.03±0.02	0.28±0.08	0.03±0.03
19	14 03 53.98	54 21 56.1	−8.24±0.01	0.50±0.02	0.48±0.02
20	14 03 54.00	54 22 07.9	−8.35±0.02	0.19±0.03	0.18±0.03
21	14 03 54.10	54 22 02.5	−8.30±0.01	0.54±0.02	0.41±0.02
22	14 03 54.18	54 22 06.6	−8.24±0.02	0.33±0.03	0.31±0.03
23	14 03 54.19	54 22 11.2	−9.17±0.01	0.55±0.01	0.51±0.01
24	14 03 54.32	54 22 09.1	−8.09±0.05	0.10±0.06	0.07±0.06
25	14 03 54.74	54 21 53.7	−8.20±0.01	0.27±0.01	0.24±0.01

Table 4.5. Photometry of Candidate Clusters in NGC 5471

ID	α_{J2000}	δ_{J2000}	M_{F547M}	$M_{\mathrm{F547M}} - M_{\mathrm{F675W}}$	$M_{\mathrm{F547M}} - M_{\mathrm{F675W'}}$
1[a]	14 04 28.64	54 23 51.9	−8.81±0.09	1.24±0.12	0.41±0.11
			−8.23±0.12		
2[a]	14 04 28.64	54 23 52.1	−9.31±0.08	1.46±0.10	0.76±0.10
			−9.05±0.09		
3	14 04 28.86	54 23 48.2	−9.08±0.03	−0.18±0.06	−0.13±0.04
4	14 04 28.88	54 23 47.8	−9.86±0.02	0.15±0.03	0.12±0.03
5	14 04 28.90	54 23 48.4	−10.27±0.01	−0.02±0.02	−0.07±0.02
6	14 04 29.10	54 23 41.7	−8.59±0.04	0.34±0.09	−0.09±0.05
7	14 04 29.15	54 23 45.9	−9.00±0.06	0.04±0.09	−0.11±0.07
8	14 04 29.17	54 23 45.4	−8.87±0.06	1.12±0.08	0.14±0.07
9	14 04 29.27	54 23 51.2	−9.38±0.01	0.26±0.03	0.19±0.01
10	14 04 29.29	54 23 52.4	−8.71±0.08	0.99±0.11	0.14±0.13
11	14 04 29.29	54 23 52.9	−8.21±0.05	0.86±0.09	0.22±0.08
12	14 04 29.33	54 23 47.2	−9.06±0.02	0.37±0.04	0.19±0.03
13	14 04 29.37	54 23 46.5	−8.47±0.04	0.34±0.04	−0.04±0.04
14	14 04 29.38	54 23 46.2	−8.08±0.06	0.72±0.08	0.35±0.09
15	14 04 29.39	54 23 51.8	−8.02±0.02	0.54±0.14	0.02±0.09
16	14 04 29.47	54 23 46.4	−10.06±0.06	0.16±0.13	−0.13±0.06
17	14 04 29.53	54 23 46.1	−8.68±0.14	1.47±0.15	0.25±0.15
18	14 04 29.54	54 23 45.8	−8.40±0.11	1.38±0.13	0.52±0.12
19	14 04 29.56	54 23 47.5	−8.97±0.02	0.44±0.07	0.21±0.03

[a] The photometry is given in two rows, with the first row measured with the WFC images and the second row measured with the PC images.

Table 4.6. Physical Properties of Massive Clusters in M101 GHRs

Cluster ID	Age (Myr)	Starburst99 Mass ($\times 10^4 M_\odot$)	BC03 Mass ($\times 10^4 M_\odot$)	$R_{\rm eff}$ (pc)	Remarks
NGC 5461-1	< 5	2 ± 0.5	2 ± 0.5	...	
NGC 5461-6	< 5	1 ± 0.5	$\lesssim 1$	0.8 ± 0.2	
NGC 5461-8	< 5	1.5 ± 0.5	1.5 ± 0.5	0.7 ± 0.2	
NGC 5461-9	< 5	1.5 ± 0.5	1 ± 0.5	...	
NGC 5461-10	< 5	3 ± 1	2 ± 1	2.1 ± 0.1	asymmetric morphology
NGC 5461-11	< 5	~ 0.5	$\lesssim 0.5$	...	
NGC 5462-6	> 10	~ 2	1.5–2	2.3 ± 0.3	asymmetric morphology
NGC 5462-18	< 5	$\lesssim 1$	0.5–1	...	
NGC 5462-23	> 10	~ 2	1.5–2	...	
NGC 5471-2	< 5	~ 0.2	~ 0.2	...	
NGC 5471-3	> 10	~ 0.5	~ 0.5	...	
NGC 5471-4	> 10	$\gtrsim 1$	$\gtrsim 1$	2.9 ± 0.3	asymmetric morphology
NGC 5471-5	> 10	~ 2	~ 2	1.4 ± 0.1	asymmetric morphology
NGC 5471-7	< 5	~ 0.5	~ 0.5	...	
NGC 5471-9	> 10	~ 1	~ 1	0.2 ± 0.1	probably a star
NGC 5471-12	< 5	~ 0.5	~ 0.5	...	
NGC 5471-16	< 5	1.5 ± 0.5	1.5 ± 0.5	1.1 ± 0.1	

Table 4.7. Fractional Contribution of Clusters to Total Stellar Light & Ionizing Luminosity

	Region 1	Region 2	Region 3	Region 4
Clusters	NGC 5461-1	NGC 5461-8,9,10	NGC 5462-18	NGC 5471-16
Continuum Aperture Diameter	$1\farcs3$	$2\farcs2$	$1\farcs4$	$1\farcs5$
$\frac{L_{\rm cluster}}{L_{\rm total}}$ in F547M	0.47 ± 0.05	0.43 ± 0.08	0.41 ± 0.04	0.30 ± 0.03
$\frac{L_{\rm cluster}}{L_{\rm total}}$ in F675W′	0.39 ± 0.04	0.38 ± 0.08	0.35 ± 0.04	0.24 ± 0.03
Hα Aperture Diameter	$2\farcs1 \times 2\farcs0$	$3\farcs5 \times 2\farcs8$	$2\farcs4 \times 2\farcs3$	$2\farcs5 \times 2\farcs3$
$Q_{\rm HII}$ ($\times 10^{50}$ s^{-1})	14	97	12	37
$Q_{\rm cluster}$[a]($\times 10^{50}$ s^{-1})	8	24	4	8
$\frac{Q_{\rm cluster}}{Q_{\rm HII}}$[a]	0.57	0.25	0.33	0.22

[a] The ionizing luminosities of these clusters are estimated assuming a cluster age of 3 Myr. Since these clusters are only know to have ages < 5 Myr, the ionizing luminosity of the clusters and thus the ratio $\frac{Q_{\rm cluster}}{Q_{\rm HII}}$ could range from 1/4 to 1.5 times the value in the table.

Chapter 5

Conclusions

5.1 Summary

Star formation can be characterized at two levels: on the microscopic level by the IMF, and on the macroscopic level by space, time and intensity. To understand how star formation proceeds across a region, one needs to examine all four parameters. In this thesis, we have used the resolved massive stars and YSOs of N 44 to carry out a detailed study of star formation at both levels with extended coverage in space and time. We have also used the resolved cluster content of luminous GHRs in M101 to examine macroscopic star formation in a starburst environment. The main results of the thesis are described below.

5.1.1 Massive Star Formation in H II Complex N 44

Our study of massive stars in N 44 found that the PDMFs of the four star formation regions do not show obvious variations. The PDMF of the SB-rim region is steeper than the Salpeter IMF, but this steeper slope may be caused by a prolonged star formation period. The PDMFs of the field regions are steeper than the PDMFs of the star formation regions. The PDMFs of field stars at different locations from the OB associations exhibit similar slopes but with different cutoffs at the high-mass end, suggesting that star formation history varies from location to location. As star formation is a complex function of space and time, assumptions made for converting PDMF to IMF have to be critically examined.

We have used *Spitzer* observations to search for YSOs in N 44. We use multi-wavelength images and SEDs to critically confirm 59 YSO candidates. About 60% of the confirmed YSOs are either resolved into multiple systems or show extended images in ISPI images, stressing the importance of using high resolution data. The masses of single-source YSOs are estimated using multi-parameter fits to the SEDs and range from 8 to 25 $M_{\odot}$, though the lower mass limit of the entire YSO sample would be $\sim 4M_{\odot}$. We have examined the immediate interstellar environment of YSOs in H II regions with images available in the *HST* archive. A small H II region is detected around the YSO projected near N 44C; the ionization requirement from the Hα emission is consistent with that expected for a B2-3V star estimated from our *UBV* photometry. An

YSO emerging at the tip of a dust pillar is found in N 44F; the spatial configuration is similar to those in the Eagle Nebula, but this YSO is more massive. The great majority of YSOs are found in molecular clouds and concentrated toward the three molecular peaks. Among the three peaks, the central molecular peak has the most concentrated distribution of YSOs as well as molecular material. As the molecular peak is centered on the superbubble rim, together with that the distribution of YSOs is along the rim instead of a scattered pattern shown by YSOs in other molecular peaks, the triggering from the expansion of the superbubble must have played an important role in the current star formation in this cloud. The northern molecular peak has loosely distributed YSOs and the lowest concentration of molecular material. These YSOs are not associated with large ionized gas structures, indicating that they are the first generation of massive stars formed in that cloud. Using the relationship between YSOs and their interstellar environment, we showed that star formation may have proceeded from the central to the south molecular peak.

5.1.2 Clusters in GHRs in M101

Our study of clusters in the three luminous GHRs in M101 found that the types of cluster contents are different in GHRs with distinct morphologies. NGC 5461 is dominated by a very luminous core, and has been suggested to host a SSC. Our observations show that it contains three R136-class clusters superposed on a bright stellar background in a small region. This tight group of clusters may dynamically evolve into an SSC in the future, and may appear unresolved and be identified as an SSC at large distances, but at present NGC 5461 contains no SSCs. NGC 5462 consists of loosely distributed H II regions and clusters without a prominent core. It has the largest number of cluster candidates among the three GHRs studied, but most of them are faint and older than 10 Myr. NGC 5471 has multiple bright H II regions, and contains a large number of faint clusters younger than 5 Myr. Two of the clusters in NGC 5471 are older than R136, but just as luminous; they may be the most massive clusters in the three GHRs studied.

The fraction of stars formed in massive clusters has been estimated from the clusters' contribution to the total stellar continuum emission and from a comparison between the ionizing power of the clusters and the ionizing requirement of the associated H II regions. Both estimates show that $\lesssim$ 50% of massive stars are formed in massive clusters; consequently, the Hα luminosity of an H II region does not provide a sufficient condition for the existence of SSCs. The cluster LFs of the three GHRs show different slopes. NGC 5462 has the steepest cluster LF and the most loosely distributed interstellar gas, qualitatively consistent with the hypothesis that massive clusters are formed in high-pressure interstellar environments. The combined cluster LF of the three GHRs has a slope similar to the universal cluster LFs seen in starburst galaxies and non-starburst spiral galaxies.

5.2 Future Work

5.2.1 New Optical and IR Ground-based Observations of N 44 – Better Data Quality

Due to the limitations of the angular resolution, area coverage and sensitivity of the 0.9m *UBV* data, it is difficult to push down the uncertainties in determining slopes of the PDMFs, or to examine the field population at a larger distance from the OB associations. Furthermore, with only the *UBV* bandpass, lower-mass stars in high extinction regions, which are common in star formation regions, are difficult to detect.

We have obtained *UBVI* and JK_s observations of N 44 with the MOSAIC CCD Imager and ISPI on the CTIO 4m Blanco telescope, respectively. These new observations have higher angular resolutions and deeper exposures. They also include the IJK_s bands at longer wavelengths, which suffer less from extinction effects. The new data will help to expand the mass range for determining the slope of the PDMF to lower masses, and also help to differentiate the factor that caused the deficiency of observed lower mass stars in the four star formation regions in N 44.

5.2.2 *HST* NICMOS and WFPC2 Observations of N 44

Our *Spitzer* observations reveal a large number of massive YSOs in N 44. One of the YSOs, 052207.3−675819.9, is resolved to have a small H II region with size $\sim 1\farcs1$ in the *HST* Hα image. However, this YSO has an SED that can be fitted satisfactorily with a Class II model, an earlier stage than that evidenced by the presence of a H II region. This YSO would have been mistakenly categorized to an earlier stage if only the ground-based, lower resolution images were used. This demonstrates the importance of using high resolution images to examine the evolutionary states of YSOs. Furthermore, using the ground-based ISPI images, we found that $\sim$ 30% of the YSOs are resolved into multiple sources, and another $\sim$ 30% show extended images, uncertain of their multiplicity. To examine whether sources with extended images are multiples, high resolution IR images are also needed.

We have therefore proposed to use *HST* WFPC2 and NICMOS observations of N 44 to determine the masses, evolutionary states, and pre-natal environments of YSOs. We have requested WFPC2 Hα and continuum images of YSO candidates in N 44 to determine whether these YSOs: are still obscured, have small compact HII regions, are in bright-rimmed dust globules, and are single or multiple. The Hα flux of an HII region can be further used to derive the rms electron density and required ionizing power. We will use the physical conditions of the local ISM to determine whether the star formation was triggered. We have also requested NICMOS images of these YSOs to better resolve the YSOs from their companions and nearby nebulae. We can accurately determine the near-IR fluxes for the YSOs, and an accurately determined SED of a YSO from near-IR to mid-IR is essential for detailed modeling of its stellar mass and circumstellar disk and envelope properties (Whitney et al., 2004b; Chu et al., 2005; Robitaille et al., 2006). The better determined YSO properties will result in a more accurate IMF of the emerging stellar population in N 44. With the improved knowledge of the interstellar environment, we can increase our understanding of the relationship between the YSOs and their initial conditions.

References

Allen, R. J., Atherton, P. D., & Tilanus, R. P. J. 1985, in ASSL Vol. 120: Birth and Evolution of Massive Stars and Stellar Groups, ed. W. Boland & H. van Woerden, 243

Allen, R. J., Atherton, P. D., & Tilanus, R. P. J. 1986, Nature, 319, 296

Baumgardt, H., & Makino, J. 2003, MNRAS, 340, 227

Bessell, M., & Murdin, P. 2000, Encyclopedia of Astronomy and Astrophysics

Biretta et al., J. A. 1996, WFPC2 Instrument Handbook, Version 4.0 (Baltimore: STScI)

Blanco, V. M., & McCarthy, M. F. 1990, AJ, 100, 674

Bonnell, I. A., Bate, M. R., & Vine, S. G. 2003, MNRAS, 343, 413

Boutloukos, S. G., & Lamers, H. J. G. L. M. 2003, MNRAS, 338, 717

Bruzual, G., & Charlot, S. 2003, MNRAS, 344, 1000

Bruzual A., G., & Charlot, S. 1993, ApJ, 405, 538

Calvet, N., et al. 2005, ApJ, 630, L185

Castaneda, H. O., Vilchez, J. M., & Copetti, M. V. F. 1990, ApJ, 365, 164

Cesaroni, R., Galli, D., Lodato, G., Walmsley, C. M., & Zhang, Q. 2007, in Protostars and Planets V, ed. B. Reipurth, D. Jewitt, & K. Keil, 197

Chin, Y.-N., Henkel, C., Whiteoak, J. B., Millar, T. J., Hunt, M. R., & Lemme, C. 1997, A&A, 317, 548

Chu, Y.-H., et al. 2005, ApJ, 634, L189

Chu, Y.-H., Low, M.-M. M., Garcia-Segura, G., Wakker, B., & Kennicutt, Jr., R. C. 1993, ApJ, 414, 213

Cohen, M., Wheaton, W. A., & Megeath, S. T. 2003, AJ, 126, 1090

Davis, L. E. 1994, A Reference Guide to the IRAF/DAOPHOT Package

De Buizer, J. M., Osorio, M., & Calvet, N. 2005, ApJ, 635, 452

de Grijs, R., Anders, P., Bastian, N., Lynds, R., Lamers, H. J. G. L. M., & O'Neil, E. J. 2003, MNRAS, 343, 1285

DeGioia-Eastwood, K., Throop, H., Walker, G., & Cudworth, K. M. 2001, ApJ, 549, 578

Deharveng, L., Lefloch, B., Massi, F., Brand, J., Kurtz, S., Zavagno, A., & Caplan, J. 2006, A&A, 458, 191

Deharveng, L., Zavagno, A., & Caplan, J. 2005, A&A, 433, 565

Egan, M. P., Van Dyk, S. D., & Price, S. D. 2001, AJ, 122, 1844

Elmegreen, B. G. 1998, in ASP Conf. Ser. 148: Origins, ed. C. E. Woodward, J. M. Shull, & H. A. Thronson, Jr., 150

Elmegreen, B. G., & Efremov, Y. N. 1997, ApJ, 480, 235

Elmegreen, B. G., & Scalo, J. 2006, ApJ, 636, 149

Elson, R. A. W., & Fall, S. M. 1985, ApJ, 299, 211

Elson, R. A. W., Fall, S. M., & Freeman, K. C. 1987, ApJ, 323, 54

Elson, R. A. W., Freeman, K. C., & Lauer, T. R. 1989, ApJ, 347, L69

Evans, I. N. 1986, ApJ, 309, 544

Fazio, G. G., et al. 2004, ApJS, 154, 10

Feast, M. 1999, in IAU Symp. 190: New Views of the Magellanic Clouds, ed. Y.-H. Chu, N. Suntzeff, J. Hesser, & D. Bohlender, 542

Finkenzeller, U., & Mundt, R. 1984, A&AS, 55, 109

Fioc, M., & Rocca-Volmerange, B. 1997, A&A, 326, 950

Franceschini, A., et al. 2005, AJ, 129, 2074

Franco, J., Kurtz, S. E., García-Segura, G., & Hofner, P. 2000, Ap&SS, 272, 169

Freedman, W. L., Wilson, C. D., & Madore, B. F. 1991, ApJ, 372, 455

Fukui, Y., Mizuno, N., Yamaguchi, R., Mizuno, A., & Onishi, T. 2001, PASJ, 53, L41

Giannakopoulou-Creighton, J., Fich, M., & Wilson, C. D. 1999, ApJ, 522, 238

Gordon, K. D., et al. 2005, PASP, 117, 503

Grebel, E. K., & Chu, Y.-H. 2000, AJ, 119, 787

Groenewegen, M. A. T. 2006, A&A, 448, 181

Gruendl, R. A., & The Illinois Team. 2007, in preparation

Harris, W. E. 1996, AJ, 112, 1487

Harvey, P. M., et al. 2006, ApJ, 644, 307

Hatziminaoglou, E., et al. 2005, AJ, 129, 1198

Heggie, D. C. 1985, in IAU Symp. 113: Dynamics of Star Clusters, ed. J. Goodman & P. Hut, 139–157

Henize, K. G. 1956, ApJS, 2, 315

Hester, J. J., et al. 1996, AJ, 111, 2349

Hillenbrand, L. A., Massey, P., Strom, S. E., & Merrill, K. M. 1993, AJ, 106, 1906

Hillenbrand, L. A., Strom, S. E., Vrba, F. J., & Keene, J. 1992, ApJ, 397, 613

Hodge, P. 1988, PASP, 100, 1051

Hodge, P. W., Gurwell, M., Goldader, J. D., & Kennicutt, Jr., R. C. 1990, ApJS, 73, 661

Holtzman, J. A., et al. 1995, PASP, 107, 156

Humphreys, R. M. 1978, ApJS, 38, 309

Humphreys, R. M., & Davidson, K. 1979, ApJ, 232, 409

—. 1994, PASP, 106, 1025

Humphreys, R. M., Massey, P., & Freedman, W. L. 1990, AJ, 99, 84

Hunter, D. A., Baum, W. A., O'Neil, Jr., E. J., & Lynds, R. 1996, ApJ, 456, 174

Hunter, D. A., Shaya, E. J., Holtzman, J. A., Light, R. M., O'Neil, Jr., E. J., & Lynds, R. 1995, ApJ, 448, 179

Israel, F. P., Goss, W. M., & Allen, R. J. 1975, A&A, 40, 421

Johnson, H. L. 1966, ARA&A, 4, 193

Johnson, H. L., & Morgan, W. W. 1953, ApJ, 117, 313

Johnson, K. E., & Kobulnicky, H. A. 2003, ApJ, 597, 923

Kennicutt, R. C., & Hodge, P. W. 1986, ApJ, 306, 130

Kennicutt, Jr., R. C. 1984, ApJ, 287, 116

Kennicutt, Jr., R. C., & Chu, Y.-H. 1988, AJ, 95, 720

Kennicutt, Jr., R. C., & Garnett, D. R. 1996, ApJ, 456, 504

King, I. 1962, AJ, 67, 471

Kobulnicky, H. A., & Johnson, K. E. 1999, ApJ, 527, 154

Krist, J. 1995, in ASP Conf. Ser. 77: Astronomical Data Analysis Software and Systems IV, ed. R. A. Shaw, H. E. Payne, & J. J. E. Hayes, 349

Kroupa, P., Tout, C. A., & Gilmore, G. 1993, MNRAS, 262, 545

Lada, C. J. 1987, in IAU Symp. 115: Star Forming Regions, ed. M. Peimbert & J. Jugaku, 1–17

Landolt, A. U. 1992, AJ, 104, 340

Larsen, S. S. 1999, A&AS, 139, 393

—. 2002, AJ, 124, 1393

Leitherer, C., et al. 1999, ApJS, 123, 3

Lejeune, T., & Schaerer, D. 2001, A&A, 366, 538

Li, A., & Draine, B. T. 2001, ApJ, 554, 778

—. 2002, ApJ, 576, 762

Loup, C., Zijlstra, A. A., Waters, L. B. F. M., & Groenewegen, M. A. T. 1997, A&AS, 125, 419

Lucke, P. B., & Hodge, P. W. 1970, AJ, 75, 171

Luridiana, V., Esteban, C., Peimbert, M., & Peimbert, A. 2002, Revista Mexicana de Astronomia y Astrofisica, 38, 97

Luridiana, V., & Peimbert, M. 2001, ApJ, 553, 633

Mackey, A. D., & Gilmore, G. F. 2003, MNRAS, 338, 85

Madore, B. F. 1982, ApJ, 253, 575

Maíz-Apellániz, J. 2001, ApJ, 563, 151

Massey, P. 1985, PASP, 97, 5

Massey, P., & Davis, L. E. 1992, A User's Guide to Stellar CCD Photometry with IRAF

Massey, P., & Johnson, J. 1993, AJ, 105, 980

Massey, P., Lang, C. C., Degioia-Eastwood, K., & Garmany, C. D. 1995, ApJ, 438, 188

Massey, P., & Thompson, A. B. 1991, AJ, 101, 1408

Mathis, J. S. 1990, ARA&A, 28, 37

Mayya, Y. D. 1997, ApJ, 482, L149

Meixner, M., et al. 2006, AJ, 132, 2268

Mendoza, E. E. 1967, Boletin de los Observatorios Tonantzintla y Tacubaya, 4, 106

Meurer, G. R., Heckman, T. M., Leitherer, C., Kinney, A., Robert, C., & Garnett, D. R. 1995, AJ, 110, 2665

Mizuno, N., Yamaguchi, R., Mizuno, A., Rubio, M., Abe, R., Saito, H., Onishi, T., Yonekura, Y., Yamaguchi, N., Ogawa, H., & Fukui, Y. 2001, PASJ, 53, 971

Moffat, A. F. J., & Fitzgerald, M. P. 1977, A&A, 54, 263

Moffat, A. F. J., Seggewiss, W., & Shara, M. M. 1985, ApJ, 295, 109

O'Connell, R. W., Gallagher, III, J. S., & Hunter, D. A. 1994, ApJ, 433, 65

Oey, M. S., & Massey, P. 1995, ApJ, 452, 210

Origlia, L., Goldader, J. D., Leitherer, C., Schaerer, D., & Oliva, E. 1999, ApJ, 514, 96

Parker, J. W., Garmany, C. D., Massey, P., & Walborn, N. R. 1992, AJ, 103, 1205

Parker, J. W., Zaritsky, D., Stecher, T. P., Harris, J., & Massey, P. 2001, AJ, 121, 891

Peimbert, M., & Torres-Peimbert, S. 1974, ApJ, 193, 327

Pilyugin, L. S. 2001, A&A, 373, 56

Ratnatunga, K. U., & Bahcall, J. N. 1985, ApJS, 59, 63

Reid, N., Glass, I. S., & Catchpole, R. M. 1988, MNRAS, 232, 53

Ressler, M. E., & Barsony, M. 2003, ApJ, 584, 832

Rice, W. K. M., Wood, K., Armitage, P. J., Whitney, B. A., & Bjorkman, J. E. 2003, MNRAS, 342, 79

Rieke, G. H., et al. 2004, ApJS, 154, 25

Roberts, M. S., & Rots, A. H. 1973, A&A, 26, 483

Roberts, W. W. 1969, ApJ, 158, 123

Robitaille, T. P., Whitney, B. A., Indebetouw, R., & Wood, K. 2007, ApJS, 169, 328

Robitaille, T. P., Whitney, B. A., Indebetouw, R., Wood, K., & Denzmore, P. 2006, ApJS, 167, 256

Rodgers, A. W., Campbell, C. T., & Whiteoak, J. B. 1960, MNRAS, 121, 103

Rowan-Robinson, M., et al. 2005, AJ, 129, 1183

Rowan-Robinson, M., Lock, T. D., Walker, D. W., & Harris, S. 1986, MNRAS, 222, 273

Schaerer, D., & de Koter, A. 1997, A&A, 322, 598

Schlegel, D. J., Finkbeiner, D. P., & Davis, M. 1998, ApJ, 500, 525

Schmidt-Kaler, T. 1982, in Landolt-Börnstein New Series, Group 6, Volume 2b, Stars and Star Clusters, ed. K. Schaifers & H. H. Voigt (Berlin: Springer)

Scowen, P. A., Dufour, R. J., & Hester, J. J. 1992, AJ, 104, 92

Skillman, E. D. 1985, ApJ, 290, 449

Skrutskie, M. F., et al. 2006, AJ, 131,

Smith, D. A., Allen, R. J., Bohlin, R. C., Nicholson, N., & Stecher, T. P. 2000, ApJ, 538, 608

Smith, R. C., & The MCELS Team. 1999, in IAU Symp. 190: New Views of the Magellanic Clouds, ed. Y.-H. Chu, N. Suntzeff, J. Hesser, & D. Bohlender, 28

Stahler, S. W., Palla, F., & Ho, P. T. P. 2000, Protostars and Planets IV, 327

Stetson, P. B. 1987, PASP, 99, 191

Stetson, P. B., et al. 1998, ApJ, 508, 491

Thompson, R. I., Smith, B. A., & Hester, J. J. 2002, ApJ, 570, 749

Turner, J. L., Beck, S. C., & Ho, P. T. P. 2000, ApJ, 532, L109

van Boekel, R., Waters, L. B. F. M., Dominik, C., Dullemond, C. P., Tielens, A. G. G. M., & de Koter, A. 2004, A&A, 418, 177

Walborn, N. R., & Blades, J. C. 1997, ApJS, 112, 457

Waller, W. H., et al. 1997, ApJ, 481, 169

Whitmore, B. C. 2003, in A Decade of Hubble Space Telescope Science, ed. M. Livio, K. Noll, & M. Stiavelli, 153–178

Whitmore, B. C., Zhang, Q., Leitherer, C., Fall, S. M., Schweizer, F., & Miller, B. W. 1999, AJ, 118, 1551

Whitney, B. A., et al. 2004a, ApJS, 154, 315

Whitney, B. A., Indebetouw, R., Bjorkman, J. E., & Wood, K. 2004b, ApJ, 617, 1177

Will, J.-M., Bomans, D. J., & Dieball, A. 1997, A&AS, 123, 455

Wood, P. R., Whiteoak, J. B., Hughes, S. M. G., Bessell, M. S., Gardner, F. F., & Hyland, A. R. 1992, ApJ, 397, 552

Zaritsky, D., Harris, J., Thompson, I. B., & Grebel, E. K. 2004, AJ, 128, 1606

Zavagno, A., Deharveng, L., Comerón, F., Brand, J., Massi, F., Caplan, J., & Russeil, D. 2006, A&A, 446, 171

Curriculum Vitae

Chang-Hui Rosie Chen

University of Illinois at Urbana-Champaign
Department of Astronomy
1002 W. Green St.
Urbana, IL 61801 USA

Voice: (217) 333-7957
Fax: (217) 244-7638
E-mail: c-chen@astro.uiuc.edu
Web: www.astro.uiuc.edu/~c-chen

EDUCATION

University of Illinois at Urbana-Champaign, Urbana, Illinois, USA

Ph.D., Astronomy, May 2007

Dissertation Topic: "Star Formation in OB Associations and Clusters"

Advisor: You-Hua Chu

National Central University, Chung-Li, Taiwan

M.S., Astronomy, June 1996

National Central University, Chung-Li, Taiwan

B.A., Earth Science, May 1994

PROFESSIONAL EMPLOYMENT

1998–2007: Graduate Assistant (under teaching and research duty),
Astronomy Department, University of Illinois at Urbana-Champaign.

1996–1998: Research Assistant,
Institute of Astronomy, National Central University.

1994–1996: Research Fellowship,
Institute of Astronomy, National Central University.

ASSOCIATION MEMBERSHIPS

American Astronomical Society, Junior Member

PUBLICATIONS

Refereed Journal Articles

1. Williams, R.M., Chu, Y.-H., **Chen, C.-H.R.**, Gruendl, R.A., Points, S.D., and Smith, R.C. "Supernova Remnants in the Magellanic Clouds. VIII. SNRs in the N19 Complex," 2007, ApJ, submitted.
2. Ramsey, C.J., Williams, R.M., Gruendl, R.A., **Chen, C.-H.R.**, Chu, Y.-H., and Wang, Q.D. "An Optical Study of Stellar and Interstellar Environments of Seven Luminous and Ultraluminous X-ray Sources," 2006, ApJ, 641, 241-251.
3. Chu, Y.-H., Gruendl, R.A., **Chen, C.-H.R.**, Whitney, B.A., Gordon, K.D., Looney, L.W., Clayton, G.C., Dickel, J.R., Dunne, B.C., Points, S.D., Smith, R.C., and Williams, R.M. "Protostars, Bok Globules, and a Herbig-Haro Object in the LMC Superbubble N51D," 2005, ApJ, 634, L189-192.
4. Kuntz, K.D., Gruendl, R.A., Chu, Y.-H., **Chen, C.-H.R.**, Still, M., Mukai, K., and Mushotzky, R.F. "The Optical Counterpart of M101 ULX-1," 2005, ApJ, 620, L31-34.
5. **Chen, C.-H.R.**, Chu, Y.-H., and Johnson, K.E. "Clusters in the Luminous Giant H II Regions in M101," 2005, ApJ, 619, 779-799.
6. Chu, Y.-H., Gruendl, R.A., **Chen, C.-H.R.**, Lazendic, J.S., and Dickel, J.R. "An Optical and X-Ray Examination of Two Radio Supernova Remnant Candidates in 30 Doradus," 2004, ApJ, 615, 727-731.
7. Cooper, R.L., Guerrero, M.A., Chu, Y.-H., **Chen, C.-H.R.**, and Dunne, B.C. "Energy Crisis in the Superbubble DEM L192," 2004, ApJ, 605, 751-758.
8. Metz, J.M., Cooper, R.L., Guerrero, M.A., Chu, Y.-H., **Chen, C.-H.R.**, and Gruendl, R.A. "Hot Interstellar Gas and Stellar Energy Feedback in the Antennae Galaxies," 2004, ApJ, 605, 725-741.
9. Dunne, B.C., Chu, Y.-H., **Chen, C.-H.R.**, Lowry, J.D., Townsley, L., Gruendl, R.A., Guerrero, M.A., and Rosado, M. "Diffuse X-Ray Emission from the Quiescent Superbubble M17, the Omega Nebula," 2003, ApJ, 590, 306-313.
10. Chu, Y.-H., **Chen, C.-H.R.**, Danforth, C., Dunne, B.C., Gruendl, R.A., Naze, Y., Oey, M.S., and Points, S.D. "The Wind of the B[e] Supergiant Henize S22 Viewed Through a Reflection Nebula in DEM L106," 2003, AJ, 125, 2098-2107.
11. **Chen, C.-H. R.**, Chu, Y.-H., Gruendl, R.A., Lai, S.-P., and Wang, Q.D. "A Critical Examination of Hypernova Remnant Candidates in M101. II. NGC 5471B," 2002, AJ, 123, 2462-2472.
12. Naze, Y., Chu, Y.-H., Points, S.D., Danforth, C.W., Rosado, M., and **Chen, C.-H.R.** "Interstellar Bubbles in Two Young H II Regions," 2001, AJ, 122, 921-937.

13. Lai, S.-P., Chu, Y.-H., **Chen, C.-H.R.**, Ciardullo, R., and Grebel, E.K. " A Critical Examination of Hypernova Remnant Candidates in M101. I. MF83," 2001, ApJ, 545, 754-764.
14. Williams, R.M., Petre, R., Chu, Y.-H., and **Chen, C.-H.R.** "Resolving SNR 0540–6944 From LMC X-1 With *Chandra*," 2000, ApJ, 536, L27-30.
15. **Chen, C.-H.R.**, Chu, Y.-H., Gruendl, R.A., and Points, S.D. "Hubble Space Telescope Wide Field Planetary Camera 2 Imaging of Shocks in Superbubbles," 2000, AJ, 119, 1317-1324.
16. Tsay, W.-S., Chen, A.B.C., **Chen, R.**, Lu, P.K., Smith, A, and Mendez, R. "Snapshots of CCD Fields in a Study of the Vertical Distribution of Stars," 1997, Baltic Astronomy, 6, 141-144.
17. Lu, P.K., Tsay, W.-S., Chen, A.B.C., **Chen, R.**, Sun, W., Byun, Y.-I., et al. "Multiband Photometry of Selected Areas in a Study of Galactic Structure," 1997, Baltic Astronomy, 6, 33-40.

Conference Proceedings

1. **Chen, C.-H.R.**, Chu, Y.-H., Gruendl, R.A. and Heitsch, F., 2006, "Triggered Massive Star Formation in the LMC H II Complex N 44," in the IAU Symposium of "Triggered Star Formation in a Turbulent ISM," in press.
2. **Chen, C.-H.R.**, Wang, S., Guerrero, M.A., Chu, Y.-H., and Gruendl, R.A., 2004, "*Chandra* Archive of Nearby Galaxies. I. Normal Galaxies," in the proceedings of "How Does the Galaxy Work? A Galactic Tertulia with Don Cox and Ron Reynolds," 186.
3. Wang, S., **Chen, C.-H.R.**, Guerrero, M.A., Chu, Y.-H., and Gruendl, R.A., 2004, "Chandra Archive of Nearby Galaxies. II. Galaxies with Nuclear Activity," in the proceedings of "How Does the Galaxy Work? A Galactic Tertulia with Don Cox and Ron Reynolds," 189-190.
4. Chu, Y.-H., **Chen, C.-H.R.**, and Lai, S.-P., 2000, "Super-luminous Supernova Remnants," in "The Largest Explosion Since the Big Bang: Supernovae and Gamma-Ray Bursts", 1999 STScI May Symposium, 131-143.
5. **Chen, C.-H.R.**, Tsay, W.-S. and Lu, P. K., 1996, "Study of NGC 288 on Strömgren Photometry," JKASS, 29, 135-136.
6. **Chen, C.-H.**, and Jamk, P.C., 1996, "Large Format CCD Photometry in the Globular Cluster NGC 288," in "Proceedings of the Third East-Asian Meeting on Astronomy," 214-217.